

Influence of Extended Defects on the Electrical Properties of TiO_2 (Rutile)



Kiran Kumar Adepalli

Max-Planck-Institut für Festkörperforschung

Stuttgart

Dissertation an der Universität Stuttgart

2013

Influence of Extended Defects on the Electrical Properties of TiO₂ (Rutile)

Von der Fakultät Chemie der Universität Stuttgart
zur Erlangung der Würde eines
Doktors der Naturwissenschaften (Dr. rer. nat.)
genehmigte Abhandlung

Vorgelegt von

Kiran Kumar Adepalli

aus Godicherla, Indien

Hauptberichter:	Prof. Dr. Joachim Maier
Mitberichter:	Prof. Dr. Joachim Bill
Prüfungsvorsitzender:	Prof. Dr. Frank Gißelmann

Tag der Einreichung:	03.05.2013
Tag der mündlichen Prüfung:	24.06.2013

Max-Planck-Institut für Festkörperforschung
Universität Stuttgart

2013

To my FATHER in heaven...

Erklärung

Die vorliegende Doktorarbeit wurde vom Autor selbst in der Abteilung von Prof. Maier am Max-Planck-Institut für Festkörperforschung, im Zeitraum von 09/2009 bis 05/2013 angefertigt. Der Inhalt ist die eigene Arbeit des Autors, Ausnahmen sind gekennzeichnet, und wurde noch nicht zur Erlangung einer Qualifizierung oder eines Titels an einer akademischen Institution eingereicht.

Stuttgart, den 03 Mai 2013

Kiran Kumar Adepalli

Declaration

The work described in this thesis was carried out by the author in the Department of Prof. Maier at the Max Planck Institute for Solid State Research from 09/2009 to 05/2013. The contents are the original work of the author except where indicated otherwise and have not been previously submitted for any other degree or qualification at any academic institution.

Stuttgart, 03 May 2013

Kiran Kumar Adepalli

Contents

List of Figures	xi
List of Tables	xvii
List of abbreviations and symbols	xix
1 Introduction and motivation	1
1.1 Choice of material and outline of thesis	4
2 Theoretical background	7
2.1 Introduction to TiO ₂	7
2.2 Classification of defects	8
2.3 Defect chemistry of TiO ₂	13
2.3.1 Undoped TiO ₂	15
2.3.2 Acceptor doped TiO ₂	18
2.3.3 Donor doped TiO ₂	19
2.4 Impedance spectroscopy	22
2.5 Space charge effects	27
3 Materials and Methods	33
3.1 TiO ₂ single crystals	33
3.2 Polycrystalline TiO ₂ powder synthesis	33
3.2.1 Doping and decoration	35
3.3 Sintering procedures	35
3.3.1 Conventional sintering	36
3.3.2 Spark plasma sintering	37

CONTENTS

3.4	Electrical characterization	37
3.4.1	Electrode preparation and cell assembly	37
3.4.2	Impedance spectroscopy	39
3.4.3	DC characterization	40
3.4.4	Wagner-Hebb polarization	40
3.5	Creating 1-D defects	41
3.5.1	Deformation Mechanism Maps	41
3.5.2	Dislocation Generation	43
3.6	Creating 2-D defects	44
3.6.1	Bicrystal Preparation	44
3.7	1- and 2-D defect characterization	47
3.7.1	Transmission electron microscopy	47
3.7.2	TEM sample preparation	47
3.7.3	Oxygen Isotope Exchange Experiments	48
3.7.4	Secondary Ion Mass Spectroscopy	49
I	Results and discussion on 1-D defects	51
4	Single crystal TiO₂	53
4.1	Defect characterization	54
4.1.1	TEM on crystals compressed along [001]	55
4.1.2	TEM on crystals compressed along [110]	57
4.2	Electrical characterization	60
4.2.1	[001] oriented crystals	60
4.2.2	[110] orientated crystals	64
4.3	Partial conductivities in [001] crystals	66
4.4	Oxygen tracer experiments	68
4.5	Discussion based on the space charge model	71
4.6	Conclusions on single crystals	74
5	Polycrystalline TiO₂	75
5.1	Defect characterization	76
5.2	Electrical characterization	77

5.2.1	Conventionally sintered samples	77
5.2.2	Spark plasma sintered samples	79
5.2.3	Stoichiometric polarization measurements	82
5.2.4	Stability of dislocations	85
5.2.5	Spark plasma sintering sample without dislocations	85
5.3	Discussion	89
5.3.1	Grain size dependence of deformation mechanism maps	89
5.3.2	Space charge model	89
5.4	Conclusions on polycrystalline TiO ₂	92
6	Y-doped/decorated polycrystalline TiO₂	95
6.1	Sample preparation	95
6.2	Defect characterization	96
6.2.1	Acceptor decorated TiO ₂	96
6.2.2	Acceptor doped TiO ₂	97
6.3	Electrical characterization	99
6.3.1	Conventionally sintered and spark plasma sintered 0.1 mol % Y doped TiO ₂	99
6.3.2	Spark plasma sintered 0.1 mol % Y decorated TiO ₂	103
6.4	Discussion	106
6.5	Chapter conclusions	110
II	Results and discussion on 2-D defects	113
7	Symmetric tilt boundaries	115
7.1	Structural characterization - TEM	115
7.2	Electrical characterization - EIS	121
7.2.1	Undoped Σ5 and 6° symmetric tilt boundaries	122
7.2.2	Y-decorated Σ5 symmetric tilt boundary	123
7.2.3	Y-decorated 3° symmetric tilt boundary	127
7.2.4	Discussion	129
7.3	Chapter conclusions	131

CONTENTS

8 Summary	133
References	137

List of Figures

1.1	Interface effects on the electrical properties	2
1.2	Size effects and strain effects on the electrical properties	3
2.1	Rutile and anatase crystal structures	8
2.2	Schematic representation of dislocations	11
2.3	Schematic representation of conditions for viewing a dislocation in TEM	11
2.4	Kroeger-Vink diagram of acceptor doped TiO ₂	19
2.5	Kroeger-Vink diagram for donor doped TiO ₂	21
2.6	Nyquist plot for a polycrystalline ionic solid.	24
2.7	Schematic representation of structural and electrical boundaries for ionic solids.	25
2.8	Schematic representation of layer models	25
2.9	Schematic representation of (a) two phase parallel layer model (equivalent to bulk and parallel dislocations in single crystals) and (b) equivalent electrical circuit.	26
2.10	Brick layer model	27
2.11	Schematic representation of space charge layer and the corresponding EIS	28
2.12	Schematic representation of space charge model for a combined case.	31
3.1	XRD pattern for TiO ₂ powders after sol-gel synthesis (anatase phase) and after sintering (rutile phase).	34
3.2	SEM images of CS TiO ₂ samples	36
3.3	SEM images of SPS TiO ₂ samples	38

LIST OF FIGURES

3.4	Deformation mechanism map for rutile	43
3.5	Orientation of single crystals for making $\Sigma 5$ and 6° symmetric tilt TiO ₂ boundaries	45
3.6	Schematic drawing of the diffusion bonding furnace used for preparing bicrystals	46
4.1	Bright field TEM image of pristine TiO ₂ crystal, specimen prepared from [001] orientation with beam axis parallel [001].	54
4.2	Schematic representation of crystal orientation with respect to the applied load. Specimens for TEM and electrical characterization are also represented.	55
4.3	Bright field TEM image of [001] TiO ₂ crystal, specimen prepared from plan view with beam axis parallel to [001].	56
4.4	(a) Bright field TEM image of [001] sample prepared from cross- section, two beam condition with diffraction vector = (-110) oper- ating along with beam axis parallel to [110]. (b) Dark field image from the same location.	57
4.5	(a) TEM-bright field image of [110] plan view sample with two beam condition operating with beam axis parallel to [110] and [001] diffrac- tion vector. (b) Dark field image from the same location.	58
4.6	TEM-bright field image of [110] plan view sample with beam parallel to [110] (a) two beam condition with only [001] reflex operating (b) [110] reflex operating.	58
4.7	TEM-BF image of [110] sample prepared from the cross-section with two beam condition operating with $\mathbf{g}=(-110)$ and beam axis parallel to [001]. Insets show the diffraction pattern of the corresponding regions.	59
4.8	EIS of 001 crystals with and without dislocations.	61
4.9	Electrical conductivity as a function of pO_2 for 001 crystals with and without dislocations	61
4.10	Arrhenius plots for 001 crystals with and without dislocations	64
4.11	EIS of 110 crystals with and without dislocations.	65

LIST OF FIGURES

4.12	Electrical conductivity as a function of $p\text{O}_2$ for 110 crystals with and without dislocations	65
4.13	Arrhenius plots for 110 crystals with and without dislocations	66
4.14	DC polarization curve for the [001] single crystal with dislocations.	67
4.15	Electrical conductivity as a function of $p\text{O}_2$ for 001 crystal with ion blocking Au electrodes.	68
4.16	Normalized ^{18}O concentration profiles for 001 and 110 oriented crystals	69
4.17	Normalized ^{18}O concentration profile and fit result for [001]	70
4.18	Bulk oxygen tracer diffusion coefficients obtained for (a) [001] crystals and (b) [110] crystals as a function of inverse temperature at 0.5 bar $p\text{O}_2$	71
4.19	(a). Schematic representation of the slip system and measurement axis (only one plane is showed for better view). (b) A possible space charge model for p-type and n-type.	72
5.1	SEM images of polycrystalline TiO_2 prepared by CS and SPS	76
5.2	TEM images of polycrystalline samples with dislocations	77
5.3	Impedance spectrum measured at 550 ° C in 1 bar $p\text{O}_2$ for the CS sample sintered at 1300 ° C for 5 h in air, inset shows the equivalent circuit used for fitting the data with $\psi_{HF}=0.95$, $\psi_{LF}=0.6$	78
5.4	Electrical conductivity as a function of $p\text{O}_2$ for SPS and CS undoped samples	80
5.5	Arrhenius plot for the SPS sample (with dislocations) and the CS sample (without dislocations)	80
5.6	EIS of the SPS polycrystalline TiO_2 with dislocations.	81
5.7	Partial ionic conductivity as a function of $p\text{O}_2$ for the SPS sample with dislocations, compared to the total conductivity.	84
5.8	Arrhenius plot for the total and partial ionic conductivity of the SPS sample with dislocations.	84
5.9	EIS of the SPS sample with dislocations after annealing treatment.	86

LIST OF FIGURES

5.10 (a) Total electrical conductivity as a function of pO_2 for the SPS sample with dislocations before ('disl-SPS') and after annealing at 1300 °C for 5 h ('SPS-anneal'). (b) Arrhenius plot for the same samples in 1 bar oxygen. The slopes in the low- pO_2 regime are drawn according to the values expected from the bulk defect chemical model.	87
5.11 EIS of the SPS sample without dislocations.	88
5.12 Total electrical conductivity as a function of pO_2 for the SPS sample with negligible dislocations, pressed at 40 MPa, 850 °C for 10 min and the CS sample (without dislocations) for comparison. The slopes in the low- pO_2 regime are drawn according to the values expected from the bulk defect chemical model.	88
5.13 Deformation mechanism map for TiO_2 as function of grain size.	90
5.14 Schematic illustration of dislocations in TiO_2 ceramics, with respect to sintering techniques	91
5.15 Dislocation structure in rutile with annealing treatment	92
6.1 SEM images of 0.1 mol % Y-doped and decorated polycrystalline TiO_2	96
6.2 Bright field TEM images of 0.1 mol% Y-decorated polycrystalline TiO_2	97
6.3 Bright field TEM images of 0.1 mol% Y-doped polycrystalline TiO_2 without dislocations	98
6.4 Bright field TEM images of 0.1 mol% Y-doped polycrystalline TiO_2 with few dislocations	98
6.5 EIS spectrum for CS 0.1 mol % Y doped TiO_2	99
6.6 Electrical conductivity as function of pO_2 for 0.1 mol % Y doped CS and SPS samples	100
6.7 Arrhenius plot for the CS and SPS 0.1 mol % Y doped TiO_2 samples (with negligible dislocations).	101
6.8 EIS spectrum for SPS 0.1 mol % Y doped TiO_2	102
6.9 EIS spectrum for SPS 0.1 mol % Y decorated TiO_2	104
6.10 Electrical conductivity as function of pO_2 for 0.1 mol % Y decorated SPS samples	105
6.11 Arrhenius plot for the SPS 0.1 mol % Y decorated and undoped TiO_2 samples with dislocations.	105

LIST OF FIGURES

6.12	Summary of conductivity plots of 0.1 mol % Y doped and decorated TiO ₂ samples.	106
6.13	Electrical conductivity as function of pO_2 for 0.1 mol % Y decorated SPS samples after a long anneal	108
6.14	Arrhenius plot for the SPS 0.1 mol % Y decorated TiO ₂ samples before and after annealing at 1000 °C for 10 h.	109
6.15	Schematic representation of oxygen vacancy defect profile in the bulk and space charge zone for the SPS 0.1 mol % Y decorated TiO ₂ sample with increase in annealing time.	110
6.16	Bright field TEM images of 0.1 mol % Y-decorated polycrystalline TiO ₂ after annealing	111
7.1	Schematic cartoon showing the TEM specimen and its orientation with respect to the electron beam axis in the microscope.	116
7.2	Optical microscopy images of TEM specimens	117
7.3	A TEM bright field image of the $\Sigma 5$ undoped symmetric (210)[001] tilt boundary.	117
7.4	HRTEM image of the $\Sigma 5$ undoped symmetric tilt boundary, insets are the diffraction patterns of respective crystals obtained by fast Fourier transform.	118
7.5	TEM bright field image of the $\Sigma 5$ symmetric tilt undoped boundary, the boundary plane was slightly tilted for a better view of dislocations.	119
7.6	HRTEM image of the $\Sigma 5$ symmetric tilt Y-decorated boundary, insets are the diffraction patterns of respective crystals obtain by fast Fourier transform.	120
7.7	HRTEM image for the 6° undoped and Y decorated symmetric tilt boundary	120
7.8	TEM bright field images for the 6° symmetric tilt undoped and 0.5 nm Y decorated grain boundary	121
7.9	EIS for undoped $\Sigma 5$ and 6° symmetric tilt boundary of TiO ₂ bicrystals	123
7.10	Electrical conductivity vs. pO_2 for undoped $\Sigma 5$ and 6° symmetric tilt boundary TiO ₂ bicrystals	124

LIST OF FIGURES

7.11 Arrhenius plot for undoped $\Sigma 5$ and 6° symmetric tilt boundary TiO_2 bicrystals	124
7.12 EIS for Y-decorated $\Sigma 5$ symmetric tilt boundary of TiO_2 bicrystal	125
7.13 Electrical conductivity vs. $p\text{O}_2$ for Y-decorated $\Sigma 5$ symmetric tilt boundary of TiO_2 bicrystal	126
7.14 Arrhenius plot for undoped and Y-decorated $\Sigma 5$ symmetric tilt boundary TiO_2 bicrystals.	126
7.15 EIS for Y-decorated 6° symmetric tilt boundary of TiO_2 bicrystal	127
7.16 Electrical conductivity vs. $p\text{O}_2$ for Y-decorated 6° symmetric tilt boundary of TiO_2 bicrystal	128
7.17 Arrhenius plot for undoped and Y-decorated 6° symmetric tilt boundary of TiO_2 bicrystals.	128
7.18 Impedance spectra for $\Sigma 5$ Y decorated tilt boundary sample before and after thickness reduction.	129
7.19 Impedance spectra for $\Sigma 5$ undoped tilt boundary and $[001]$ single crystal under an applied DC bias of 0 V to 0.8 V, inset shows the plot for electrical conductivity as a function of DC bias. Each spectra was collected at an interval of 30 min.	131

List of Tables

2.1	Various properties of TiO_2 for anatase and rutile	9
2.2	Equilibrium constants for all possible defect reactions in TiO_2	21
2.3	Migration enthalpies for point defects in TiO_2	22
3.1	Chemical analysis (ICP-OES) of the materials used in this work.	35
3.2	Creep data for TiO_2	44
7.1	Effect of sample thickness on the electrical parameters	130

LIST OF ABBREVIATIONS AND SYMBOLS

List of abbreviations and symbols

$\langle uvw \rangle$	family of directions	Q_{core}	core charge density
$\Delta\phi^o$	space charge potential	z_i	charge of the defect i
ϵ^\bullet	strain rate	A'_{Ti}	trivalent acceptor dopant on titanium sublattice
λ	Debye length	D_{Ti}^\bullet	pentavalent donor dopant on titanium sublattice
ω	angular frequency given as $1/(RC)$	O_O^\times	oxygen on oxygen sublattice
ψ_i	geometry factor for constant phase element, subscript $i =$ HF-high frequency, LF-low frequency	pO_2	oxygen partial pressure
σ	conductivity	\mathbf{b}	Burgers vector
ϵ_r	relative permittivity	\mathbf{g}	diffraction vector
$\{hkl\}$	family of planes	m	oxygen partial pressure exponent
c_i	concentration of the defect i	$Ti_i^{\bullet\bullet\bullet\bullet}$	titanium ion on interstitial site
D^*	oxygen tracer diffusivity	$Ti_i^{\bullet\bullet}$	titanium interstitial with a trapped electron
D_i	defect diffusivity of species i	Ti_{Ti}^\times	titanium on titanium sublattice
n	concentration of electrons	$V_O^{\bullet\bullet}$	oxygen vacancy
O_i''	oxygen on interstitial site	$V_{Ti}^{\prime\prime\prime\prime}$	titanium vacancy
p	concentration of holes	AC	alternating current
		C	capacitor
		CPE	constant phase element
		CS	conventional sintering
		CS-dop	conventional sintered Y doped sample
		DC	direct current
		disl.	sample with dislocations
		EIS	electrochemical impedance spectroscopy
		GB	grain boundary
		HF	high frequency semicircle in impedance spectroscopy

LIST OF ABBREVIATIONS AND SYMBOLS

LF	low frequency semicircle in impedance spectroscopy	SPS-dec	spark plasma sintered Y decorated sample
R	resistor	SPS-dop	spark plasma sintered Y doped sample
SAD	selected area diffraction	TEM	transmission electron microscope
SEM	secondary electron microscopy	Z	impedance
SIMS	secondary ion mass spectroscopy		
SPS	spark plasma sintering		

Zusammenfassung

TiO₂ ist ein vielversprechendes Material für zahlreiche technologische Anwendungen wie Solarzellen, Wasserspaltung, Datenträger und Li-Ionen-Batterien. Trotz der unterschiedlichen Funktionen spielen in all diesen Technologien die Punktdefekte in TiO₂ eine entscheidende Rolle. Die Punktdefektchemie von TiO₂ wurde in den letzten Jahrzehnten ausgiebig untersucht. Eine Änderung der Konzentration der Punktdefekte wurde hierbei entweder durch aliovalente Dotierung oder nanoskalige Größeneffekte erreicht. Beide Methoden sind auf dem Gebiet der Festkörperionik weit verbreitet, jedoch auch limitiert in ihrer Verwendung, zum Beispiel aufgrund begrenzter Löslichkeiten von Dotieratomen und Kornwachstum schon bei moderaten Temperaturen. Eine weitere Stellschraube, um Punktdefektkonzentrationen zu verändern, ist das Einbringen von strukturellen Modifikationen wie ein-dimensionale Liniendefekte (Versetzungen) oder zwei-dimensionale planare Defekte (Korngrenzen). Für einen ionischen Festkörper wird angenommen, dass diese ausgedehnten Defekte elektrisch geladen sind und sich folglich lokal die Punktdefektkonzentrationen in Raumladungszonen ändern, um global die Ladungsneutralität zu erhalten. Der Einfluss von Versetzungen auf die Punktdefektkonzentrationen – und damit auf die elektrischen Eigenschaften – in TiO₂ ist wenig untersucht. Die vorliegende Arbeit untersucht dies im Detail anhand von TiO₂ in der Rutil-Struktur als Modellmaterial.

Die Versetzungen wurden durch uniaxiale Kompression bei erhöhten Temperaturen in TiO₂-Einkristalle sowie polykristalline Proben eingebracht. Aus dem Verformungsmechanismus-Diagramm für TiO₂ wurde eine geeignete Kombination aus Temperatur und Druck für Krie-

chen durch Versetzungen gewählt. Die Bildung und Wanderung von Versetzungen ist stark abhängig von den Materialeigenschaften; im Falle von TiO_2 erlauben verschiedene Faktoren wie vergleichbare Mobilitäten von Kationen (Ti-Zwischengitteratome) und Anionen (Sauerstoffleerstellen), nicht zu hohe Schmelztemperatur und nicht zu hoher Schubmodul im Unterschied zu anderen Halbleitern mit großer Bandlücke die Bildung von Versetzungen bei moderaten Bedingungen (typischerweise 1000 °C , 40 MPa für Einkristalle und 925 °C , 400 MPa für polykristalline Materialien). Im Temperaturbereich $350 - 550\text{ °C}$, in dem die Leitfähigkeitsmessungen durchgeführt wurden, sind die Versetzungen typischerweise nicht beweglich und die gemessenen Eigenschaften gut reproduzierbar. Die eingebrachten Versetzungen wurden mit Transmissionselektronenmikroskopie untersucht. Diese zeigte, dass die Versetzungen bevorzugt auf der $\{110\}$ Gleitebene liegen. Als Richtung für die elektrischen Messungen wurden $[001]$ und $[110]$ gewählt, d.h. parallel bzw. senkrecht zu den Versetzungen. Die elektrischen Eigenschaften wurden in Abhängigkeit der Versetzungsdichte, der Temperatur und des Sauerstoffpartialdrucks untersucht. Mit zunehmender Versetzungsdichte ändert sich die Leitfähigkeit von TiO_2 bei moderaten Temperaturen (550 °C) und hohen Sauerstoffpartialdrücken (1 bar bis 10^{-5} bar) von der üblichen Loch-Leitfähigkeit (p-Typ Halbleiter) zu einer überwiegend ionischer Leitfähigkeit. Außerdem wurden Sauerstoffisotopenaustausch mit nachfolgender Sekundärionen-massenspektroskopie durchgeführt, um bei der ionischen Leitfähigkeit zwischen dem Transport von Sauerstoff-Leerstellen und Titan-Zwischengitterionen zu unterscheiden. Ein Vergleich der Ergebnisse dieser verschiedenen Charakterisierungsmethoden zeigt, dass die erhöhte ionische Leitfähigkeit eine Folge der negativen Ladung der Versetzungskerne und somit der Anreicherung von positiven Ladungsträgern in den anliegenden Raumladungszonen ist. Diese Interpretation wird ferner durch die Tatsache gestützt, dass die Konzentrationen der ionischen Defekte mit höherer Ladung in größerem Maße beeinflusst werden als die elektronischen Defekte.

Ähnliche Effekte von Versetzungen auf die elektrischen Eigenschaften

werden auch in polykristallinem TiO_2 beobachtet. Die Versetzungsbildung hat einen dauerhaften Einfluss auf die elektrischen Eigenschaften, und stets wird die ionische Leitfähigkeit gegenüber der elektronischen Leitfähigkeit erhöht. Die partielle ionische Leitfähigkeit der Probe wurde mittels einer Elektrodenkonfiguration nach Hebb-Wagner gemessen. Für TiO_2 wird bei hohen Sauerstoffpartialdrücken eine ungewöhnlich große ionische Überführungszahl gefunden. Außerdem wurden die Einflüsse von sowohl homogener Akzeptordotierung als auch selektiver Dekorierung der Korngrenzen (0.1 mol% Y) auf die Bildung von Versetzungen untersucht. In den homogen dotierten Proben wurden aufgrund von Mischkristallverfestigung keine Versetzungen festgestellt, so dass sich diese Proben mit der üblichen Defektchemie von akzeptor-dotiertem TiO_2 beschreiben lassen. Im Fall der Dekoration wurden Versetzungen in der gesamten Probe erzeugt und eine sauerstoffpartialdruckunabhängige ionische Leitfähigkeit festgestellt, typischerweise im Bereich 1 bis 10^{-7} bar. Der Einfluss der Versetzungen ist dauerhaft – selbst eine Temperaturbehandlung bei 1300 °C für 5 h konnte die Versetzungsdichte nicht maßgeblich reduzieren. Die gemessenen Änderungen der elektrischen Eigenschaften sind sehr stabil und reproduzierbar innerhalb eines großen Temperaturbereichs.

Die Kerne der Korngrenzen von Oxiden mit Perowskit/Fluorit-Struktur und großer Bandlücke wie SrTiO_3 , CeO_2 , ZrO_2 (Y stabilisiert) sind typischerweise wegen der Anwesenheit von Überschuss-Anionenleerstellen positiv geladen. Die positiven Korngrenzkern hemmen aufgrund der Bildung von Verarmungsschichten den Transport positiv geladener Defekte wie Löcher, Kationen-Zwischengitteratomen und Anionen-Leerstellen. Im Fall von TiO_2 können sich jedoch auch negative Korngrenz- oder Versetzungskerne bilden. Aus diesem Grund werden im zweiten Teil dieser Arbeit die Korngrenzen von TiO_2 -Bikristallen mit symmetrischen Kleinwinkelkorngrenzen untersucht. Die beiden Hauptorientierungen ($\Sigma 5$ (210) [001] und 6° [001] symmetrische Kleinwinkelkorngrenzen), werden insbesondere bezüglich der elektrischen Eigenschaften der Korngrenzen untersucht. Mittels hochauflösender Transmissionselektronenmikrosko-

pie wird ersichtlich, dass die symmetrische Kleinwinkelkorngrenze einer periodischen Anordnung von Versetzungen nach Franks Regel entspricht. Es wird ferner gezeigt, dass die elektrischen Eigenschaften beider Korn- grenzorientierungen ähnlich sind (nicht blockierend für den Transport von Löchern). Dies deutet daraufhin, dass die symmetrischen Kleinwin- kelkorngrenzen in TiO_2 sich deutlich von denen in anderen Oxiden mit großer Bandlücke unterscheiden, die üblicherweise positiv geladen sind. Zusammenfassend zeigt diese Arbeit über TiO_2 , dass Versetzungen zur lokalen Modifizierung der elektrischen Eigenschaften in einer Dimension eingebracht werden können. Dies ermöglicht einen alternativen Weg zur gezielten lokalen und globalen Veränderung der elektrischen Eigenschaf- ten von ionischen Festkörpern, der zusätzliche Freiheitsgrade bietet, um die ionischen/elektronischen Eigenschaften von verschiedenen Funktions- keramiken anzupassen.

Abstract

TiO₂ is a promising material for many technological applications such as solar cells, water splitting, memory devices and Li-ion batteries. Even though the functionalities are diverse depending on their applications, the point defects in TiO₂ play a decisive role in all these technologies. The point defect chemistry of TiO₂ was intensively studied in the last few decades and so far modification of point defect concentrations was attained by either aliovalent doping or by nano size effects. Both methods are widely applied in the field of solid state ionics, however, with limitations such as limited solubility of dopants grain growth effects already at moderate temperatures. Another adjusting screw for altering point defect concentrations is by incorporating microstructural modifications in the material such as one dimensional line defects (dislocations), or two dimensional planar defects (grain boundaries). In ionic solids, these extended defects should be charged, and in order to maintain global charge-neutrality, they will locally modify the point defect concentration in space charge zones. The influence of dislocations on point defect concentrations in oxides, and thus the electrical properties, has not been studied much in TiO₂ for far. The present thesis gives such a detailed investigation using TiO₂ in the rutile structure as model material.

Dislocations were created in TiO₂ single crystals as well as polycrystalline materials by uniaxial compression at elevated temperature. Based on the creep deformation map for TiO₂, a suitable combination of temperature and pressure was chosen to activate dislocation creep. The dislocation formation and migration strongly depends on the material properties; in case of TiO₂ various factors – such as comparable cation (Ti interstitials) and anion (oxygen vacancies) mobilities, comparably low melting temperature and shear modulus when compared to other wide band gap

oxides – allows for their formation at moderate conditions (typically at 1000 °C, 40 MPa for single crystals and 925 °C, 400 MPa for polycrystalline materials). In the temperature range (350 °C to 550 °C) in which the conductivity measurements have preformed, dislocations are typically immobile and therefore measured properties well reproducible. Dislocations generated by this process are characterized by transmission electron microscopy and it is found that the dislocations favorably lie on {110} slip planes. Based on the slip planes, electrical measurement axis is chosen to be [001] and [110], directions parallel and perpendicular to the dislocations respectively. Electrical properties are also studied as a function of dislocation density, temperature and oxygen partial pressure. With increasing density of dislocations the conductivity type of TiO₂ at moderate temperatures (550 °C) and high oxygen partial pressures (1 bar to 10⁻⁵ bar) changes from usual hole conductivity (p-type semiconductor) to predominant ionic conductivity. Further, to discriminate between oxygen vacancy and titanium interstitial transport in the partial ionic conductivity, oxygen isotope exchange and SIMS analysis were performed. The comparison of the results from these characterization techniques shows that the enhanced ionic conductivity is due to negatively charged dislocation cores and adjacent space charge accumulation zones of positive carriers. This interpretation is further supported by the fact that the concentrations of ionic defects with their higher charge are influenced to a much greater degree than electronic defects. Similar effects of dislocations on the electrical properties are observed for polycrystalline TiO₂. Dislocation creation have a persistent effect on the electrical properties with the ionic conductivity of the samples increased more strongly than the electron hole conductivity. The partial ionic conductivity of the sample is measured by Hebb-Wagner type electrodes, and an unusually high ionic transference number is observed for TiO₂ at high oxygen partial pressures. Further, effects of acceptor dopant (0.1 mol % Y) on the dislocation generation is studied by either homogeneously doping or by selectively decorating grain boundaries. No dislocations were observed in homogeneously doped samples

due to solid solution strengthening, which therefore resulted in a regular defect chemistry as expected for an acceptor doped TiO_2 . In case of decorated samples, very similar to the undoped samples, dislocations are generated throughout the sample and once again a oxygen partial pressure independent ionic conductivity is observed, typically in the range of 1 bar to 10^{-7} bar. The effect of dislocations is very persistent - even a high temperature treatment at 1300 °C for 5 h did not anneal much of the dislocation density. Hence, the observed changes in electrical properties are very stable and reproducible over a wide temperature range. Grain boundary cores of perovskite and fluorite structured oxides with large band gaps such as SrTiO_3 , CeO_2 , ZrO_2 (Y stabilized) are typically positively charged due to the presence of excess anion vacancies. Positive grain boundary cores impede the transport of positively charged defects such as holes, cation interstitials and anion vacancies by formation of depletion layers. However, in case of TiO_2 also negative grain boundary or dislocation core charges may form. For this reason, grain boundaries of TiO_2 bicrystals with symmetric tilt boundaries are investigated in the second part of the study. Two main orientations viz. $\Sigma 5$ (210)[001] and 6° [001] symmetric tilt boundaries are investigated with a focus on the boundary electrical properties. High-resolution transmission electron microscopy revealed that the symmetric tilt grain boundaries correspond to a periodic array of dislocations with a spacing according to Frank's rule. It is also observed that the electrical conductivity in two boundary orientations are similar and the boundaries are not blocking for the transport of holes. This indicates that the symmetric tilt boundaries in TiO_2 are not similar to other wide band gap oxides, but are usually positively charged.

To summarize, it is quite obvious from this work on TiO_2 that dislocations can be used as a means of modifying defect transport of ionic solids locally and globally, hence, allowing additional degrees of freedom for tuning the ionic/electronic properties of various functional oxides.

1

Introduction and motivation

Point defects play a critical role in crystalline solids; in fact, all physical, chemical and structural properties are influenced by these zero dimensional defects. In ionic solids, electrical properties (both ionic and electronic transport) are mainly determined by the concentration of point defects and their mobilities. Any modification in these defects leads to a variation in electrical properties. Therefore, chemical doping (aliovalent impurities) has been the first choice for modifying the electrical properties of ionic solids. The advantages of chemical doping are undebatable, and this is still a preferred technique. However, a major limitation comes from the solubility limit of the dopant, especially for tuning electrical properties of relatively close packed ionic solids such as rutile type TiO_2 . This is typically in the range of 10-15 % for donor dopants like Nb [1], and typically lower for acceptor dopants - only upto 1 % for Al and Ga [2,3] and only 0.1 % percent for Y [4]. The low acceptor solubility in TiO_2 is attributed to the large ionic radii compared with donors.

Additionally, the presence of boundaries or interfaces in ionic solids would lead to locally modified electrical properties (due to thermodynamic reasons) compared to the bulk defect chemistry [5]. The effect of heterogeneous interfaces on the electrical properties was first observed in the $\text{LiI-Al}_2\text{O}_3$ two phase system, with conductivities that are abnormally high in comparison with the parent phases [6] as shown in Figure 1.1a. Similarly, various other systems [7,8] were found to show such effects and the primary reason for this was attributed to core effects (mobility and concentration of defects are modified due to the core structure) and/or space charge effects (only concentration of defects are modified) [5]. Another example in this category

1. INTRODUCTION AND MOTIVATION

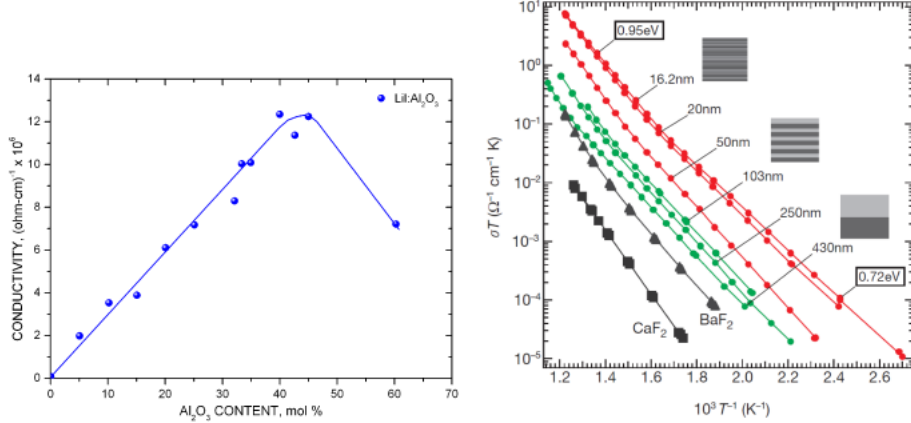


Figure 1.1: (a) Variation of electrical conductivity of $\text{LiI}:\text{Al}_2\text{O}_3$ electrolyte as a function of Al_2O_3 content, reproduced from ref. [6]. (b) In-plane ionic conductivity of epitaxially grown $\text{CaF}_2/\text{BaF}_2$ heterolayers as a function of temperature and film thickness, reprinted from ref. [9].

are epitaxially grown $\text{CaF}_2/\text{BaF}_2$ heterolayers [9] as shown in Figure 1.1b. In this system, not only the conductivity is higher than in the pure phases, but increases with decreasing layer thickness. This is a striking example of space charge effects at the interfaces, which demonstrated that overlapping space charge zones lead to modified electrical properties (non trivial size effect).

The advent of nano-ionics [10, 11] emphasized these effects to a greater extent. In nanocrystalline materials, interface properties can dominate over the bulk and lead to modified electrical properties via space charge regions. Supporting this concept, several systems were found with electrical properties very different from their bulk or microcrystalline properties. A striking example in this respect is nanocrystalline SrTiO_3 as shown in Figure 1.2a, where the p-type conductivity is lowered by 3 orders of magnitude while n-type conductivity increased by more than 2 orders of magnitude, the oxygen vacancy conductivity is lowered by at least 4 orders of magnitude and the $p\text{O}_2$ of the conductivity minimum is shifted by 12 orders of magnitude compared to a microcrystalline sample [12]. In case of nominally undoped CeO_2 , the predominant ionic conductivity is changed to electronic conductivity when the grain size is reduced below 30 nm [13–15]. In both these examples, positively charged grain boundary cores accumulate negatively charged point defects and deplete positively charged point defects in the adjacent space charge zones, resulting

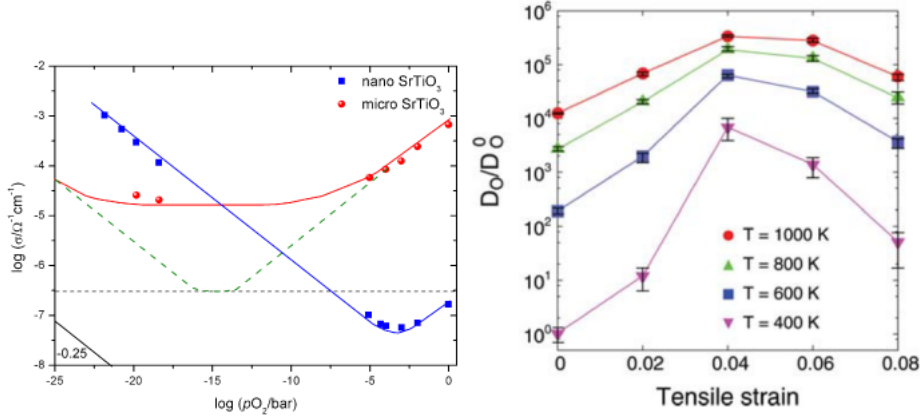


Figure 1.2: (a) Electrical conductivity as a function of $p\text{O}_2$ at 547°C for nanocrystalline and microcrystalline SrTiO_3 , according to ref. [12]. (b) Simulated oxygen diffusivity (D_O) variation with lattice strain for YSZ at different temperatures, D_O^0 is the oxygen diffusivity at zero strain. (plot obtained from [17]).

in modified electrical properties. Predominant ionic conductivity was observed in nanocrystalline anatase TiO_2 , while n-type conductivity was found in microcrystalline rutile TiO_2 [16]. From these examples, it is convincing that heterogeneous doping by interfaces (either by two phase admixture or by size effects) can be considered as an alternative way for tuning electrical properties, complementary to chemical doping. However, achieving dense but nanocrystalline materials is challenging, and use of these materials is often restricted to a lower temperature to avoid excessive grain growth.

All examples mentioned so far are 2-D defects. Apart from these, heterogeneous doping via introduction of one-dimensional defects by mechanical effects is a further option. This one-dimensional doping means generation of dislocations (line defects) as a consequence of plastic deformation*. One of the key features of dislocations is that they take an intermediate place between kinetically frozen interfaces and thermodynamically equilibrated point defects, which is least studied in the context of electrical properties of ionic solids. In contrast to metals, dislocations in ionic solids are usually charged, due to the ionic nature of point defects. For example, 111 planes in NaCl consists of alternate layers of Na^+ and Cl^- , therefore dislocations on these planes possess either a positive or negative core charge depending on the

*also some elastic distortion, i.e. strain, will be introduced by mechanical treatment

1. INTRODUCTION AND MOTIVATION

extra plane termination (on the slip plane on which extra plane terminates) [18]. Dislocations even on neutral planes are also expected to be charged due to their extension on other other planes (such as jogs) for energetic reasons. (e.g., in NaCl, edge dislocations formed on the 110 planes are neutral, however formation of jogs makes them charged [19]). In general, dislocation cores on structurally distorted regions (even without jogs) will be charged due to defect segregation as formation energies of charged defects in these regions differ from the bulk. A similar situation can be expected in all the ionic solids, as it is convincing from various other systems such as ZnO, ZnS, ZnSe, CdS, CdSe, ZnTe, BaTiO₃, SrTiO₃ and ZrO₂:Y [20–22], that dislocations are often charged. Further, dislocations can be either negatively charged or positively charged. In case of alkali halides, Whitworth [19] observed that dislocation core charges are likely to become negative by doping with donors on cation sites and positive by acceptor doping on anion sites.

Owing to these excess charges, dislocations can vary the point defect concentrations very locally in one dimensions. Additionally dislocations often generate lattice strain which further influence the electrical properties. More recent works on understanding the effect of lattice strain on the interface conductivity lead to several interesting findings [17, 23–25]. In Figure 1.2b, effect of lattice strain on the oxygen diffusivity of YSZ simulated at different temperatures based on DFT calculations is shown. Increase in strain lead to enhanced oxygen diffusivity due to lowered migration enthalpy.

Therefore, at dislocations one can expect space charge (modifying carrier concentrations) and strain effects (altering defect mobility). A synergistic combination of both could influence point defect transport drastically. In regard to the current challenges, understanding these effects may lead to improved electrochemical and solid state electronic/ionic devices.

1.1 Choice of material and outline of thesis

To investigate these effects, a model material is necessary where extended defects are not only readily created but also will be stable at the measurement or testing conditions. The first choice for these experiments is TiO₂ based on its mobile anion and cation defects [26] which will ameliorate the creation of extended defects,

1.1 Choice of material and outline of thesis

and additionally, its melting point at 1855 °C enabling the extended defects persist at moderate temperatures. Apart from this scientific interest, TiO₂ is also a technologically relevant material with diverse applications ranging from biological to energy applications. Therefore, understanding the effects of extended defects on the transport properties of point defects in TiO₂ has a paramount importance in several fields of science and technology.

Since the point defect chemistry of TiO₂ was extensively studied in last few decades [26–38], numerous data are available on the electrical properties. A high density of 1-D defects (dislocations) in crystalline materials can be consistently generated by mechanical deformation processes*. The mechanical properties of TiO₂ were also extensively studied beginning of the early 70's [39–45] and in brief, it was concluded that irrespective of the compression axis the favorable plane for dislocation generation is always on the 110< 001 > and -101< 101 > slip systems. Therefore, TiO₂ is a very suitable material, with very well studied point defects and mechanical properties, as a basis for this work.

The challenge in the present thesis is to investigate the transport properties of point defects in presence of dislocations. So far no such work is available (to author's knowledge) in wide band gap ceramics making this contribution even more worthwhile. For this reason, and for the purpose of a better understanding, samples with extended defects are always compared with respective samples free[†] of extended defects. Based on comparing and contrasting the samples, probable mechanisms for the observed effects will have to be discussed.

The influence of dislocations in various forms of TiO₂ such as single crystals, polycrystalline and doped/decorated polycrystalline samples on the electrical properties of TiO₂ is extensively studied in this work. Also the influence of 2-D defects viz. symmetric tilt boundaries on the electrical properties of TiO₂ is discussed in this thesis. In the discussion main emphasis has been laid on the defect transport properties.

The necessary concepts are set out in Chapter 2 "Theoretical background" providing a brief introduction to the classification of defects and the necessary tools for

*dislocations are unavoidable in any crystalline materials, however, a low density would not result in any significant effects. Therefore, a high densities are always preferred to study their effects.

[†]strictly speaking: with insignificant concentration of extended defects

1. INTRODUCTION AND MOTIVATION

characterizing them. The bulk point defect chemistry of TiO_2 , which is often referred to throughout this thesis is summarized in this chapter. Electrical properties are characterized by electrochemical impedance spectroscopy (background is given in Section 2.4), which is the state-of-the-art method for resolving different electrical processes that occur at distinct relaxation times (or frequency). The method will also allow drawing conclusions on the dislocation core charges. The excess charges in the extended defects will lead to a spatial distribution of defects known as space charge regions. These regions become decisive when the extended defects form a continuous network in the system. Different possible types of space charge models are briefly summarized in section 2.5.

In Chapter 3, experimental details for synthesizing TiO_2 polycrystalline ceramics as well as bicrystals with symmetric tilt boundaries are given. Since the major portion of this thesis deals with dislocations, techniques to create dislocations in single crystals as well as polycrystalline materials are discussed in detail (Section 3.5). Electrical and non-electrical characterization tools (e.g. transmission electron microscopy) are referred to as well in this chapter.

Results and discussions of this work are categorized into two parts based on the defect dimensions. Part-I, constitutes a major portion of this thesis, deals with dislocations and their influence on the electrical properties. The effects of dislocation in single crystals are discussed in Chapter 4, effects in polycrystalline TiO_2 are discussed in Chapter 5 and Chapter 6 highlights the effects of acceptor doping and decoration on dislocation generation and electrical properties of polycrystalline TiO_2 . Part-II focus on the effects of planar defects (i.e., symmetric tilt boundaries) on the electrical properties of TiO_2 . Boundary characterization by transmission electron microscopy and electrical characterization by impedance spectroscopy are discussed in Chapter 7.

2

Theoretical background

2.1 Introduction to TiO_2

Titanium dioxide or titania (TiO_2) is a wide band gap semiconductor commonly found in the form of one of the two polymorphs viz. anatase and rutile. There are at least six other polymorphs [46–51] known for TiO_2 . Among all of them, rutile is known to be the thermodynamically stable phase except for the nanometer scale (and possibly very low temperatures [52,53]) for which anatase is known to be stable [53–55]. Various properties of these two phases are summarized in the Table 2.1. Rutile and anatase are tetragonal structures, where each titanium atom is octahedrally coordinated by six oxygen atoms and each oxygen atom is coordinated by three titanium atoms as shown in Figure 2.1. In both structures, the TiO_6 octahedron is slightly distorted [56] with two of the six Ti-O bonds slightly larger (see bond lengths in Table 2.1). The key difference comes from the connection of its octahedra, in rutile they share two edges with other octahedra and in anatase they share four edges. The experimentally determined band gap for rutile and anatase is 3.1 eV and 3.23 eV respectively. Among several wide band gap oxides TiO_2 is one of the technologically most important materials with diverse applications in several fields - as shown by the high number of publications [57], which is over 13000 within one year (2010-11). Some of the key applications include water splitting [58], photocatalysis [59], photoelectrochemical properties [60], dye sensitized solar cells [61], memristors (nonvolatile memory devices) [62,63], gas sensors [64] and anodes

2. THEORETICAL BACKGROUND

for Li and Na ion batteries [65, 66].

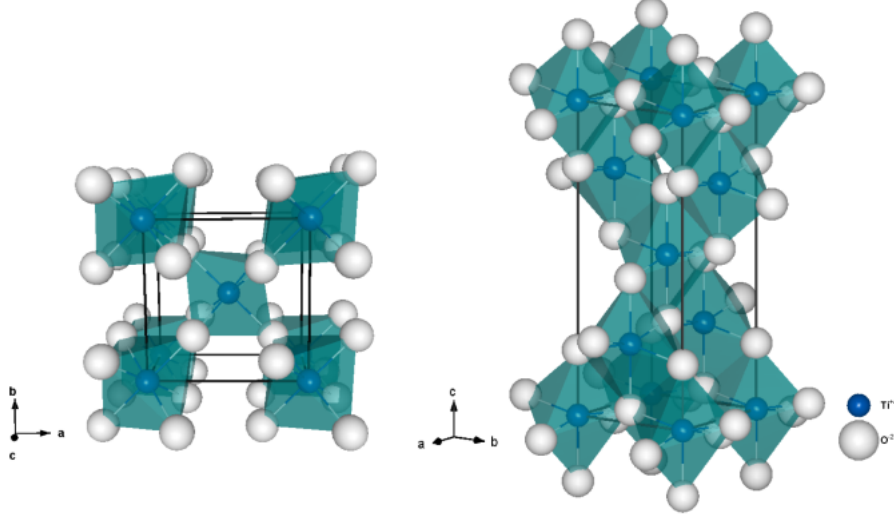


Figure 2.1: Rutile and anatase crystal structures

2.2 Classification of defects

Any form of deviation from the perfect crystal lattice can be termed a defect. Defects can be classified based on their dimensions as follows:

0-dimensional defects

0-dimensional defects (0-D) are point defects which are commonly observed in materials and exist in thermal equilibrium above 0 K [69]. The formation energy of these defects is lower than for extended defects. At any given temperature, a finite concentration of native point defects are always present due to the increase in entropy. In case of ionic solids, charge neutrality is maintained by the simultaneous creation of oppositely charged defect. The concentration of a separated defect pair $i+$ and $i-$ at a given temperature can be therefore represented by this relation

$$[c_{i+}][c_{i-}] = \exp\left(\frac{\Delta S_{\text{vib}}^{\circ}}{k}\right) \exp\left(-\frac{\Delta H^{\circ}}{kT}\right) \quad (2.1)$$

2.2 Classification of defects

Table 2.1: Properties of rutile and anatase TiO₂, data from ref [56, 67, 68].

	Rutile	Anatase
crystal structure	tetragonal	tetragonal
space group	$P4_2/mnm$	$I4_1/amd$
lattice constants (Å)	a=4.5936, c=2.9587	a=3.784, c=9.515
atoms/unit cell	6	12
phase transformation	no	rutile (400 °C-1100 °C)
density (g/cm ³)	4.25	3.89
melting point (°C)	1855	turns to rutile
permittivity (ϵ_r)	90 (c-axis) 170 (a-axis)	38 (c-axis) -
Ti-O bond length (Å)	1.949 (4) 1.980(2)	1.937(4) 1.965(2)
band gap (eV)	3.1	3.23
reflectance, % (at 400 °C)	47-50	88-90
UV light absorption at 360 nm(%)	90	67
coefficient of thermal expansion (10 ⁻⁶ / K)	7.14	10.2

where, $\Delta S_{\text{vib}}^\circ$ is the vibrational entropy and ΔH° is the enthalpy change per defect. The RHS of the above equation can also be simply represented in terms of standard free energy of formation (ΔG_f°) for a defect pair '*i+*' and '*i-*' or more simply in terms of the mass action constant of the corresponding defect reaction

$$[c_{i+}][c_{i-}] = \exp\left(\frac{-\Delta G_f^\circ}{kT}\right) = K(T) \quad (2.2)$$

Point defects are further classified in to native defects and impurity defects (dopants) which can be found either on the lattice (substitutional defects) or at the interstitial positions.

For consistency point defects are represented by Kroger-Vink notation [70] throughout this thesis. In TiO₂, the following point defects are to be considered

Intrinsic defects: oxygen vacancies - $V_{\text{O}}^{\bullet\bullet}$, titanium interstitials - $\text{Ti}_i^{\bullet\bullet\bullet\bullet}$, titanium vacancies - $V_{\text{Ti}}^{\prime\prime\prime}$ and oxygen interstitials - $O_i^{\prime\prime}$ (energetically very unfavorable [71])

Extrinsic defects: impurity defects such as trivalent ions on titanium site (acceptor impurity) - A'_{Ti} or a pentavalent ion on titanium site (donor impurity) - D_{Ti}^\bullet .

In case of ionic solids the overall charge has to be zero (electroneutrality), hence

2. THEORETICAL BACKGROUND

the total number of positively charged defects has to be balanced by the negatively charged defects.

Defect characterization Point defects can be studied by different experimental techniques such as dilatometry (expansion/contraction of the lattice), positron annihilation, transmission electron microscopy (TEM) or scanning tunneling microscopy (STM); all these methods are very tedious and time consuming, limited by investigated sample volume (often only few nanometers) and hence, often these techniques are not the first choice for characterization of point defects. Apart from these methods, point defects can be well investigated by measuring characteristic defect related properties such as electrical conductivity. Since conductivity is a function of defect concentration, understanding the variation in the conductivity by stoichiometry variation of the solid provides a great deal of information on the point defects. Therefore, measuring electrical conductivity as a function of oxygen partial pressure provides invaluable and sensitive information about the nature of the point defects (see section 2.3).

1-dimensional defects

1-D defects are can be viewed as one-dimensionally aggregated point defects (lines) which includes all kinds of dislocations such as edge type, screw type, mixed type and partial dislocations. The formation energy is higher for these defects than for point defects (but lower than for 2-D defects), owing to the higher number of broken bonds involved in their creation. Simultaneously the configurational entropy connected with their formation is much less than for point defects, (usually) forbidding their existence in thermodynamic equilibrium. (This is even more strictly true for 2-D defects). Dislocations can be viewed as an extra plane of atoms inserted or removed in the crystal which does not extend throughout the crystal (then it is an interface) but usually ends on an orthogonal plane known as a slip plane. The intersection (common) line between these two planes is known as the dislocation line or simply dislocation. Dislocations can be of edge type or screw type as shown in the Figure 2.2, however, in real crystals dislocations of pure edge character occur only rarely. In reality dislocation structures are more complicated, they are often mixed in nature

and also split in to partial dislocations to minimize their energy [72].

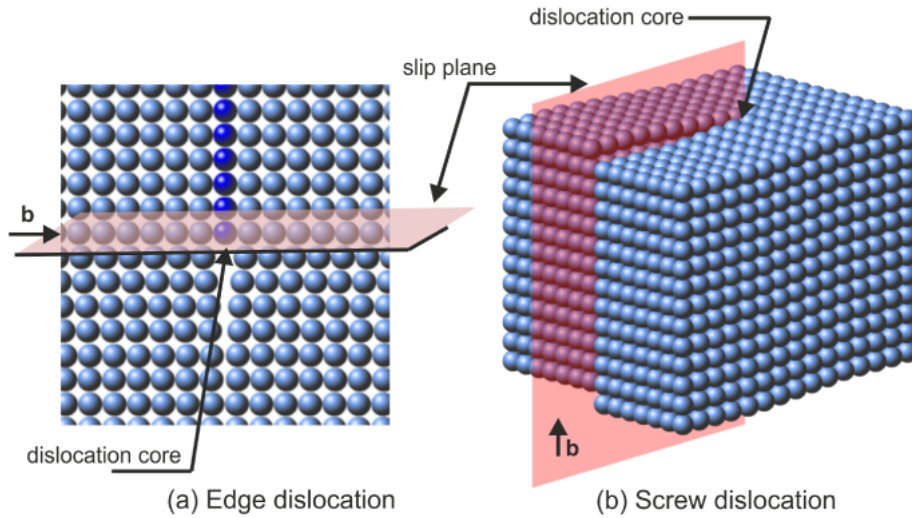


Figure 2.2: Schematic representation of a dislocation (a) edge type and (b) screw type. \mathbf{b} =Burgers vector

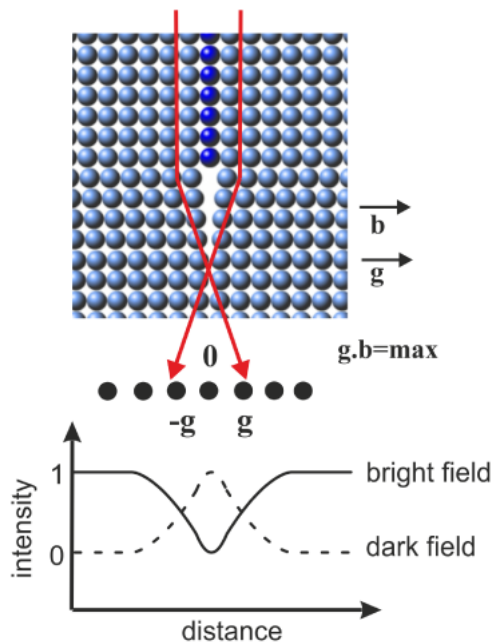


Figure 2.3: Schematic representation of conditions for viewing a dislocation in TEM

Defect characterization Dislocations can be best viewed and characterized by TEM, which operates on the principle of electron diffraction. The technique involves

2. THEORETICAL BACKGROUND

transmitting a monochromatic electron beam with energies typically between 100 kV to 1 MV through a thin sample and collecting the diffracted (elastically scattered) beam. With the primary and diffracted beam, it is possible to construct the local information of the lattice and the defects (imaging mode) and the diffraction spots obtained in the reciprocal lattice provides the orientation information. Details on dislocation orientation can be obtained by the 'two beam' condition, where only one reflection is excited at a time (collecting information from a specific diffraction vector - \mathbf{g}). It is also possible to determine the direction of dislocation or Burgers vector (\mathbf{b}) by this technique by viewing a dislocation in different diffraction vectors (\mathbf{g}) until a condition is found where the dislocation vanishes ($\mathbf{g} \bullet \mathbf{b} = 0$). The same approach can also be used for enhancing the contrast of dislocations by maximizing the scalar product ($\mathbf{g} \bullet \mathbf{b}$) as shown in the Figure 2.3.

2-dimensional defects

2-D defects are surface or area defects that extend in two dimensions. The most commonly known 2-D defects are grain boundaries, interfaces (heterostructures) and stacking faults. They cannot occur in thermodynamic equilibrium unless we refer to exotic cases. Nonetheless they are ubiquitous, as they are kinetically frozen not only at room temperature but also at elevated temperatures. Only if the temperatures are very high, they may anneal out. Grain boundaries are usually defined by the orientation relation of one grain with respect to the adjacent grain and the orientation of the GB plane relative to the grains. In real materials this can be any random orientation, however, for a systematic understanding of these defects it is helpful to have well defined grain boundaries known as Σ (Sigma) boundary, or boundaries with a small tilt, or twist boundaries. For characterizing these defects, especially the special boundaries and stacking faults, once again TEM is the best technique.

3-dimensional defects

3-D defects are volume defects which differ from the parent crystal (or matrix) in structure, composition or orientation. This can be for e.g. precipitates, second phase grains, pores or particles in the matrix. These defects are not common in

crystals, unless they are intentionally created by special treatments like precipitation processes. Typically, the formation energy for 3-D defects is higher as a larger number of bonds need to be broken for their formation.

2.3 Defect chemistry of TiO₂

Defect chemistry studies on oxides are commonly based on investigating the oxide nonstoichiometry as a function of oxygen activity or $p\text{O}_2$. Since hypo/hyper stoichiometry leads to conductivity or weight change as a result of point defect concentration variation, studying conductivity or mass variation as a function of $p\text{O}_2$ is the best method to study point defect chemistry, hence it has been most frequently used technique for several decades. In this work, the defect chemistry of TiO₂ was studied based on measuring the electrical conductivity as a function of oxygen partial pressure i.e. $\sigma \propto (p\text{O}_2)^m$, where m is termed as the $p\text{O}_2$ exponent. Since conductivity is a function of defect concentration and mobility (the latter can be assumed to be $p\text{O}_2$ independent), the majority defect species can be identified by their characteristic $p\text{O}_2$ exponent. This section is mainly focussed on deriving these relations for all possible point defects in TiO₂ based on their defect formation reactions and electroneutrality condition.

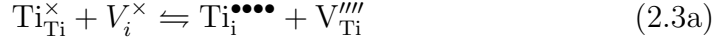
The defect chemistry of TiO₂ is more complicated compared with other wide band gap oxides such as SrTiO₃, ZrO₂, and CeO₂. The complexity mainly arises from having two types of mobile defects $\text{V}_{\text{O}}^{\bullet\bullet}$ and $\text{Ti}_i^{\bullet\bullet\bullet\bullet}$, which are comparable in concentration [26] over an extended $p\text{O}_2$ range. As mentioned earlier, the majority species can be identified by its characteristic $p\text{O}_2$ exponent m . Unfortunately in TiO₂ the m -values for $\text{V}_{\text{O}}^{\bullet\bullet}$ and $\text{Ti}_i^{\bullet\bullet\bullet\bullet}$ are very similar at reducing $p\text{O}_2$ ($m = -1/6$ for $\text{V}_{\text{O}}^{\bullet\bullet}$ and $m = -1/5$ for $\text{Ti}_i^{\bullet\bullet\bullet\bullet}$ explained later). This led to a controversy about the defect chemistry of TiO₂ in the past, some authors [27–31] claiming $\text{Ti}_i^{\bullet\bullet\bullet\bullet}$ as the majority defect while others [32–35] favor $\text{V}_{\text{O}}^{\bullet\bullet}$. A clear picture of the defect model is given here by combining the recent works of Lee et. al. [26] and Nowotny et. al. [36–38].

Possible intrinsic defect reactions in stoichiometric bulk TiO₂ are cation Frenkel

2. THEORETICAL BACKGROUND

as well as Schottky reaction, but of course also electron and hole defects by thermal excitation across the band gap as given by equations (2.3)-(2.5). Anion Frenkel defects are not considered in the defect chemistry of TiO₂ as they are unlikely to form in the rather close packed rutile structure as indicated by theoretical calculations [71].

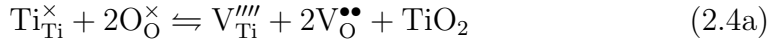
The cation Frenkel defect formation reaction (formation of cation interstitials (Ti_i^{••••}) and cation vacancies (V_{Ti}^{'''}) by transforming regular Ti⁴⁺ (Ti_{Ti}[×]) to a free interstitial site, V_i[×]) can be described as



with the mass action law (square brackets denote concentration)

$$K_F = [\text{Ti}_i^{\bullet\bullet\bullet\bullet}][V_{\text{Ti}}^{\prime\prime\prime}] = \exp\left(\frac{-\Delta G_F^{\circ}}{RT}\right) \quad (2.3b)$$

Similarly, the Schottky defect formation reaction (formation of Ti and oxygen vacancies by excorporating a regular Ti⁴⁺ and two regular O²⁻) is given by



$$K_S = [V_{\text{Ti}}^{\prime\prime\prime}][V_{\text{O}}^{\bullet\bullet}]^2 = \exp\left(\frac{-\Delta G_S^{\circ}}{RT}\right) \quad (2.4b)$$

The internal equilibrium for holes and electrons (exciting an electron from valance to conduction band) is given by



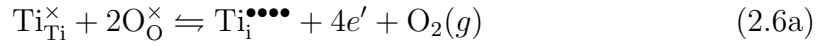
$$K_i = np \quad (2.5b)$$

where $[e'] \equiv n$ and $[h^{\bullet}] \equiv p$. Apart from Schottky and Frenkel defect disorders mentioned above, the point defect concentration in TiO₂ will also depend on the external redox equilibrium with oxygen ($p\text{O}_2$) and extrinsic compensation by impurities as shown below.

2.3.1 Undoped TiO₂

2.3.1.1 Extremely reducing regime

In extremely reducing atmosphere (pO_2 below 10^{-12} bar, $T \geq 1000$ °C), the concentration of titanium interstitials is found to be slightly higher than for oxygen vacancies [26] (by a factor 5 at 1000 °C). Titanium interstitials formation by the external equilibrium is given by



$$K_{Red}^{Ti} = [Ti_i^{\bullet\bullet\bullet\bullet}]n^4pO_2 \quad (2.6b)$$

The electroneutrality condition is satisfied by compensating electrons according to

$$n = 4[Ti_i^{\bullet\bullet\bullet\bullet}] \quad (2.6c)$$

Substituting the above condition in eq. 2.6b gives

$$n = (4K_{Red}^{Ti})^{1/5}(pO_2)^{-1/5} \quad (2.6d)$$

Equation (2.6d) shows that when the majority ionic defects ($Ti_i^{\bullet\bullet\bullet\bullet}$) are electrically compensated by electrons, $n \propto (pO_2)^m$ with $m = -1/5$. At high concentration of electrons and $Ti_i^{\bullet\bullet\bullet\bullet}$, one can expect trapping of electrons by the positively charged $Ti_i^{\bullet\bullet\bullet\bullet}$ giving rise to $Ti_i^{\bullet\bullet\bullet}$. In such a case, the defect reaction and mass action laws are given by



$$K_{trap} = \frac{[Ti_i^{\bullet\bullet\bullet}]}{[Ti_i^{\bullet\bullet\bullet\bullet}]n} \quad (2.7b)$$

and the electroneutrality is defined by

$$n = 3[Ti_i^{\bullet\bullet\bullet}] \quad (2.7c)$$

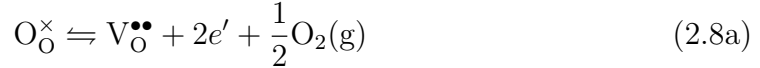
2. THEORETICAL BACKGROUND

Considering the above neutrality condition and substituting eq. (2.6b) in to eq. (2.7b) gives

$$n = (3K_{trap}K_{red}^{Ti})^{1/4} (pO_2)^{-1/4} \quad (2.7d)$$

2.3.1.2 Strongly reducing regime

In the strongly reducing regime (pO_2 below 10^{-5} bar, $T \sim 1000$ °C), oxygen vacancy concentration slightly increases over titanium interstitials to give rise to the following pO_2 exponent. Oxygen vacancy creation is given by



$$K_{Red}^O = [V_O^{\bullet\bullet}]n^2(pO_2)^{1/2} \quad (2.8b)$$

By substituting the electroneutrality condition

$$n = 2[V_O^{\bullet\bullet}] \quad (2.8c)$$

eq. (2.8b) can be written as

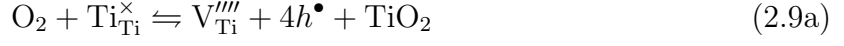
$$n = (2K_{Red}^O)^{1/3} (pO_2)^{-1/6} \quad (2.8d)$$

From eq. (2.8d), it is obvious that a plot of $\log \sigma$ vs $\log pO_2$ results in a slope of -1/6, when electrons are compensating $V_O^{\bullet\bullet}$.

2.3.1.3 Transition regime from slightly reducing to oxidizing conditions

In the slightly reducing to oxidizing regime (pO_2 below 1 bar, $T \sim 450$ to 1000 °C), i.e., close to the stoichiometric composition, ionic defects ($Ti_i^{\bullet\bullet\bullet\bullet}$ and $V_O^{\bullet\bullet}$) are either compensated intrinsically by $V_{Ti}^{\bullet\bullet\bullet\bullet}$ or extrinsically by background acceptor impurities such as A'_{Ti} . It is not possible to clearly distinguish these two compensations by conductivity measurements as both lead to the same pO_2 exponent. These two compensations are described below

case 1: Intrinsic compensation For intrinsic compensation, V_{Ti}'''' formation reaction is described by



$$K_{\text{Ox}} = [V_{\text{Ti}}'''] p^4 (p\text{O}_2)^{-1} \quad (2.9b)$$

electroneutrality is maintained by compensating $V_{\text{O}}^{\bullet\bullet}$

$$2[V_{\text{O}}^{\bullet\bullet}] = 4[V_{\text{Ti}}'''] \quad (2.9c)$$

$V_{\text{O}}^{\bullet\bullet}$ defects are in turn in equilibrium with electrons according to eq. (2.8b). Substituting this condition into eq. (2.9b) results in

$$K_{\text{Ox}} = \left[\frac{K_{\text{Red}}^{\text{O}}}{n^2 (p\text{O}_2)^{1/2}} \right] p^4 (p\text{O}_2)^{-1} \quad (2.9d)$$

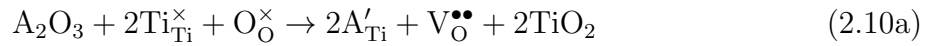
Based on the equilibrium eq. (2.9d) and the internal equilibrium condition (eq. (2.5)), this can be optionally written for holes (oxidizing condition) or electrons (slightly reducing condition). For electrons

$$n = \left[\frac{K_i^4 K_{\text{Red}}^{\text{O}}}{K_{\text{Ox}}} \right]^{1/6} (p\text{O}_2)^{-1/4} \quad (2.9e)$$

similarly for holes, it is given by

$$p = \left[\frac{K_i^2 K_{\text{Ox}}}{K_{\text{Red}}^{\text{O}}} \right]^{1/6} (p\text{O}_2)^{1/4} \quad (2.9f)$$

case 2: Extrinsic compensation Acceptor type impurities (A'_{Ti}) in TiO₂ fix the concentration of $V_{\text{O}}^{\bullet\bullet}$ extrinsically by the following reaction



The electroneutrality is defined is by

$$[A'_{\text{Ti}}] = 2[V_{\text{O}}^{\bullet\bullet}] \quad (2.10b)$$

2. THEORETICAL BACKGROUND

In reducing conditions, the $V_{\text{O}}^{\bullet\bullet}$ will be in equilibrium with electrons according to eq. (2.8b) giving rise to

$$K_{acc} = 4K_{Red}^O n^{-6} (pO_2)^{-3/2} \quad (2.10c)$$

$$n = \left[\frac{4(K_{Red}^O)^3}{K_{acc}} \right]^{1/6} (pO_2)^{-1/4} \quad (2.10d)$$

Eq. (2.10c) can be written for holes in oxidizing conditions according to the internal equilibrium Eq. (2.5)

$$p = K_i \left[\frac{4(K_{Red}^O)^3}{K_{acc}} \right]^{-1/6} (pO_2)^{1/4} \quad (2.10e)$$

From equations (2.9) and (2.10) it is evident that both intrinsic and extrinsic compensation lead to the same pO_2 exponent. In addition, considering the majority ionic defects to be $Ti_i^{\bullet\bullet\bullet\bullet}$ instead of $V_{\text{O}}^{\bullet\bullet}$ will also result in the same pO_2 exponent. This is the main reason for controversy in the literature [27–35]. Based on point defect investigations by Lee et al. [26] and Nowotny et al. [36–38], it is rather obvious that majority defects are $V_{\text{O}}^{\bullet\bullet}$ at high pO_2 and compensation occurs by $V_{\text{Ti}}^{\prime\prime\prime}$ and A'_{Ti} at oxidizing and slightly reducing conditions, respectively. Since these two type of ionic defects are comparable in concentration, a more general representation of the electroneutrality condition close to oxide stoichiometry has to be used

$$[A'_{\text{Ti}}] + 4[V_{\text{Ti}}^{\prime\prime\prime}] = 4[Ti_i^{\bullet\bullet\bullet\bullet}] + 2[V_{\text{O}}^{\bullet\bullet}] \quad (2.11)$$

By solving equations (2.6) to (2.10), the defect structure of TiO_2 can be obtained as shown in Figure 2.4. As the temperature decreases the lines in the plot will not only be shifted toward lower conductivity values but also towards lower pO_2 [38].

2.3.2 Acceptor doped TiO_2

For nominally undoped TiO_2 which contains acceptor type impurities, the same defect model described above is valid excluding the equations (2.9) which are for intrinsic compensation. It is worth mentioning that acceptor doping in TiO_2 always leads to an increase in ionic and electronic hole concentration [2, 3, 73], hence it is

2.3 Defect chemistry of TiO₂

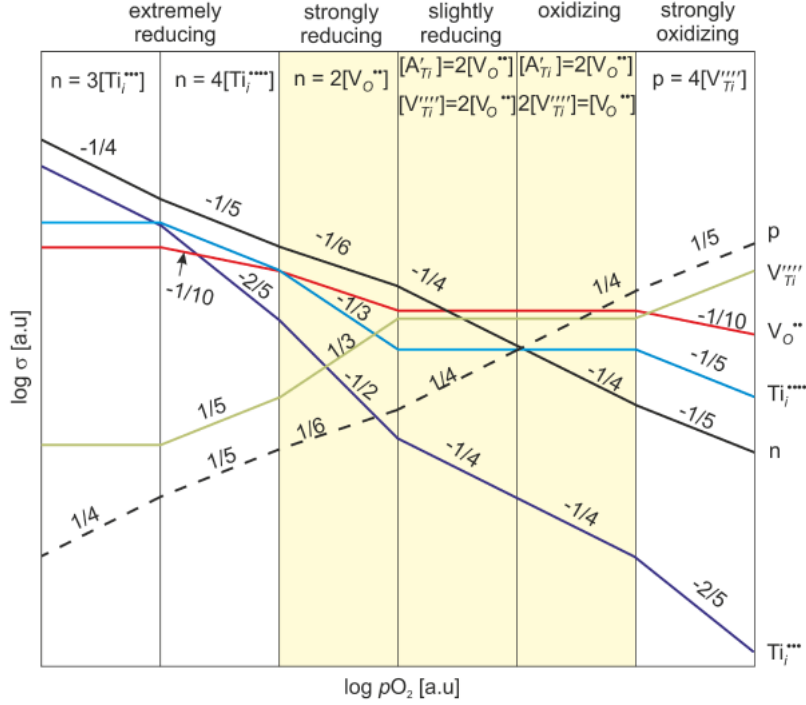


Figure 2.4: Kroeger-Vink diagram of acceptor doped TiO₂.

not possible to have a pO_2 independent ionic conductivity* (horizontal line in $\log \sigma$ vs $\log pO_2$).

2.3.3 Donor doped TiO₂

Donor dopants (D_{Ti}^{\bullet}) in TiO₂ are introduced by adding higher valence impurities than Ti⁴⁺ (e.g., Nb⁵⁺). Donors atoms substitute Ti ions to give additional electrons to the system according to following reaction



However at very low pO_2 , the concentration of $V_O^{\bullet\bullet}$ and $Ti_i^{\bullet\bullet\bullet}$ outnumber the D_{Ti}^{\bullet} concentration due to the reduction reaction (equations (2.6) and (2.8)). This

*depends on several factors such as concentration of $V_O^{\bullet\bullet}$ and h^{\bullet} and their migration enthalpies, in rutile high concentration of holes and low migration enthalpy leads to an increased hole conductivity on acceptor doping

2. THEORETICAL BACKGROUND

does not change the pO_2 exponent (m) from acceptor or nominally undoped TiO_2 in extremely and strongly reducing regimes as shown in the Kroeger-Vink diagram 2.5 (equations (2.6) to (2.8) are also valid for donor doped TiO_2).

2.3.3.1 Reducing regime - I

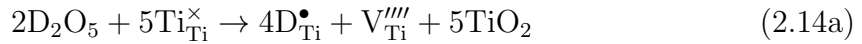
In the reducing regime, i.e. $[D_{Ti}^\bullet] > [V_O^{\bullet\bullet}]$, the fixed donor concentration governs the electronic charge compensation by

$$n = [D_{Ti}^\bullet] \quad (2.13)$$

Since equation (2.13) is pO_2 independent and the donor dopant concentration is fixed, the electron concentration will also be independent of pO_2 as shown in Figure 2.5.

2.3.3.2 Reducing regime - II

In this regime, donor incorporation into the TiO_2 lattice is described by the following equation



the ionic charge compensation for D_{Ti}^\bullet is given by

$$4[V_{Ti}^{\prime\prime\prime}] = [D_{Ti}^\bullet] \quad (2.14b)$$

$[V_{Ti}^{\prime\prime\prime}]$ from the electroneutrality condition enters into eq. (2.9b), and gives rise to

$$n = \left[\frac{[D_{Ti}^\bullet] K_i}{4K_{Ox}} \right]^{1/4} (pO_2)^{-1/4} \quad (2.14c)$$

According to equation (2.14a), the concentration of electrons in this regime is a function of $[D_{Ti}^\bullet]$ and pO_2 , leading to $m = -1/4$ as shown in Figure 2.5.

Defect concentration as a function of pO_2 can be calculated from the defect equilibrium constants given in Table 2.2, refer [38] for further details on the experimental methods used to determine these values. A comment on data in Table 2.2 is that

2.3 Defect chemistry of TiO₂

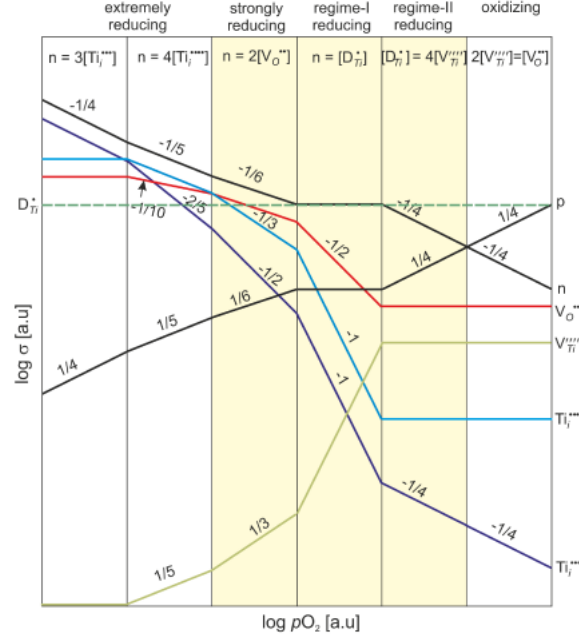


Figure 2.5: Kroeger-Vink diagram for donor doped TiO₂.

care has to be taken when considering the values for $Ti_i^{••••}$ as Nowotny's defect model underestimates the $Ti_i^{••••}$ defect formation at high pO_2 (see ref. [26] by Lee et. al. showing a considerable concentration of $V_O^{••}$ and $Ti_i^{••••}$ defects at high pO_2). Table 2.3 summarizes literature migration enthalpies for different defects

equilibrium	ref. [38]	ref. [74]	ref. [75]	ref. [76]
constant	ΔH° [kJ/mol]	ΔS° [J/mol/K]	ΔH° [eV]	ΔH° [eV]
K_{Red}^O Eq.(2.8b)	493	106		
K_{Red}^{Ti} Eq.(2.6b)	1025	238	10.67	9.6
K_{trap} Eq.(2.7b)	146	48	1.43	
K_{Ox} Eq.(2.9b)	354	-202		
K_i Eq.(2.5)	222	44	3.7	3.05

Table 2.2: Equilibrium constants of defect reactions for undoped TiO₂ according to ref [38]

2. THEORETICAL BACKGROUND

Defect	Migration enthalpy (eV)	reference
$V_{\text{O}}^{\bullet\bullet}$	0.8	[26]
$Ti_i^{\bullet\bullet\bullet\bullet}$	0.7	[77]
$V_{\text{Ti}}^{\prime\prime\prime\prime}$	1.42	[78]
h^{\bullet}	0.4-0.85	[3, 79]
e^{\prime}	0.1	[79]

Table 2.3: Migration enthalpies for point defects in TiO_2

2.4 Impedance spectroscopy

Impedance spectroscopy (or electrochemical impedance spectroscopy, EIS) combined with transmission electron microscopy provides an in-depth understanding of electrical properties of ionic solids. Since this thesis mainly focusses on the influence of extended defects on the electrical properties, this section deals with interpretation of impedance spectra to understand different transport properties that correspond to features in the microstructure i.e., bulk, GB or dislocations.

In EIS, an alternating voltage (or current) is applied across the sample and the resulting current (or voltage) is measured as a function of frequency(ω). The impedance of a material as a function of frequency can be expressed as a complex function, with j =imaginary unit, as

$$Z(j\omega) = Z' + jZ'' \quad (2.15)$$

The complex plane plot of Z' on x-axis and Z'' on y-axis results in continuous curves from which basic elements (R = resistor, C = capacitor, L = inductor) can be extracted by fitting the spectra with a combination of equivalent circuit elements (phenomenological circuits) that should be chosen such that they are properly represent the physical processes of the system. The complex plane plots are commonly known as Nyquist plots. Figure 2.6 shows a Nyquist plot for a polycrystalline material with reversible electrodes. At low frequencies ($\omega \rightarrow 0$) the impedance of the material corresponds to the DC resistance (R), which is also the total resistance ($R_b + R_{GB}$) of the sample. A high frequencies ($\omega > 10^6$ Hz) the impedance approaches zero due to short circuiting of the resistors by the highly permeable capacitors. The frequency at the peak maximum (ω_{max}) of a semicircle defines the time constant of the process,

given by

$$\tau_{\max} = (RC)_{\max} = \omega_{\max}^{-1} \quad (2.16)$$

Different physical serial processes (due to bulk, GB, electrodes etc...) with sufficiently different relaxation times (e.g. $\tau_{\text{bulk}} < \tau_{\text{GB}} < \tau_{\text{elec}}$) lead to distinguishable semicircles as shown in Figure 2.6. It can be realized that the semicircles are not perfect but depressed in polycrystalline materials, and the depression is higher for GB's compared to the bulk. This nonideality could arise from inhomogeneities in the electrode or inhomogeneities within the sample (especially when samples are not dense). Fitting the spectra for such a nonideal process is not possible by assuming an ideal plate capacitor 'C' in the RC circuit, but can be best described by assuming a constant phase element (CPE) represented as 'Q' [80]. For polycrystalline materials or bicrystals with GB's, the capacitance can be estimated from the CPE according to the following expression [81]

$$C = (R^{1-\psi}Q)^{\frac{1}{\psi}} \quad (2.17)$$

Where, ψ known as the ideality factor describes the depression. Therefore, when $\psi = 1$, CPE (Q) is replaced by an ideal capacitor C.

Since the safe interpretation of impedance data requires an equivalent circuit model, reliable data can only be extracted by assuming a model which correctly represents the physical processes in the real system. Two different models viz. layer and effective medium models are in use for this purpose [82–84]. In this work, single crystals, bicrystals and polycrystals layer models best describes the physical processes of the system.

At this point, it is worth distinguishing the structural boundary from the electrical boundary. Crystallographic mismatch zones are commonly known as structural boundaries which typically extend only up to 1 or 2 nm in width for grain boundaries (also for dislocations). Electrical boundaries are defined from the electrochemical point of view (zone with low conductivity) which usually extend over several nanometers depending on the charge screening strength (Debye length, λ) of the material (see section 2.5). Figure 2.7 schematically represents the situation for an ionic solid with oxygen vacancy depletion, the electrical boundary is described by the $V_{\text{O}}^{\bullet\bullet}$ profile and the width of the electrical boundary is defined by the ex-

2. THEORETICAL BACKGROUND

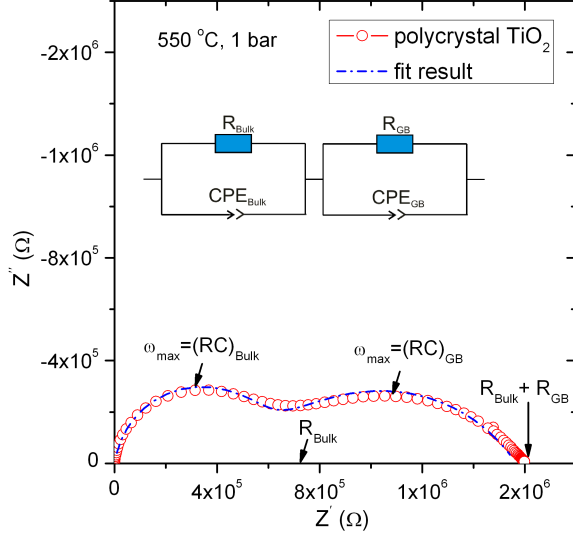


Figure 2.6: Nyquist plot for a polycrystalline ionic solid with bulk and grain boundary contribution, inset shows the equivalent circuit that represents the observed processes.

tent of charge depletion. Therefore in impedance spectroscopy, grain boundaries in polycrystalline materials are wider (depending on the space charge width) than the atomic structures observed in microscopy.

Layer models

Layer models are broadly classified in to the following

Series layer model The series layer model was first described by Maxwell [84] to describe electrical properties for two-phase microstructures when measured across the phases as shown in Figure 2.8. The same model can be used for describing electrical properties of TiO_2 bicrystals. The second phase in Maxwell's model can be replaced with the electrical boundary zone in bicrystals (Figure 2.7). The impedance of two phases can be well resolved only when the phases have sufficiently different relaxation times (τ_D). The bulk and GB capacitances (C_{bulk} , C_{GB}) can be written

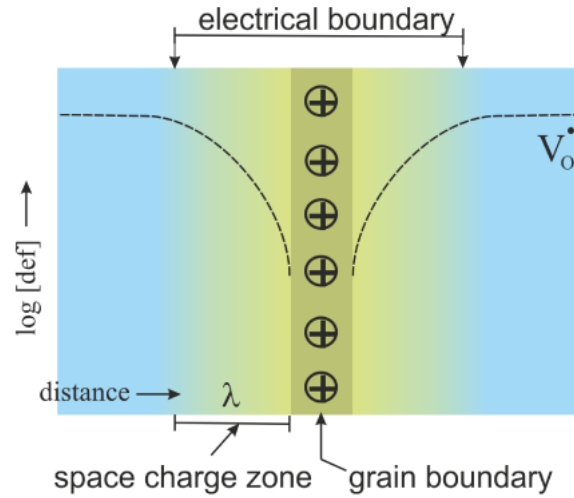


Figure 2.7: Schematic representation of structural and electrical boundaries for ionic solids.

as

$$\frac{C_{GB}}{C_{bulk}} = \frac{d_g \varepsilon_{GB}}{\delta_{gb} \varepsilon_{bulk}} \quad (2.18)$$

where d_g is the grain size and δ_{GB} is the structural grain boundary thickness. Considering no change in the bulk and GB capacitance, we see the GB permittivity is at least 2 to 3 orders higher in magnitude compared to the bulk capacitance, and hence it is very likely to resolve these two contributions in EIS.

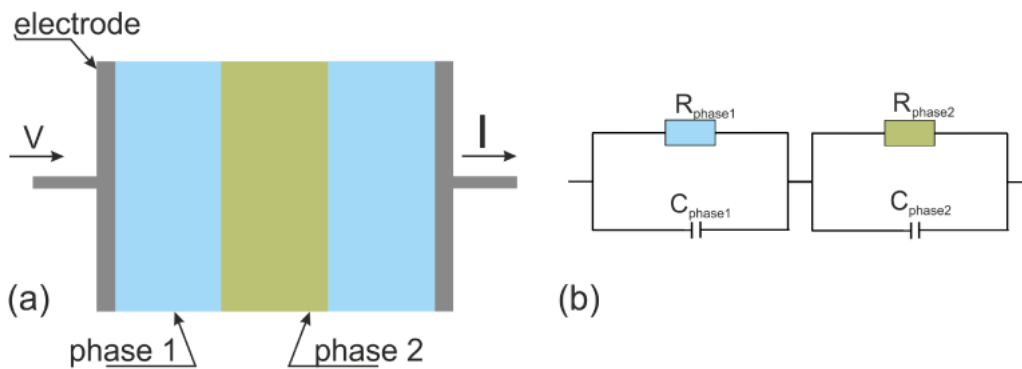


Figure 2.8: Schematic representation of (a) two phase series layer model (equivalent to bulk and grain boundary in bicrystals in case of reversible electrodes) and (b) equivalent electrical circuit.

2. THEORETICAL BACKGROUND

Parallel layer model In the parallel layer model, the measuring electrodes are perpendicular to the phases, which allows one to measure conductivity along the phases as shown in Figure 2.9. This model describes the situation in TiO_2 single crystals with dislocations extending throughout the crystal i.e., parallel to the electrical measurement axis. The electrical equivalent circuit for this can be represented by two parallel RC circuit elements, which transforms to a single parallel RC circuit (single semicircle in impedance) as shown in Figure 2.9. If one phase (e.g. dislocations) is highly conductive compared to the other, then the observed impedance spectrum may be dominated by the highly conductive phase.

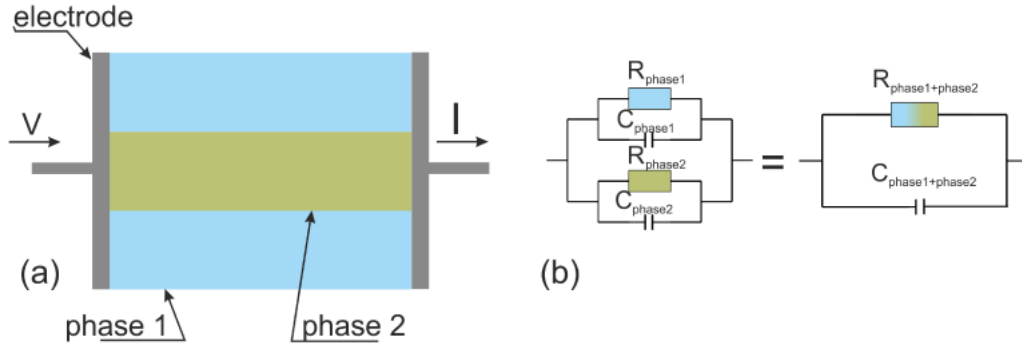


Figure 2.9: Schematic representation of (a) two phase parallel layer model (equivalent to bulk and parallel dislocations in single crystals) and (b) equivalent electrical circuit.

Brick layer model The brick layer model [83, 85, 86] is a well known and commonly used layer model for polycrystalline materials, where the grains are represented as an array of cubes separated by slab shaped grain boundaries as shown in Figure 2.10. Based on the specific conductivity of grain (σ_{bulk}) and σ_{GB} the current path can take one of the following:

- (1) when $\sigma_{\text{bulk}} \gg \sigma_{\text{GB}}$, current path will be through grains and across grain boundaries
- (2) when $\sigma_{\text{bulk}} \ll \sigma_{\text{GB}}$, current path will be preferably along grain boundaries.

In path (1), neglecting the resistive GB conductivity parallel to the grains results in the simple series layer model which is commonly used for extracting the bulk and

GB conductivities in polycrystalline materials (according to the equations shown in section 3.4.2).

In some ionic solids more than one type of mobile charged defects are present and

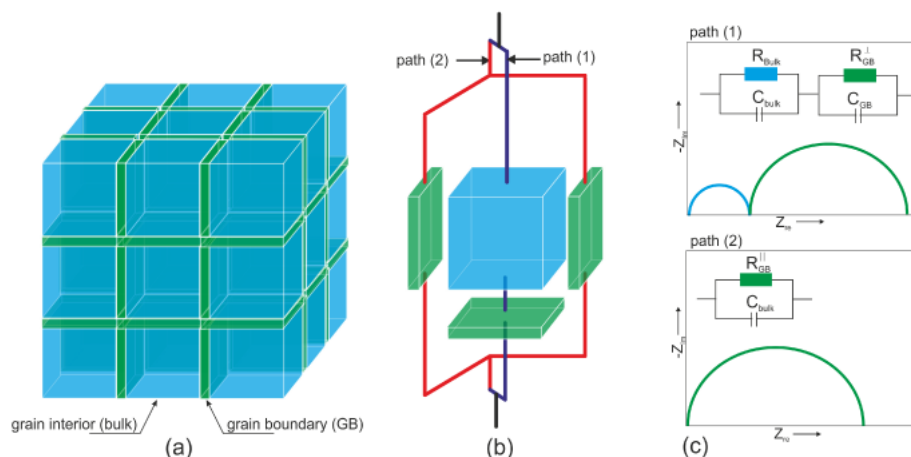


Figure 2.10: Schematic representation of brick layer model with (a) cube shaped grains separated by grain boundaries, (b) possible parallel electrical path ways and (c) respective impedance spectra and equivalent circuits, image developed based on ref. [87].

hence the selection of path (1) or (2) also depends on the signs of the core charge the mobile defect. For example, in SrTiO_3 at high $p\text{O}_2$ the majority charge carriers oxygen vacancies and holes take path (1) and at low $p\text{O}_2$ majority charge carriers - electrons, take path (2) [88]. A schematic representation of impedance spectra depending on the GB core charge and sign of the majority charge carrier defect is shown in the Figure 2.11. Hence the knowledge of defect chemistry combined with EIS provides qualitative and semi-quantitative information about the boundary core charge, which would be a very tedious and difficult measurement to determine by transmission electron microscopy.

2.5 Space charge effects

As described in the classification of defects and in the defect chemistry section, ionic solids keep overall charge neutral by the electroneutrality conditions. However, locally there can be regions with excess charges due to charged extended defects such

2. THEORETICAL BACKGROUND

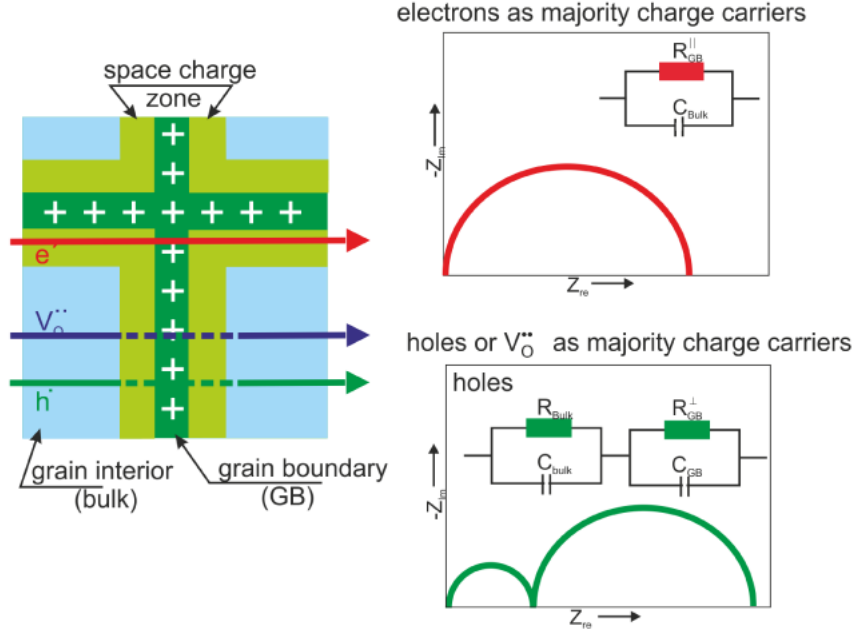


Figure 2.11: Schematic representation space charge layer and impedance spectra as with respect to the defect type, according to ref. [13, 87]

as dislocations, stacking faults, and grain boundaries. Such excess charges are often observed in the majority of wide band gap oxides such as ZrO_2 [89], CeO_2 [13], SrTiO_3 [90, 91], TiO_2 [4, 92, 93], and also in halides - NaCl [18, 94], AgCl [19, 95], AgBr , CsCl , CaF_2 [19]. To keep overall charge neutral, the defects adjacent to these excess charges get redistributed either by depletion (Mott-Schottky profile) or by accumulation (Gouy-Chapman profile) depending on the defect charge with respect to the extended defect (core) charge. This local charge redistribution is known as the space charge zone and the overall effect is known as the space charge effect. It is assumed that the crystal structure and permittivity are unchanged in the space charge zone.

The defect concentration profile ($c_i(x)$) in the space charge zone due to the influence of the space charge potential is given by [5, 96]

$$\frac{c_i(x)}{c_{i,\infty}} = \exp\left(-\frac{z_i e \Delta\phi(x)}{kT}\right) \quad (2.19)$$

where, $c_{i,\infty}$ is the concentration of defect i in the bulk, and e, k, T represents the usual quantities and $\Delta\phi(x)$ is the space charge potential at a distance x . The overall potential is described by $\Delta\phi^\circ = \phi(0) - \phi(\infty)$, where $\phi(0)$ is the potential at the interface and $\phi(\infty)$ is the bulk potential.

Solving Poisson's equation and combination with equation (2.19) yields the Poisson-Boltzmann differential equation. For one dimension (x) it is given as

$$\frac{d^2\phi_x}{dx^2} = \frac{-e}{\varepsilon_o\varepsilon_r} \sum_i z_i c_{i,\infty} \exp\left(\frac{-z_i e}{kT} \Delta\phi(x)\right) \quad (2.20)$$

where ε_o = permittivity of vacuum, ε_r = relative permittivity of the material. The differential equation (2.20) can be solved with appropriate boundary conditions such as defining the reference potential (usually set as zero in the bulk) and variation of the potential in the bulk considered to be zero (i.e. $\frac{d\phi}{dx} = 0$ as $x \rightarrow \infty$). For brevity only the solutions for the concentration profile are given here for two main scenarios viz. Gouy-Chapmann and Mott-Schottky case, a detailed treatment is given elsewhere [69].

Gouy-Chapman case All majority defects are mobile and are redistributed in the space charge zone. Since the majority charge carriers are accumulated in the space charge region in this case, it is also known as space charge accumulation model. The concentration profiles for a defect i is given by

$$\frac{c_i(x)}{c_{i,\infty}} = \left(\frac{1 + \Theta \exp\left(\frac{-x}{\lambda}\right)}{1 - \Theta \exp\left(\frac{-x}{\lambda}\right)} \right)^{(2z_i)} \quad (2.21)$$

where Θ is the profile parameter, $\Theta = \tanh\left(\frac{z_i e \Delta\phi^\circ}{4kT}\right)$ and λ is the Debye length, which describes the width of charge screening (extension of defect redistribution)

$$\lambda = \sqrt{\frac{\varepsilon_o\varepsilon_r kT}{2z_i^2 c_{i,\infty} e^2}} \quad (2.22)$$

2. THEORETICAL BACKGROUND

An increase in relative permittivity of the material or a decrease in the impurity concentration will lead to a bigger Debye length, λ . The core charge density (total excess charge in the extended defect) can be calculated from [97]

$$Q_{\text{core}} = \sqrt{8kTc_{i,\infty}\varepsilon_o\varepsilon_r} \sinh\left(\frac{z_i e \Delta\phi^o}{2kT}\right) \quad (2.23)$$

Mott-Schottky case When a majority ionic defect (especially dopants) becomes immobile then the Mott-Schottky situation is obtained. This forces the opposite majority carrier to deplete to compensate the core charge. The concentration profiles in such case is given by

$$\frac{c_i(x)}{c_{i,\infty}} = \exp\left[-\frac{z_i}{z_{\text{imm}}}\left(\frac{x - \lambda^*}{2\lambda}\right)^2\right] \quad (2.24)$$

where z_{imm} is the immobile majority charge defect and λ^* is the extension of the depletion zone due to the immobile charge carrier

$$\lambda^* = \sqrt{\frac{2\varepsilon_o\varepsilon_r\Delta\phi^o}{z_i e c_{i,\infty}}} = \lambda \sqrt{\frac{4z_i e}{kT}\Delta\phi^o} \quad (2.25)$$

The core charge density in this situation is given by

$$Q_{\text{core}} = \sqrt{8\varepsilon_o\varepsilon_r e c_{i,\infty}\Delta\phi^o} = 2\lambda^* z_i e c_{i,\infty} \quad (2.26)$$

Space charge potential from impedance measurements under the Mott-Schottky situation the space charge potential can be extracted from the conductivities of the bulk and grain boundaries from the impedance spectra [89]

$$\frac{\sigma_{\text{bulk}}}{\sigma_{\text{GB}}^{\text{spec}}} = \frac{C_{\text{GB}}R_{\text{GB}}}{C_{\text{bulk}}R_{\text{bulk}}} = \frac{\exp\left(\frac{ze\Delta\phi^o}{RT}\right)}{\frac{(2ze\Delta\phi^o)}{RT}} \quad (2.27)$$

where $\sigma_{\text{GB}}^{\text{spec}}$, is the specific GB conductivity calculated according to Equation (3.5)

Combined case Another possible situation is a combination of Gouy-Chapman and Mott-Schottky cases, where one majority charge carrier is immobile and the

other majority charge carrier is depleted as in the Mott-Schottky situation along with accumulation of minority charge carriers in the bulk that cross over the majority carriers in the space charge region, as shown in Figure 2.12.

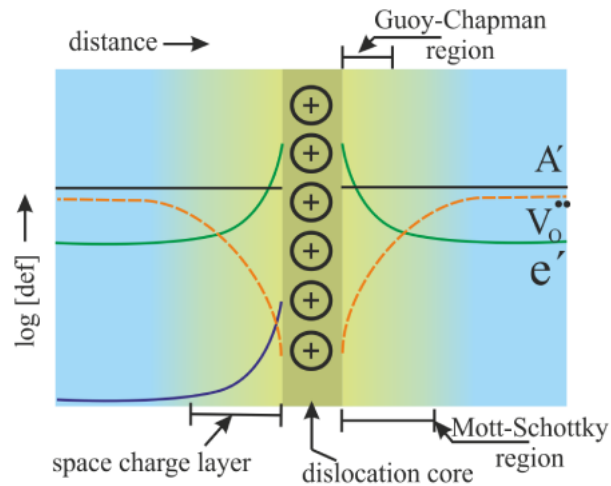


Figure 2.12: Schematic representation of space charge model for a combined case.

2. THEORETICAL BACKGROUND

3

Materials and Methods

3.1 TiO₂ single crystals

For studying the influence of 1-D defects, TiO₂ single crystal pieces (10x10x0.5 mm³) in [001] and [110] orientations (with large faces being (001) and (110)) were prepared from a large crystal boule (Frank & Schulte GmbH) grown in [001] direction by the Verneuil-flame fusion method. All pieces were prepared in-house (crystal preparation group, MPI-FKF) with the help of Laue diffraction and a precision saw with goniometer. After cutting one of the large surface was polished to a mirror finish. The chemical composition of the crystal was analyzed by inductively coupled plasma optical emission spectroscopy (ICP-OES, performed at MPI-IS) and indicated in the table 3.1. For preparing bicrystals different samples were used (see section 3.6.1).

3.2 Polycrystalline TiO₂ powder synthesis

Polycrystalline TiO₂ ceramics in this study were prepared from TiO₂ powders synthesized via sol-gel process. For preparation of approx. 2 g of TiO₂, 7.5 mL of titanium (IV) isopropoxide (Aldrich, 97 %) precursor was added to 50 mL 2-propanol (Merck) solvent to make a 0.5 M solution. The solution was stirred continuously in ambient room temperature under air for 30 min until a clear homogeneous solution was obtained. The obtained precursor solution was added dropwise into 20 mL

3. MATERIALS AND METHODS

acetic acid (Roth, 100 % p.a) and 2-propanol mixture (1:1 by volume) and stirred for 2 h to completely hydrolyze the precursor. Finally, 10 mL of distilled and deionized water was added dropwise in to the sol to initiate gelification process. A thick white gel is obtained after aging for 30 min. The solvents in the gel were evaporated by drying in an air circulation oven at 100 °C for 12 h. The dried particles (yellow to whitish color) were grounded to fine powder and calcined at 450 °C for 5 h to expel all volatile organic materials, resulting in a clear white powder. The TiO₂ powder prepared by this method was phase pure anatase (Figure 3.1) with a crystallite size of approx. 20 nm as determined from X-ray diffraction. The impurity content of the particles obtained by this process is less than 65 ppm (see table 3.1) as determined by ICP-OES analysis. The phase transformation from anatase to rutile occurred while sintering at high temperatures. No significant changes were observed in terms of electrical properties, whether the transformation occurred during sintering or before sintering.

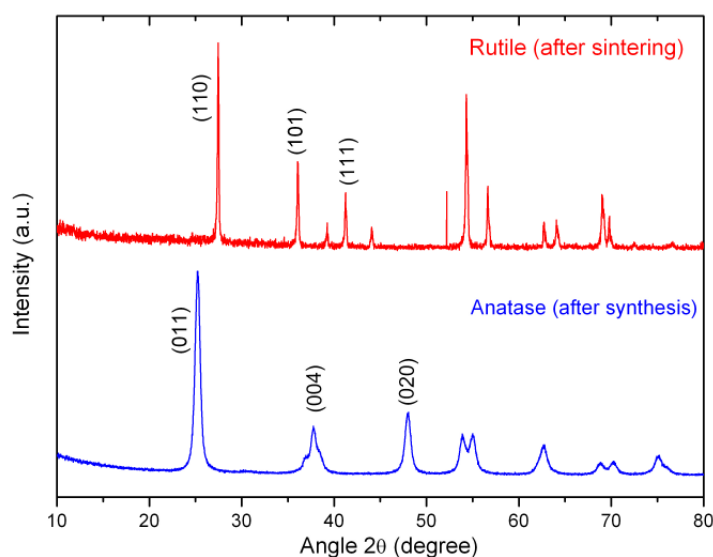


Figure 3.1: XRD pattern for TiO₂ powders after sol-gel synthesis (anatase phase) and after sintering (rutile phase).

3.3 Sintering procedures

Element	Single crystal TiO ₂ mol. fraction (ppm)	Polycrystalline TiO ₂ mol. fraction (ppm)
Al	ca 74	<15
Ca	<20	<40
Cr	<30	<8
Cu	<25	<6
Fe	<14	<7
Mg	<33	-
Mn	<7	<3
Na	<70	-
Ni	<14	<7
V	<16	<8
Zn		<2
Zr		<2

Table 3.1: Chemical analysis (ICP-OES) of the materials used in this work.

3.2.1 Doping and decoration

Dopants were incorporated in to TiO₂ powders by either homogeneous doping or GB decoration. In case of homogeneous doping, the dopants were introduced in to the parent lattice during the sol-gel process - just before hydrolyzing the precursor. The main dopant used in this work is, Y³⁺ in form of yttrium nitrate (Aldrich, Y(NO₃)₃.6H₂O, 99.9 %) as an acceptor. In case of decoration, the dopants were coated on TiO₂ particles by suspending the latter in a dopant solution (solvent being water for yttrium nitrate). The suspension was later dried by a rotating vacuum dryer (Rotovap), followed by calcination at 450 °C for 5 h. The key difference in this process from homogeneous doping was that dopants are expected to remain very close to the grain boundaries due to sluggish cation diffusion compared to very fast sintering processes initiated by spark plasma sintering (less than 5 min at 925 °C).

3.3 Sintering procedures

Polycrystalline TiO₂ samples in this work were obtained by sintering of titania powders obtained via sol-gel process. Conventional sintering was applied for studying

3. MATERIALS AND METHODS

the bulk and GB electrical properties without the influence of dislocations. In order to study the effect of dislocations, spark plasma sintering process was used to prepare dense ceramics with dislocations.

3.3.1 Conventional sintering

Conventional sintering (CS) is an inexpensive sintering process which is widely practiced for densification of ceramics. Before sintering, the powders were placed in a rubber mold of required dimensions (0.5 cm diameter and ~ 1 mm thickness in this study) and sealed tightly in polypropylene bags. These bags were isostatically pressed at 900 MPa for 5 min at room temperature. The samples were intact without any cracks indicating homogeneous stress throughout the sample. The cold compressed samples were gently placed in Al_2O_3 boats and covered all sides with the same TiO_2 powders in order to avoid contamination from the crucibles, and sintered at 1300 °C for 5 h in air, with a heating and cooling rate of ± 5 °C/min. The samples obtained by this process were not of high density compared to SPS samples; the density of these samples as calculated from their geometry is approx. 70 %. The microstructures of different samples prepared by the CS method are shown in Figure 3.2, all samples were polished and thermally etched at 1000 °C for 30 min.

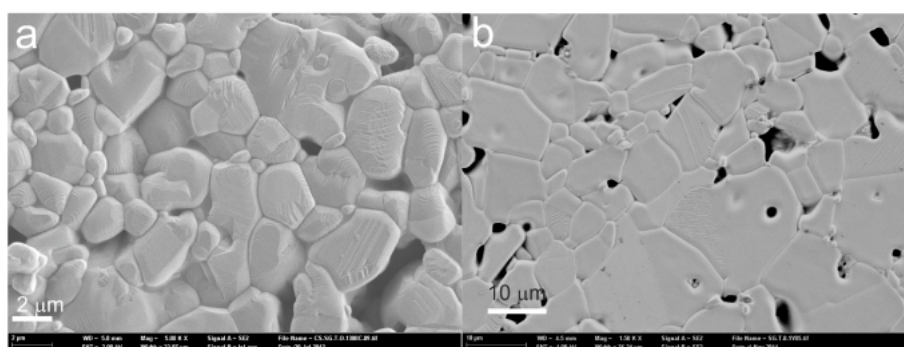


Figure 3.2: Scanning electron microscopy images of conventionally sintered TiO_2 at 1300 °C for 5 h, images taken after polishing and thermal etching at 1000 °C for 30 min (a) Undoped (b) 0.1 mol % Y doped.

3.3.2 Spark plasma sintering

Spark plasma sintering (SPS) is a special sintering process where compaction and sintering take place under electrical heating simultaneously to decrease both sintering time and temperatures, compared to CS. Preparing a highly dense ceramics without much increase in the grain size is one of the specialties of SPS. Unlike CS, SPS generates heat locally by Joule heating in the graphite molds (in case of non-conducting powders) and/or at the particle-particle contacts by passing DC pulses. A simultaneous application of uniaxial pressure by SiC push rods provides nearly fully dense samples (up to 95 %) for titania powders.

Pellets of similar size compared to CS were prepared in SPS (HP D 5, FCT Systems GmbH) by placing TiO₂ powders in 0.5 cm diameter graphite molds and uniaxially compressing at 400 MPa, 925 °C for 5 min in Ar atmosphere. The samples were heated and cooled at a rate of 300 °C/min and 100 °C/min respectively. Both Y doped and decorated samples were prepared in the SPS machine to understand the influence of dopants and dislocations simultaneously. In case of decorated samples, given the fast sintering processes in the SPS, it is expected that dopants remain very close to the GB's. Since all TiO₂ samples were reduced due to the contact with the graphite mold a post annealing treatment was given at 1000 °C for 1 h in air to reoxidize the pellets. The microstructure of pellets made by SPS is shown in Figure 3.3. Unlike CS, the grain size with SPS process were not of uniform size but ranging from 50 nm to 2 μm.

Temperature and pressure are the important parameters to create dislocations in the TiO₂ (discussed detail in the section 3.5.1), hence a different pressure - temperature combination - e.g. 40 MPa and 850 °C for 15 min was also chosen for SPS of TiO₂ powders, where no dislocations were formed. However, the density of these samples was only approx. 80 %.

3.4 Electrical characterization

3.4.1 Electrode preparation and cell assembly

For electrical characterization, electrodes were prepared on either side of the sample by applying Pt paste (Heraeus, CL11-5100) and firing at 1000 °C for 10 min

3. MATERIALS AND METHODS

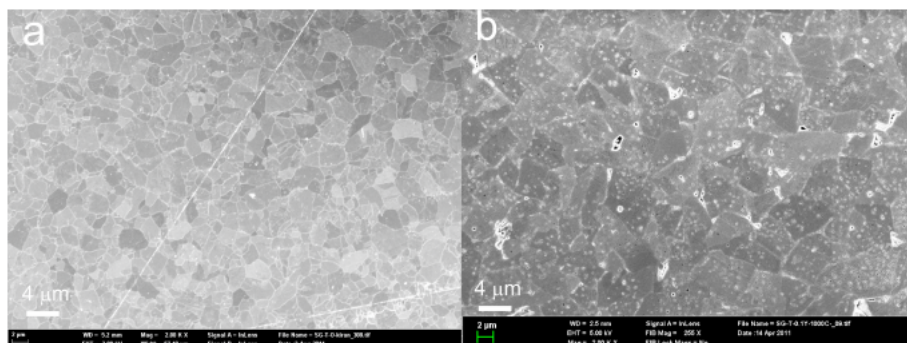


Figure 3.3: Scanning electron microscopy images of spark plasma sintered TiO_2 at $925\text{ }^\circ\text{C}$ under 400 MPa for 5 min and heat treated at $1000\text{ }^\circ\text{C}$ for 1 h , images taken after polishing and thermally etched at $1000\text{ }^\circ\text{C}$ for 30 min (a) Undoped (b) 0.1 mol \% Y decorated.

in air to remove organic compounds in the binder and establish a good contact. The electrodes established by this process are generally porous (reversible with respect to oxygen exchange to some extent), thus resulted in very small/no electrode resistance. Selectively blocking electrodes were employed for some samples to measure the partial conductivities. Such electrodes will be discussed right in the text wherever they were employed. All the samples for electrical characterization were mounted between Pt foil current collectors in a spring loaded quartz or alumina holder. The holders with the samples is placed in a gas tight quartz tube with a facility to feed in out a predetermined $p\text{O}_2$. The precise control of $p\text{O}_2$ was achieved by either mixing O_2 with N_2 or 1000 ppm O_2 with N_2 at high $p\text{O}_2$ (ranging from 10^{-1} to 10^{-5} bar); very low $p\text{O}_2$ (ranging from 10^{-17} to 10^{-28} bar) was achieved by mixing CO (1 vol \% in Argon) with CO_2 at 550°C . The equilibrium between CO and CO_2 is temperature dependent [98]; below 550°C the equilibrium shifts to deposit carbon ('sooting'). Irrespective of the gases used, the total flow rate of the gas mixtures was always set to a constant value (50 mL/min). The $p\text{O}_2$ in the exhaust gas was continuously monitored by home built lambda sensor (yttria stabilized zirconia) operated at $800\text{ }^\circ\text{C}$. A thermocouple was placed close to the sample to measure the real temperature of the samples, a precision of $\pm 1\text{ K}$ was achieved. Once the samples were fixed in the quartz cells with all other accessory units mentioned above, electrical characterization was preferred by one or more techniques mentioned below.

3.4.2 Impedance spectroscopy

Impedance measurements of the samples were performed by using a computer controlled Novocontrol Alpha-A high resolution dielectric analyzer with a ZG2 interface. An AC amplitude of 0.1 V was applied across the samples in the frequency range from 10^6 to 10^{-3} Hz. In case of bias dependent measurements, additional bias voltage was applied via an inbuilt DC source (voltage limited to ± 4 V including the AC amplitude). Calibration of the device was performed on regular basis to avoid the self drift caused by the device circuit ('internal calibration'). Additional resistive and capacitance effects caused by the cables and multiplexer (home built special circuit switch to measure more than one sample in an automated mode) were also taken into consideration by performing 'external calibration' as described in the device manual.

At a given temperature and pO_2 , impedance spectra were recorded at regular intervals of 2 h to monitor the equilibration process, this procedure was continued till stable spectra were obtained (approx. after 24 h). The measured data were fitted using Z-view (Scribner Associates Inc.) software by considering an equivalent electrical circuit that represents the physical processes expected in the electrochemical system. Based on the fitting data, the electrical conductivity (σ) and dielectric constant (ε) of the bulk and GB were calculated considering the geometry of the sample

$$\sigma_{bulk} = \frac{1}{R_{bulk}} \cdot \frac{L}{A} \quad (3.1)$$

$$\sigma_{GB} = \frac{1}{R_{GB}} \cdot \frac{L}{A} \quad (3.2)$$

$$\varepsilon_{bulk} = \frac{C_{bulk}}{\varepsilon_o} \cdot \frac{L}{A} \quad (3.3)$$

$$\varepsilon_{GB} = \frac{C_{GB}}{\varepsilon_o} \cdot \frac{L}{A} \quad (3.4)$$

where R_{bulk} , R_{GB} , C_{bulk} and C_{GB} is the resistance and capacitance of the bulk and GB respectively. A is the electrode area and L is the sample thickness.

3. MATERIALS AND METHODS

The specific GB conductivity which corresponds to the local conductivity in the low-conductivity zone at the grain boundary was calculated from [89]

$$\sigma_{GB}^{spec} = \frac{1}{R_{GB}} \cdot \frac{C_{bulk}}{C_{GB}} \cdot \frac{L}{A} \quad (3.5)$$

3.4.3 DC characterization

DC characterization of the samples was performed by a Keithley 236 source measure unit, the specifications of which include a wide operating voltage range between ± 1.1 V to ± 1100 V and current range between ± 1 nA to ± 100 mA. For testing TiO₂ single crystals or polycrystals either potentiostatic or galvanostatic measurements were conducted. In either case the voltage across the sample was limited to a range of 0.01 to 0.1 V to avoid any side reactions or irreversible changes. DC measurements were always performed in conjunction with AC impedance spectroscopy to resolve the different physical processes contributing to the observed total DC conductivity. By this, it is possible to separate the electrode contribution (if there is any) from the total conductivity for calculating the partial conductivities.

3.4.4 Wagner-Hebb polarization

Partial ionic and electronic conductivities in the total conductivity can be measured by using electrodes which selectively block one of the charge carrier species (for more details cf. the original articles by Hebb [99], Wagner [100] and Yokota [101]). For TiO₂ single crystals, a dense Au electrode of approx. 200 nm was prepared by evaporation was used as ion blocking electrode with following cell configuration Pt-paste/TiO₂/Au. The temperature for conductivity measurement was kept below 550 °C to avoid island formation by breaking Au electrodes at high temperature. In case of TiO₂ polycrystals, a dense 1 μ m thick 8 mol % yttria stabilized zirconia (YSZ) electrode was prepared by pulsed laser deposition to selectively block the electronic conductivity. The typical cell configuration is Pt-paste/YSZ/TiO₂/YSZ/Pt-paste. To avoid oxygen exchange through the edges of the TiO₂ pellet, the sample was sealed by a glass (Schott 8330, heat treated at 850 °C for 10 min). In these cell configurations always the partial conductivity of the unblocked carriers can be obtained from the steady state resistance value. It is also possible to extract the chemical

diffusivity coefficient (D^δ) from the transient (i.e., before reaching the steady state), this transient is due to the building-up of stoichiometric polarization (gradient) across the sample. Therefore, a Wagner-Hebb type polarization experiment allows one to measure partial conductivities as well as chemical diffusion coefficients of the sample at the same time.

3.5 Creating 1-D defects

1-D defects such as dislocations can be created by very simple techniques such as polishing, scratching, deformation or any other sample preparation techniques. Among these, the deformation technique is the most reliable and reproducible method to generate a high density of dislocations throughout the sample. When a crystalline solid is plastically deformed the overall periodicity is maintained by activation of slip, which is a result of formation of 1-D defects such as edge dislocations, screw dislocations or more complicated mixed dislocations and dislocation partials. For a given crystal structure, slip occurs on specific plane(s) and direction(s) which is known as the slip system(s). In case of TiO_2 rutile, extended studies were performed in early 60's to determine the slip systems [39–43, 45, 102–106], which are* $\{110\} \langle 001 \rangle$ (observed at high stress conditions) and $\{101\} \langle -101 \rangle$. These studies reveal that dislocations are formed mainly on $\{110\}$, $\{101\}$ planes and the direction of the dislocation (also known as the Burgers vector) was found to be along $[001]$.

3.5.1 Deformation Mechanism Maps

As mentioned earlier, creating dislocations by deformation is the easiest and most versatile method as the density of dislocations can be varied by altering the parameters such as pressure, temperature and dopant concentration. It is worth mentioning that it is not only dislocations that contribute to material transport (creep) but there are other mechanisms by which material can be transported during high temperature deformation. These mechanisms can be represented in single plot of stress vs temperature, which is commonly known as deformation mechanism map [107, 108].

* Slip system can also be viewed as the favorable planes where dislocations are likely to form. $\{hkl\}$ brackets represent the family of planes and $\langle uvw \rangle$ represent the family of directions

3. MATERIALS AND METHODS

Deformation mechanism maps can be constructed for any material by solving the constitutive strain rate equations (provided the material parameters are known). Based on the available literature for rutile TiO₂ [109], a deformation mechanism map was constructed by solving the strain rate equations pertaining to different creep mechanisms as given below according to ref. [108] (a detailed treatment is given elsewhere [110]).

A defect free crystal (hypothetically) can be plastically deformed by a stress exceeding the theoretical shear strength (τ_{Th}) given as

$$\tau_{Th} = 0.039G \quad (3.6)$$

At high temperatures (above $0.7 \times$ melting point) and low stresses, deformation of polycrystals is controlled by the diffusion of point defects through the bulk lattice also known as Nabarro-Herring (NH) creep. The strain rate due to NH creep (ϵ_{NH}^\bullet) is given as

$$\epsilon_{NH}^\bullet = \frac{13.3D_b\Omega P}{kTd^2} \quad (3.7)$$

At slightly lower temperatures (below $0.6 \times$ melting point), creep occurs by diffusion of point defects along the grain boundaries, this is known as Coble creep (ϵ_{Coble}^\bullet)

$$\epsilon_{Coble}^\bullet = \frac{47.5(D_{gb}\delta)\Omega P}{kTd^3} \quad (3.8)$$

At high stresses and high temperatures, the creep rate becomes a non-linear function of applied stress due to creation and movement of dislocations. This dislocation creep rate ($\epsilon_{Disl.}^\bullet$) is semi-empirically given by

$$\epsilon_{Disl.}^\bullet = \frac{AD_bGb}{kT} \left(\frac{P}{G}\right)^n \quad (3.9)$$

All the terms and constants in the above equations are described in Table 3.2. A model creep deformation map for polycrystal TiO₂ with grain size $1\mu\text{m}$ and at strain rate (ϵ^\bullet) $10^{-8}/\text{s}$ is constructed and shown in Figure 3.4. This is the lowest strain rate that can be measured experimentally, therefore the plot represents the lower limit that correspond to purely elastic (or anelastic) deformation. Increase in strain rate would lead to modification of creep deformation fields (usually contract,

see ref. [108]). Since the actual strain rate during sintering is not known it is better to compare it with the lowest strain rate deformation map. The fields in the map represents the rate controlling mechanism for creep deformation. The boundaries of the fields were obtained by equating the respective creep rate equations given above.

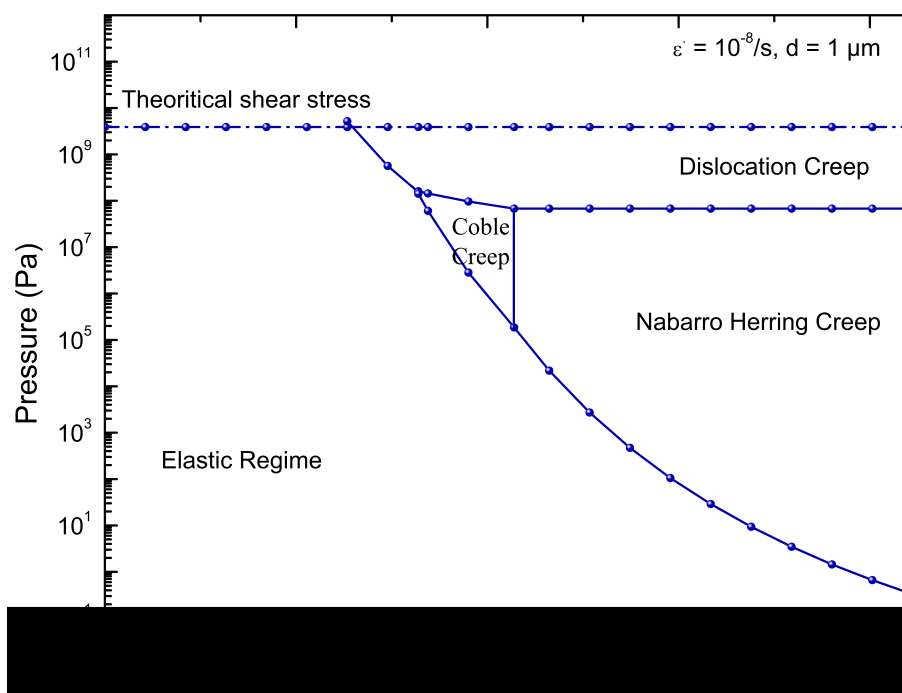


Figure 3.4: Deformation mechanism map for polycrystalline rutile TiO_2 with $1 \mu\text{m}$ grain size, constructed based on the data available in ref [109]

3.5.2 Dislocation Generation

As described in section 3.5.1, dislocations can be generated by choosing the right temperature-pressure combination (i.e. at high temperature and pressure, see Figure 3.4). In case of single crystals the dislocation creep regime shown in the Figure 3.4 gets enlarged by extending the dislocation creep boundaries to lower temperatures and pressures. Therefore, it is easy to create dislocations even at low temperatures in single crystals. In this study [001] and [110] crystals were uniaxially pressed in a hot press under a pressure of 40 MPa at 1200 °C for 5 min. A high temperature was chosen in order to generate high density of dislocations through out the sample. After the compression treatment, all crystals were annealed at 1200 ° for 5 h in air

3. MATERIALS AND METHODS

Table 3.2: Creep data for rutile TiO₂ according to ref [109]

Parameter	Value
Atomic volume, Ω (m ³)	3.11x10 ⁻²⁹
Burgers vector*, \mathbf{b} (m)	3x10 ⁻¹⁰
Melting temperature, T_m (K)	2112
Shear modulus, G (Pa)	100x10 ⁹
D_b° for bulk diffusion†, (m ² /s)	3.5x10 ⁻⁶
Activation energy for D_b , Q_b (kJ/mol)	2.51x10 ²
D_{GB}° for GB diffusion*, (m ² /s)	7x10 ⁻⁶
Activation energy for D_{GB}^* , Q_{GB} (kJ/mol)	2.01x10 ²
Stress exponent, n	3
Dorn parameter, A	3
Grain size, d (m)	1x10 ⁻⁶
Structural grain boundary width, w (m)	5x10 ⁻¹⁰

P is the applied stress (Pa)

and k is the Boltzmann constant

† this corresponds to apparent diffusion

due to $V_O^{\bullet\bullet}$ and $Ti_i^{\bullet\bullet\bullet\bullet}$

*assumed

to reoxidize the samples after the reducing conductions in the SPS graphite die. In case of polycrystalline ceramics, SPS at 925 °C under 400 MPa pressure generated dislocations in the sample.

3.6 Creating 2-D defects

2-D defects can be broadly classified into stacking faults and boundaries (homogeneous or heterogeneous). Since boundaries are very frequently observed in ceramics, we focused mainly on homogeneous grain boundaries without any second phase in this study. In order to have an in depth understanding of grain boundaries, bicrystals with special Σ or low angle tilt boundaries were prepared.

3.6.1 Bicrystal Preparation

Symmetrical tilt bicrystals with Σ 5 (210) and 6° tilt boundary were prepared by bonding custom diced rutile TiO₂ single crystals supplied by SurfaceNet GmbH

(Rheine, Germany). To make a $\Sigma 5$ boundary, $[210]$ oriented single crystals (with large surface parallel to (210) plane) were prepared by keeping one of the edges perpendicular to the c -axis i.e. (001) see Figure 3.5. In order to form a symmetric tilt boundary one of the two crystals was rotated by 180° around the $[210]$ axis, before joining them on their common plane of contact i.e. (210) plane. This step is decisive to form a symmetric tilt boundary along $[001]$. In case of the 3° symmetric tilt boundary along $[001]$, single crystals cut long (100) planes with a 3° offset towards (110) , see Figure 3.5. To form a symmetric tilt, one of the crystals was rotated on its large surface as mentioned earlier.

After orienting, the crystals were glued on the edges (UHU hart adhesive) to keep

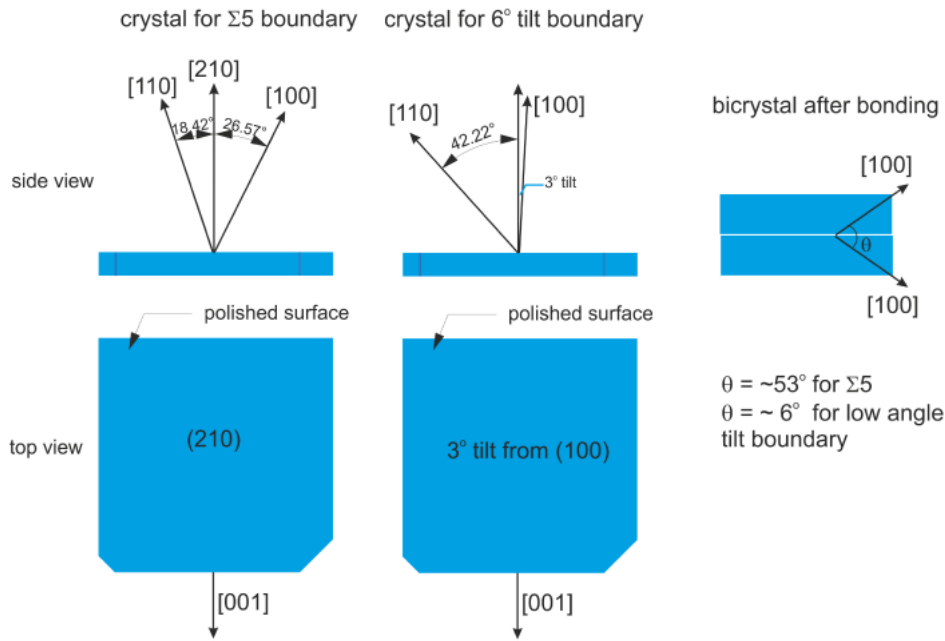


Figure 3.5: Orientation of single crystals for making $\Sigma 5$ and 6° symmetric tilt TiO_2 boundaries

the alignment intact until the crystals were held tightly by the push rods in the diffusion bonding furnace. The adhesive does not react with TiO_2 and is completely removed (evaporated, oxidized) at $\sim 400^\circ\text{C}$ prior to the diffusion bonding. To avoid any cross contamination between push rods and the crystals at high temperatures, a spacer was used between the SiC push rod and TiO_2 crystal, as shown in Figure 3.6. Since TiO_2 is non-reactive with SiC, spacers made from the same material were

3. MATERIALS AND METHODS

used. To establish a firm bonding, the crystals were held under a pressure of 4 MPa at 1400 °C for 90-120 min. A slow heating and cooling rates were employed to avoid any thermal stresses in the crystals, typically ± 2 K/min. The holding pressures should not exceed beyond 5 MPa, since a higher pressure would lead to the generation of dislocations as mentioned in the previous section. After diffusion bonding the obtained bicrystals were annealed in pure oxygen at 1200 °C for 10 h. The influence of dopant decoration in the GB was studied by depositing the dopant on one of the bonding surfaces prior to diffusion bonding. Two different dopants were studied in this work, viz. Y_2O_3 (acceptor) and Nb (donor). Yttria is deposited by PLD process with a thickness of approximately 0.5 nm or 1 nm which corresponds to approximately 1 or 2 monolayers respectively. For donor decoration, 1 nm thick Nb metal is evaporated on the TiO_2 single crystal surface.

For TEM characterization, samples were cut parallel to the (001) edge in such a way that the electron beam axis will be parallel to the [001] direction. Electrical characterization was performed across the single GB by applying Pt paste electrodes on either side of the large surfaces and fired at 1000 °C for 30 min.

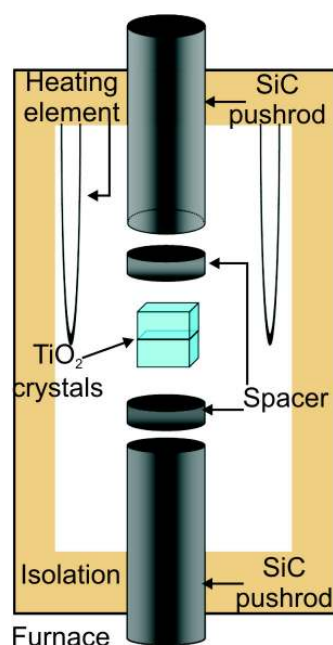


Figure 3.6: Schematic drawing of the diffusion bonding furnace used for preparing bicrystals

3.7 1- and 2-D defect characterization

3.7.1 Transmission electron microscopy

Transmission electron microscopy (TEM) is one of the best characterization techniques that is available for analyzing structural defects. In this work, different microscopes were employed depending on the aim of the study. The different transmission electron microscopes used for this study and their characteristic features are described below

- **Philips CM 200 microscope** was used for characterizing dislocations in single crystal and polycrystalline TiO₂ samples. The key advantage of this microscope over other high energy microscopes comes from its high tilt angles along A axis ($\pm 60^\circ$) and B axis ($\pm 30^\circ$), which makes it ideal for characterizing dislocations. The microscope was operated at 200 kV (LaB₆ as electron source) with a point to point resolution of 2.7 Å.
- **JEOL 4000FX microscope** was used mainly to characterize the grain boundary structure of the bicrystals. This high resolution microscope was operated at 400 kV (LaB₆) with a point to point resolution of 2 Å. The maximum tilt is restricted to $\pm 30^\circ$ along A axis and $\pm 15^\circ$ along B axis.
- **ZEISS 912 Omega microscope** was used to characterize the pore like features in polycrystalline TiO₂ mainly using the built-in EELS. The operating voltage was 120 kV (LaB₆) and the spatial resolution and energy resolution for EELS analysis was 20 nm and 1 eV respectively.

3.7.2 TEM sample preparation

TEM specimens were prepared by the tripod or the classical method [111], both methods worked well and did not show any significant difference. The tripod method was mainly used only for preparing specimens from the cross-section of TiO₂ single crystals. The procedure involves initial grinding and polishing (Allied Multiprep system) followed by a wedge preparation (Allied systems). After wedge preparation, the specimens were ion milled (Ar⁺ ions) to achieve electron transparent specimens.

3. MATERIALS AND METHODS

This process also avoids artifacts arising due to mechanical polishing. Ion milling (PIPS I 691 or PIPS II 695) was performed in a double modulation mode, where two Ar guns (3 keV) were placed at 8° angle to the specimen from top and bottom. Milling takes place simultaneously on both sides with continuous rotation of the sample (1.5 rpm). A final finishing of the specimen was achieved by sputtering Ar ions at a low energy (0.3 keV).

In case of the classical method, specimens were dimpled (concave shape on one side) on a dimple grinder (Gatan dimple grinder 656) after initial mechanical polishing (Gatan disc grinder 623). After dimpling, the specimens were ion milled in the same procedure as mentioned for the tripod method. Specimen preparation and characterization was performed at MPI-IS StEM group, single crystals and polycrystalline TiO_2 samples were prepared by M. Kelsch and bicrystals by U. Salzberger.

3.7.3 Oxygen Isotope Exchange Experiments

Unlike chemical diffusion experiments which are driven by the chemical potential gradient along with migration of cation ($\text{Ti}_i^{\bullet\bullet\bullet\bullet}$) as well as cation ($\text{V}_O^{\bullet\bullet}$) defects in TiO_2 , oxygen isotope exchange (tracer diffusion) experiments provides information selectively about oxygen transport without any chemical gradient. Since conductivity is a function of concentration and mobility of the defect, this technique helps to distinguish the conductivity due to oxygen ions from several other ions (for e.g. in TiO_2 both anions and cations are considered to be mobile [26, 77]) contributing to the ionic conductivity.

For oxygen tracer diffusion experiments it is essential to equilibrate the samples in the same $p\text{O}_2$ and temperature of ^{16}O prior to ^{18}O exchange. The preannealing must be at least 10 times longer than the actual tracer annealing in order to obtain a reliable oxygen tracer diffusivity (D^*) and surface exchange coefficient (k^*). A detailed overview of the proper choice of exchange conditions is given in reference [112].

For a better comparison, all TiO_2 crystals (pristine and compressed) are mechanically polished prior to preannealing treatment. The polishing damage is not healed-out in both samples as this might change the dislocation density in the compressed samples. The preannealing treatment was done in 'technical quality' ^{16}O gas exhibit-

ing natural (^{18}O) isotope abundance of 0.2 %^{*}, with 0.5 bar chamber pressure. After preannealing treatment, samples were quenched by removing the furnace from the sample containing chamber and refilled with rich ^{18}O gas (99 %) with same amount of $p\text{O}_2$. In case of TiO_2 single crystals, different ^{18}O exchange times were selected based on the exchange temperature, typically 2 days at 700 ° and 800 °C and 1 day at 900 °C and 1000 °C. During the experiment, the gas composition was recorded by a mass spectrometer (BALZERS Prisma quadrupole, U.S.A), to analyze the background isotope concentration in the preannealing gas (c_{bg}^*) and concentration of ^{18}O in the isotope exchange gas (c_g^*).

3.7.4 Secondary Ion Mass Spectroscopy

After isotope exchange experiments, secondary ion mass spectroscopy (SIMS) was employed[†] to measure the oxygen tracer concentration profiles. Time of flight SIMS (TOF-SIMS-IV, ION-TOF, Germany) analysis is the state-of-the-art equipment which can analyze all the elements in the periodic table with a high lateral (< 60 nm) and depth (< 1nm) resolution.

In this work, samples were mainly analyzed in depth profiling mode where two ion beams (sputter gun and primary gun) operate alternatively. For analyzing ^{18}O profiles in TiO_2 single crystals, a 300 μm x 300 μm crater was initiated by the sputtering gun - operated at 160 nA with 2 keV Cs^+ ion beam. After each sputter cycle, Ga^+ primary ions were bombarded at the center of the cratered surface (raster scanned over 50 μm x 50 μm) to cascade the secondary ions which are analyzed by the detector. The primary Ga^+ ion gun was operated in burst mode (with 8 short pulses) at 25 keV energy by passing 0.1 pA current. To avoid charging effects on the insulating samples, electrons were flooded intermittently by an electron flood gun (operated at 12 μA with 20 eV). All these steps were repeated successively until the ^{18}O concentration decreased to natural abundance in the sample. The key advantage of this method to record the entire data both laterally as well as with depth allowing to reconstruct the ^{18}O profiles in 2D sections or in 3D. For depths greater than 3 μm , line scanning over the cross-section of the samples was preferred.

^{*}A higher purity oxygen often has a higher ^{18}O content than natural abundance due to the purification process

[†]operated by T. Acatürk, MPI-FKF, surface analysis group

3. MATERIALS AND METHODS

This was done by cutting the sample and polishing the cross-section prior to SIMS analysis. Unlike depth profiling, data of line scanning measurement was calculated from color intensity of the 3D constructed images.

Part I

Results and discussion on 1-D defects

4

Single crystal TiO₂

Single crystals are the most simple and ideal systems for characterizing dislocations and their effect on transport properties. This can be attributed to the fixed degrees of freedom between the load axis and the crystal orientation in comparison to polycrystalline materials. This is one of the key reasons why most fundamental studies on dislocations in TiO₂ were based on single crystals [40–42, 45, 104, 105]. Since one of the key motivations of this work is to investigate the effects of dislocations on the electrical properties, it is important to start on single crystals to understand the fundamental properties.

Extensive work on dislocation characterization in TiO₂ was done in the early sixties, especially in the context of their mechanical properties. The early studies by Hirthe and Brittain [39, 40] revealed that slip occurs in TiO₂ by the {110} <001> slip systems * at high temperatures (750 °C to 1050 °C) and stresses (20 MPa to 90 MPa). It was also observed that at low stresses the {10-1} <101> slip systems become active [104]. Ashbee et. al. studied the stress-strain relationships for rutile single crystals as a function of crystal orientation and compression axis and observed that irrespective of the orientation, the favorable slip system remained the same i.e. {-101}<101> and {110}<001> [41]. Several other independent studies confirmed the same slip systems [42–45] in TiO₂.

Since the favorable planes for dislocations are {110}, two samples were chosen for

* Slip system can also be viewed as the favorable planes where dislocations are likely to form. {hkl} brackets represent the family of planes and <uvw> represent the family of directions

4. SINGLE CRYSTAL TiO_2

electrical characterization viz. $[001]$ and $[110]$ orientation. These two samples allow one to study the overall effects of dislocations. In the $[001]$ sample (compression and electrical measurement axis along $[001]$), the slip planes are aligned parallel to the electrical measurement axis, representing the conductivity along the dislocations. And in the $[110]$ oriented samples, dislocations will be perpendicular to the electrical measurement axis. To study the effect of varying dislocation densities, samples for electrical characterization are prepared from center and corner portions of the compressed sample (see section 3.5.2 for experimental details).

4.1 Defect characterization

Dislocations in single crystals are characterized on Philips CM 200 transmission electron microscope operated at 200 kV in bright field as well as in dark field modes. Sample preparation techniques are discussed in detail in the section 3.7.2. Before analyzing any compressed samples, a TEM specimen was prepared from the pristine crystal to check for artifacts arising due to sample preparation techniques. From Figure 4.1 it is convincing that the specimen preparation methods did not create any artifacts, especially no dislocations. No dislocations are observed over large areas.

TEM specimens were prepared from plan and cross-sections of both $[001]$ and

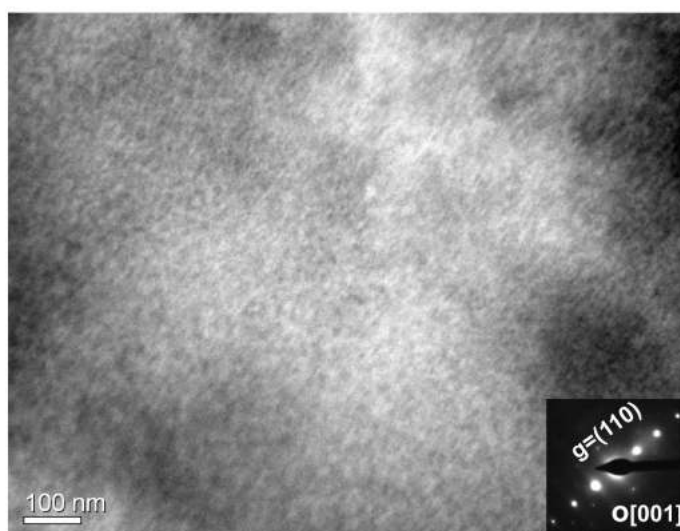


Figure 4.1: Bright field TEM image of pristine TiO_2 crystal, specimen prepared from $[001]$ orientation with beam axis parallel $[001]$.

[110] orientated samples. The cross-section orientation of the [001] sample is parallel to [110] and vice versa for [110] oriented sample as shown in Figure 4.2, this helps to understand the dislocations confining to these main directions. Dislocation characterization of each orientation is discussed below separately.

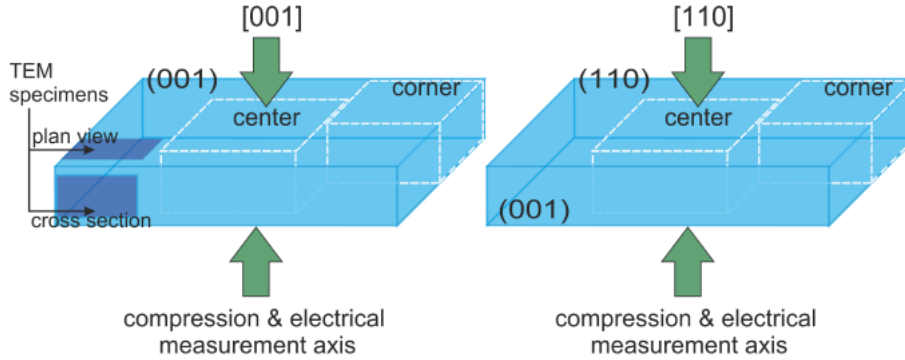


Figure 4.2: Schematic representation of crystal orientation with respect to the applied load. Specimens for TEM and electrical characterization are also represented.

4.1.1 TEM on crystals compressed along [001]

Figure 4.3 shows the bright field TEM image of the [001] plan view sample, with beam axis parallel to the c -axis. As described in figure 2.3, the contrast in the image arises when the Bragg condition is nearly met at dislocations. Therefore, the dark featured lines in the bright field mode correspond to the dislocations; the inset in the figure shows the selected area diffraction (SAD) taken at different regions (as marked) without changing the zero beam axis from the initial conditions. The shift in the SAD pattern indicates that there is a slight tilt in the regions close to the dislocations arising from local strain. Translation of the reciprocal lattice vector or diffraction vector (\mathbf{g}) on to the real space image shows that the dislocations are parallel to $\{110\}$ planes.

To characterize the dislocation orientation, a two beam condition is the best possible technique where only one reflex is activated along with the zero beam [113]. Figure 4.4a shows the two beam condition operating for the [001] cross-section view sample, with only $\{110\}$ planes diffracting along with the zero beam. As already explained from Figure 2.3, strong contrast is achieved in this mode when the dislocations lie on

4. SINGLE CRYSTAL TiO₂

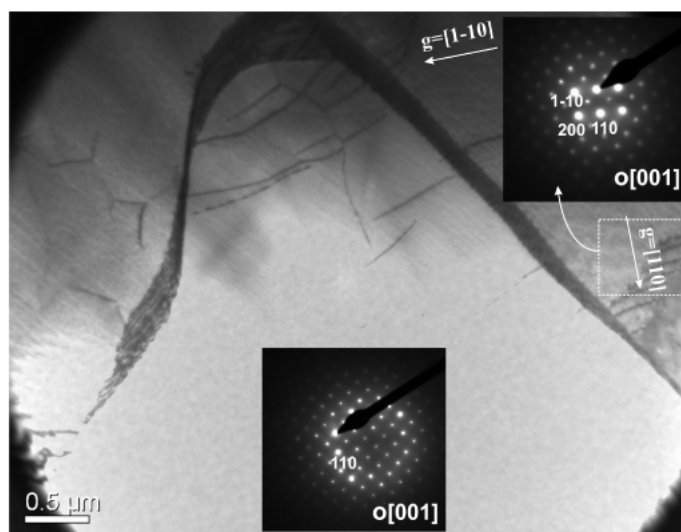


Figure 4.3: Bright field TEM image of [001] TiO₂ crystal, specimen prepared from plan view with beam axis parallel to [001].

the diffracted beam. The dark field* image at the same location is shown in Figure 4.4(b) confirming the observed features are dislocations that preferably lie on {110} planes. This method also helps to differentiate dislocations from other artifacts such as cracks, as the latter appear the same in both modes without any contrast change. The contrast features at the top-left corner of the image are thickness fringes due to thickness variation of the sample.

A point worth noting here is that the TEM analysis was performed after the post-compression annealing at 1200 °C for 5 h in air. The fact that still a high density of dislocations is observed in TEM indicates that these dislocations are very stable and will persist at moderate temperatures over prolonged times (discussed more in the later sections). As a rule of thumb, the typical temperature for the healing of line defects is approximately half the melting point of the material; however in case of rutile it is even higher [106] and only 30 % of recovery was found at 1000 °C even after annealing for 17 h. Thus the dislocations and their effect on conductivity will be persistent at intermediate temperatures.

*In dark field mode, the objective aperture is placed over the 110 diffraction beam to achieve specific orientation information by illuminating {110} planes which meet the Bragg condition.

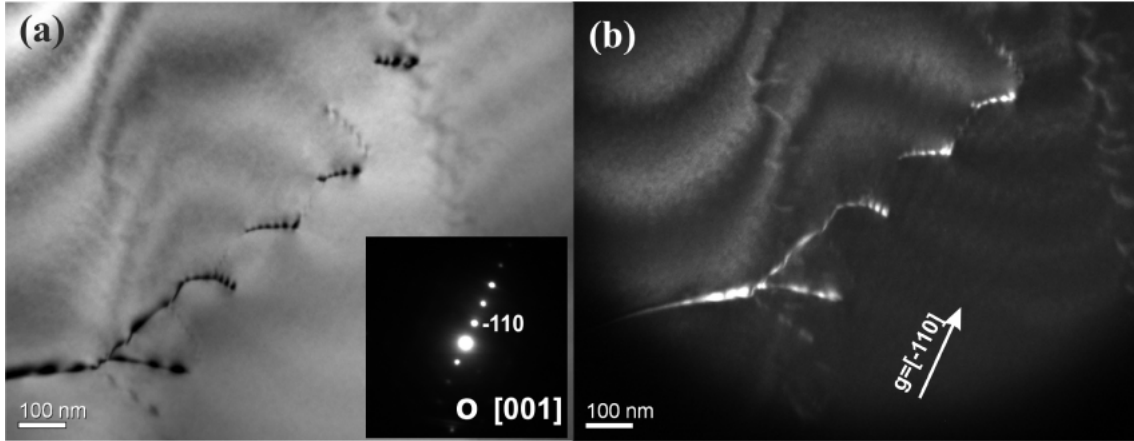


Figure 4.4: (a) Bright field TEM image of [001] sample prepared from cross-section, two beam condition with diffraction vector = (-110) operating along with beam axis parallel to [110]. (b) Dark field image from the same location.

4.1.2 TEM on crystals compressed along [110]

Figure 4.5(a) shows the bright field TEM image of the plan view [110] sample with only the [001] reflex operating. By placing the aperture over the diffraction vector $\mathbf{g} = (001)$, the bright field mode is changed to dark field mode as shown in Figure 4.5(b). It is also possible to characterize the direction of the dislocation known as Burgers vector (\mathbf{b}). To identify the direction of a particular dislocation, it has to be imaged with several possible diffraction vectors (\mathbf{g}) with a two beam condition. The procedure has to be continued till a condition is met where the dislocation vanishes, corresponding to $\mathbf{b} \cdot \mathbf{g} = 0$. The physical meaning of this expression is that the dislocation direction is perpendicular to the diffraction vector and it is not possible to view it in the given two beam condition. This procedure is very tedious and is not in the motivation of the current work. However, based on the earlier findings on Burgers vector of dislocations, a brief analysis was performed on one of the dislocations. Figure 4.6(a) shows dislocations in [110] plan view sample under two beam conditions with only the 001 reflex operating. The same image is viewed in another reflex $\mathbf{g} = (-110)$ to vary their contrast and or even to vanish when their Burgers vector is perpendicular to the diffraction vector. Interestingly the dislocation at the position marked 'X' in Figure 4.6(b) disappears when $\mathbf{g} = (-110)$. The only vector that satisfies this condition would be [001] or [110], where the latter

4. SINGLE CRYSTAL TiO_2

is not possible as dislocations with high contrast were observed on this \mathbf{g} vector earlier. So, the Burgers vector for dislocations is $[001]$ which is in agreement with the literature. More details of such an analysis can be found in ref. [103].

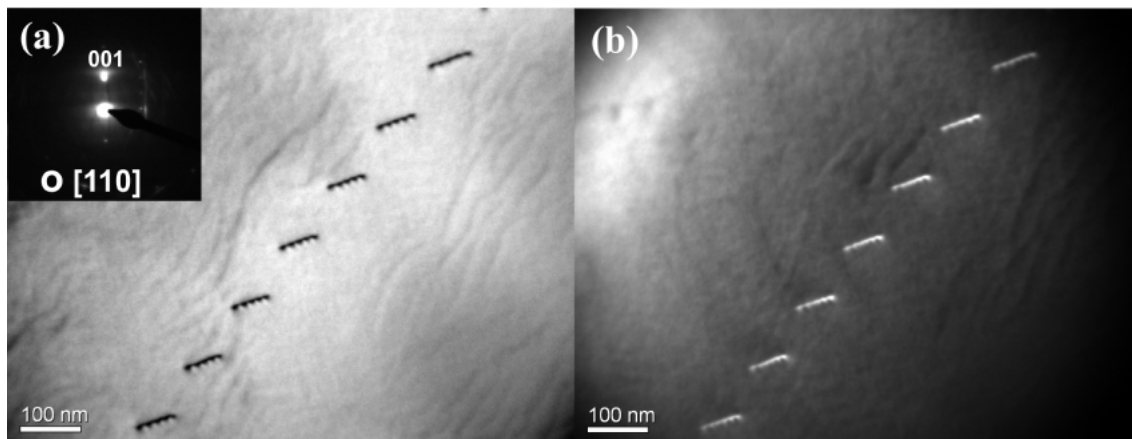


Figure 4.5: (a) TEM-bright field image of $[110]$ plan view sample with two beam condition operating with beam axis parallel to $[110]$ and $[001]$ diffraction vector. (b) Dark field image from the same location.

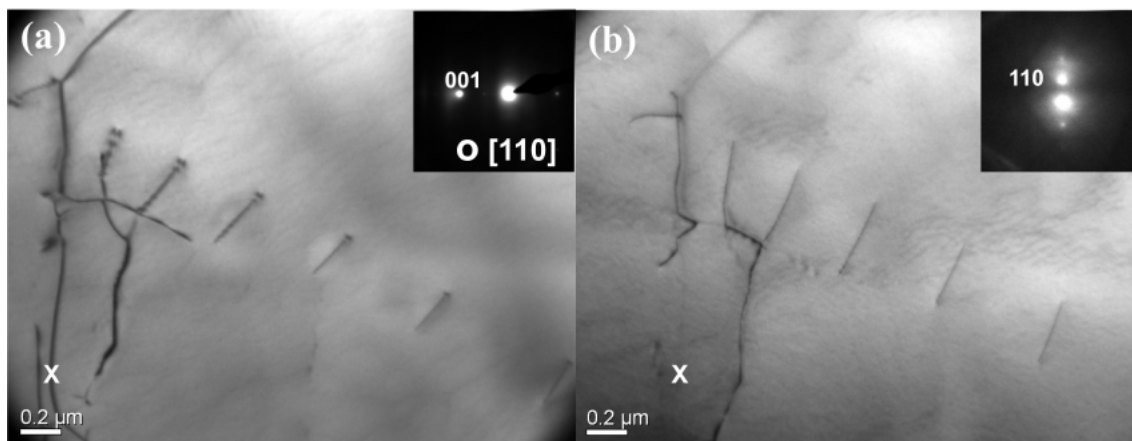


Figure 4.6: TEM-bright field image of $[110]$ plan view sample with beam parallel to $[110]$ (a) two beam condition with only $[001]$ reflex operating (b) $[110]$ reflex operating.

Figure 4.7 is obtained from the $[110]$ sample, with a specimen prepared from cross-section. Similar to other pictures, the image was taken with a two beam condition ($\mathbf{g} = (-110)$) and beam axis parallel to $[001]$. The inset shows the diffraction

patterns close to pole, the features are very similar to the plan view [001] sample with slight tilt at the dislocation bundle. From Figures 4.3-4.7 it can be recognized that the overall nature of the dislocations seems to be the same irrespective of the loading direction (i.e. either parallel to [001] or [110]). The dislocations are always formed, and the slip system remains to be unaltered as described in the literature [39–45, 103–105].

It is difficult to calculate the density of dislocations from images with dislocation

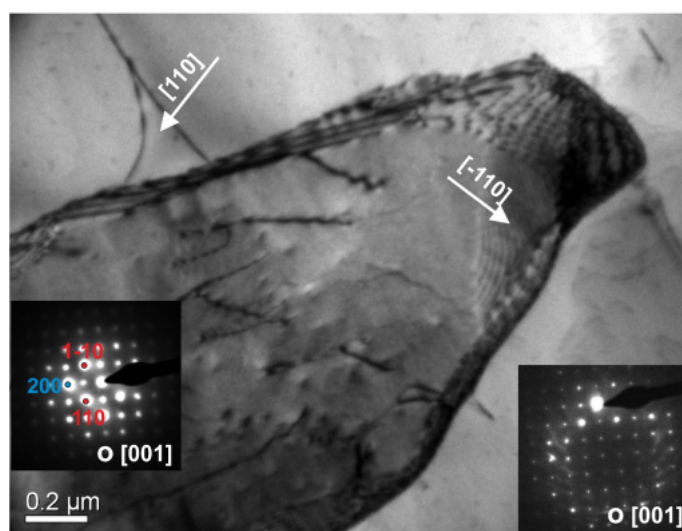


Figure 4.7: TEM-BF image of [110] sample prepared from the cross-section with two beam condition operating with $\mathbf{g}=(-110)$ and beam axis parallel to [001]. Insets show the diffraction pattern of the corresponding regions.

bundles, however a rough approximation was made based on images from plan view of [110] crystals (e.g. Figure 4.5), which yields approx. $10^{13}/\text{m}^2$. For this density the average distance between the dislocations can be calculated*, which is approx. $0.3 \mu\text{m}$. At this point it is worth stressing that dislocations need not to be a straight line (as for pure edge dislocations). In reality, as shown in the TEM images above, more complicated features appear by interaction with other dislocations, which is energetically favorable. Hence, a thoughtful way of characterizing the electrical properties is to measure parallel to the slip planes where the measurement axis contains all the planes with dislocations and vice versa.

*assuming dislocations had pure edge character and extend throughout the whole sample thickness

4.2 Electrical characterization

The electrical conductivity of TiO₂ is slightly anisotropic, it was observed that conductivity along the c-axis is approximately 10 times higher than the [110] axis [114]. Cation impurity tracer diffusion experiments by Sasaki et al. [31] revealed that the cation diffusivity (especially divalent cations like Co²⁺ and Ni²⁺) along the c-axis is at least an order of magnitude higher compared to diffusion along a or b-axis. Therefore, conductivity data for [001] samples and [110] samples are represented separately and always compared with samples of the same orientation without compression (i.e. pristine samples). Considering the possibility of varying dislocation density within the same sample, two pieces were prepared from the 10×10 mm² compressed sample, one from the center portion (named as 'center') and the other from one of the corners (named as 'corner').

4.2.1 [001] oriented crystals

Electrical characterization of the samples with compression and electrical measurement axis along [001] were performed by impedance spectroscopy and the representative spectra for pristine and compressed sample is shown in Figure 4.8. As expected, the impedance spectrum of the pristine sample indicates a single relaxation process corresponding to the bulk process. Based on the capacitance value (10⁻¹² F), the relative permittivity (ϵ_r) was calculated (approx. 95), which is close to the bulk permittivity of TiO₂ (see Table 2.1). Hence, the observed single semicircle corresponds to the bulk conductivity. A tail (arc) at the low frequency is due to the resistance from Pt paste electrodes. With dislocations in [001] sample (indicated as 'disl.') two major changes were observed. Firstly the high frequency semicircle has shrunk indicating decreased bulk resistance (shown as inset in the Figure 4.8); and the electrode contribution has extended to higher resistance similar to a Warburg diffusion process. This is a characteristic feature of electrode polarization that is usually observed when one of the mobile charge carriers is blocked at the electrodes. Based on this analysis, impedance spectra point towards a change in the dominant charge carriers in the system.

Electrical conductivity is plotted as a function of pO_2 to elucidate the point defect chemistry of TiO₂ (cf. section 2.3). Figure 4.9 describes the conductivity depen-

4.2 Electrical characterization

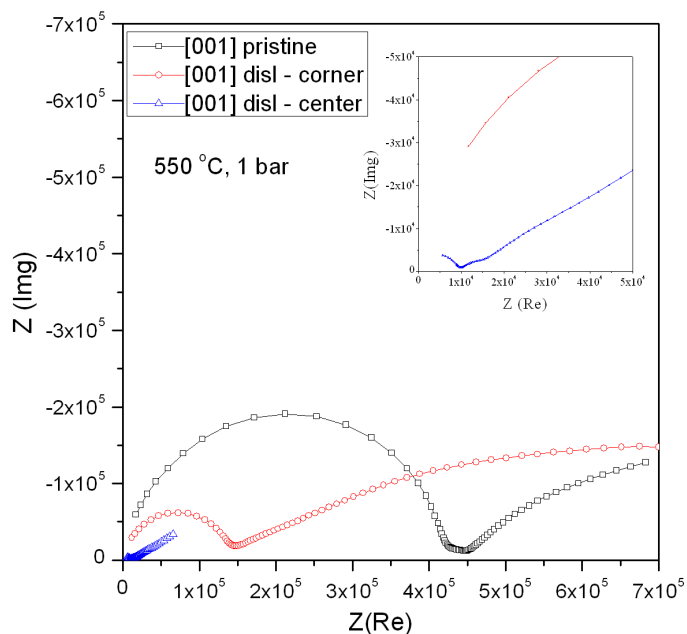


Figure 4.8: Impedance spectra of [001] sample with ('disl.'- corner and center) and without dislocations (pristine). $\psi_{HF} = 0.95$ and 0.99 respectively.

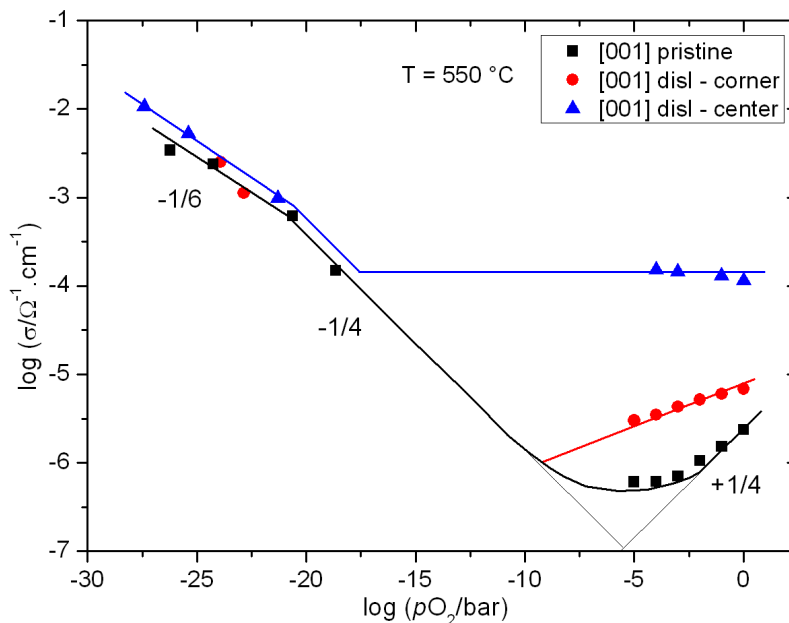


Figure 4.9: Electrical conductivity as a function of pO_2 for [001] sample with ('disl.'- center and corner) and without dislocations ('pristine'). 'Center' and 'corner' indicate samples from different regions of the compressed sample. The slopes in the low- pO_2 regime are drawn according to the values expected from the bulk defect chemical model.

4. SINGLE CRYSTAL TiO₂

dence on the oxygen partial pressure for [001] sample with and without dislocations at 550 °C. Samples from two locations (center and corner) are compared to show the effect of dislocation density on the electrical properties. The 'corner' sample is believed to have a lower density of dislocations compared to the 'center' sample. The conductivity vs pO_2 plot for the pristine crystal is in agreement with the literature [3, 26, 38, 73] and also as expected from the known bulk defect chemistry (shaded region in Figure 2.4). At high pO_2 and moderate temperatures, TiO₂ is a hole conductor with a pO_2 exponent of +1/4 according to equation (2.10) with an approximate acceptor concentration of 100 ppm (ICP-OES). At low pO_2 , the increase of $V_O^{\bullet\bullet}$ concentration by the reduction reaction leads to a pO_2 exponent, $m=-1/6$ as described by eq. (2.8).

With presence of a high density of dislocations the following changes are observed:

1. At high pO_2 (1 bar to 10^{-5} bar) the overall conductivity is strongly enhanced, which is more pronounced for the 'center' sample with high dislocation density;
2. In this region, the pO_2 exponent is decreased compared to the untreated pristine crystal, the changes are more prevalent in the 'center' sample.
3. At low pO_2 there is essentially no change in the conductivity, leading to an unchanged pO_2 exponent compared to the pristine crystal.

Firstly, the conductivity rise at high pO_2 due to dislocations can be attributed to the increased positive charge carriers that can be either h^\bullet , $V_O^{\bullet\bullet}$ or $Ti_i^{\bullet\bullet\bullet\bullet*}$. In order to satisfy the overall charge neutrality condition there must be also a corresponding amount of negatively charged defects in the system. Since the acceptor impurity content is fixed and considered to be immobile (same as in pristine crystal) and there is no significant contamination of the sample during compression treatment (contact only with graphite sheets), these negatively charged defects should be intrinsic defects. The only possible negatively charged intrinsic defect in TiO₂ is $V_{Ti}^{\prime\prime\prime}$, as the other defect $O_i^{\prime\prime}$ is energetically not favorable due to the closely packed oxide ion lattice in rutile structure (even if the structure in dislocation cores might be

*other defects preferably formed at high pO_2 can be ruled out: $O_i^{\prime\prime}$ -defects are energetically hardly possible [71] and $V_{Ti}^{\prime\prime\prime}$ -defects have such a low mobility [78,115] that they would not influence the conductivity

slightly less densely packed, still the possibility of O_i'' is improbable). Theoretical calculations proved their formation energy in the bulk as well as in the $[100]\{05-1\}$ symmetric GB is rather high and unrealistic [71]. DFT calculations also yield a much higher bulk formation energy for $O_i''+V_O^{\bullet\bullet}$ defect pairs compared to $Ti_i^{\bullet\bullet\bullet\bullet}+V_{Ti}^{\prime\prime\prime}$ for all possible Fermi energies under reducing conditions [116] similar to the compression treatment. Further, negative dislocation core charge due to acceptor impurity segregation is also very unlikely, considering the low impurity content (approx. 100 ppm) of the samples and the observed enhancement in the conductivity (approx. 3 orders in magnitude), which would correspond to $[A'_{Ti}] \sim 1\%$ according to Equation (5.2) (cf. Section 5.2.3). To maintain the global charge neutrality all defect charges have to be balanced and the acceptor impurities alone can not explain this enhanced conductivity. From these arguments, it can be understood that creation of cation vacancies in the dislocation core leads to the observed increase in the positively charged carrier concentration in the adjacent accumulation zones.

Secondly, the varying conductivity with changes in the dislocation density (corner vs. center sample) can be understood as the variation of positively charged carrier concentration in the system. The more negatively charged dislocations present, the higher will be the charge compensating positively charged mobile defects.

Finally, the absence of changes in the conductivity at low pO_2 is intriguing at a first glance, but is related to the fact that the modified transport at high pO_2 is not due to the regular bulk point defect chemistry but related to dislocations. The differences in these regions in comparison to the bulk defect chemistry will be discussed in the following Section 4.5.

Figure 4.10 compares the conductivity as a function of temperature for the pristine crystal from the present work as well as data from literature with the compressed crystals. The high activation energy at high temperature for Blumenthal and Cronmeyer data is due to intrinsic compensation in TiO_2 . There is a change in the activation energy at low temperatures (Cronmeyer data) due to extrinsic compensation. In the present work, the activation energy of the pristine sample is in between these two limits. The variation in the activation enthalpy for conduction for crystals with dislocations, suggests a variation in the conduction mechanism due to modification of the charged defects and their transport. The activation energy for the sample with highest dislocation density is lower than the known ionic defect migration en-

4. SINGLE CRYSTAL TiO₂

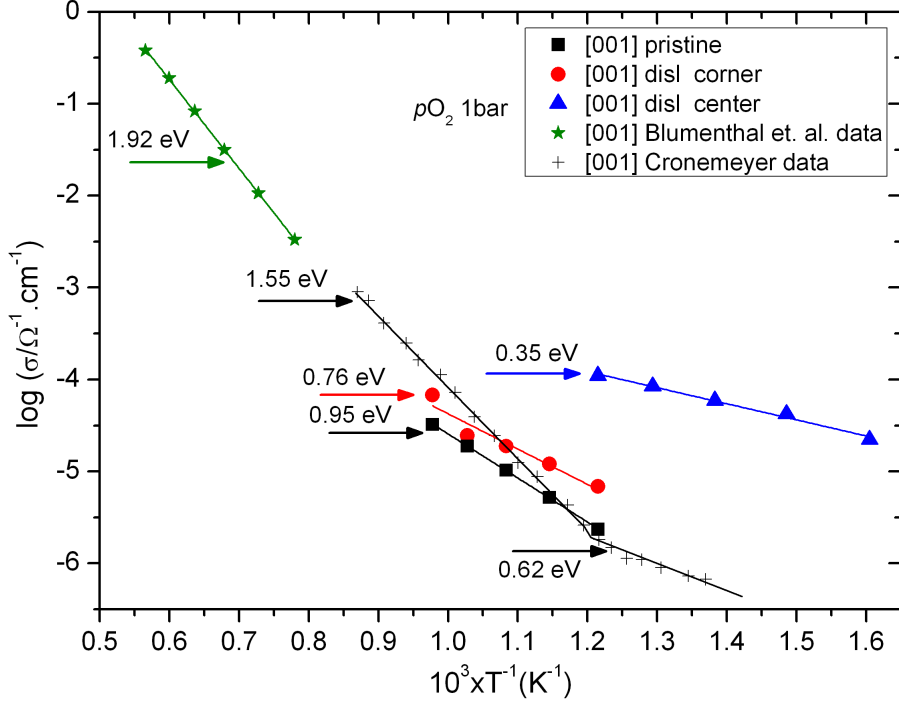


Figure 4.10: Electrical conductivity as a function of reciprocal temperature in 1 bar oxygen for the [001] sample with ('disl.') and without dislocations(pristine). Center and corner indicates samples from different regions of the compressed sample compared with data from literature [29, 75].

thalpies [26, 77], which is 0.8 eV for $V_{\text{O}}^{\bullet\bullet}$ and 0.7 eV for $\text{Ti}_i^{\bullet\bullet\bullet\bullet}$. This could be due to space charge accumulation effects being more pronounced at lower temperatures (explained in section 4.5) and/or due to strain fields in the dislocation region facilitating faster ionic motion as tensile strain could decrease ion migration barriers e.g. in fluorite oxides [17, 23–25].

4.2.2 [110] orientated crystals

Figure 4.11 shows the impedance spectra of pristine and compressed [110] samples. There is no polarization at the electrodes in either samples indicating a pure electronic conductivity of the samples. Figure 4.12 describes the electrical conductivity of [110] crystals as a function of $p\text{O}_2$, the +1/4, -1/4 and -1/6 slopes when reducing $p\text{O}_2$ to from high to low values, is in agreement with the bulk point defect chemistry of TiO_2 described in section 2.3. In contrast to the [001] samples, the

4.2 Electrical characterization

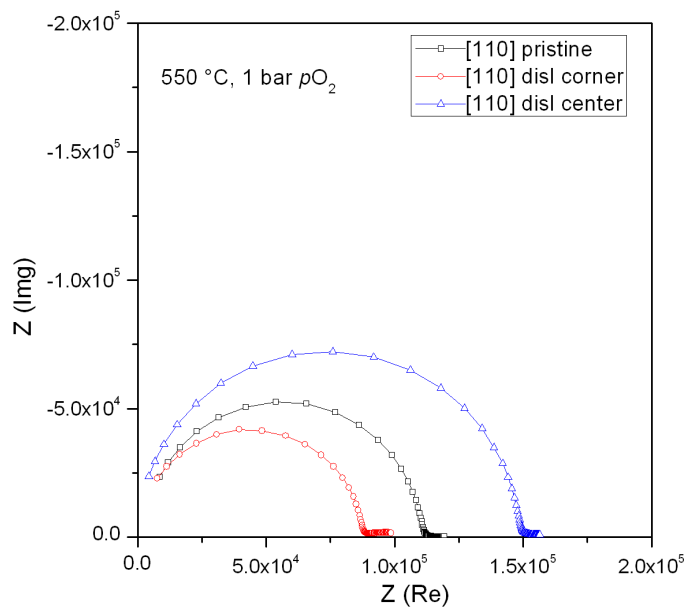


Figure 4.11: Impedance spectra of [110] sample with ('disl.') and without dislocations (pristine). $\psi_{HF} = 0.99$ for all samples.

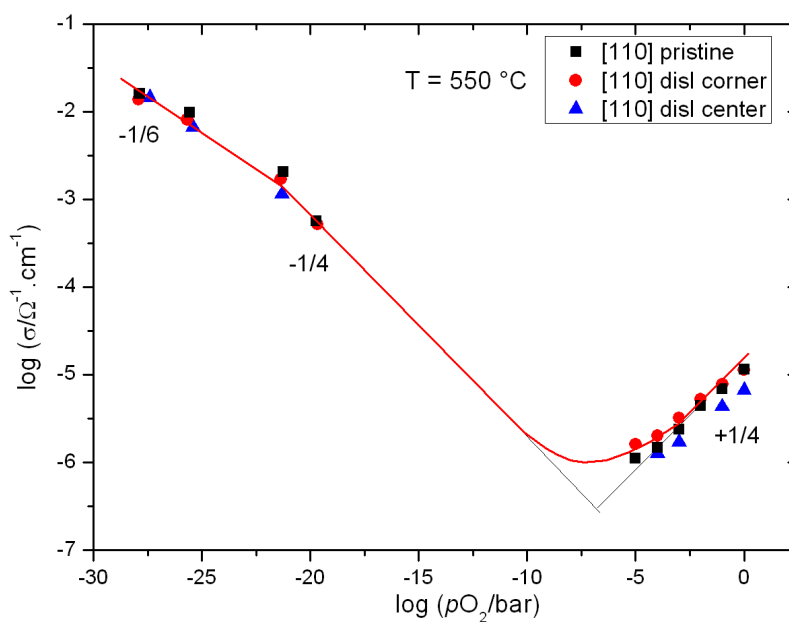


Figure 4.12: Electrical conductivity as a function of pO_2 for the [110] sample with ('disl.') and without dislocations (pristine). Center and corner indicates samples from different regions of the compressed sample

4. SINGLE CRYSTAL TiO_2

[110] samples did not show any changes in the conductivity despite the presence of dislocations as shown in Figure 4.5, 4.6, 4.7. Further, there is no significant change observed in the Arrhenius plots measured in 1 bar of oxygen as shown in Figure 4.13. Irrespective of the sample, the activation energy for conduction is close to 1.2 eV emphasizing no variation in the conductivity mechanism.

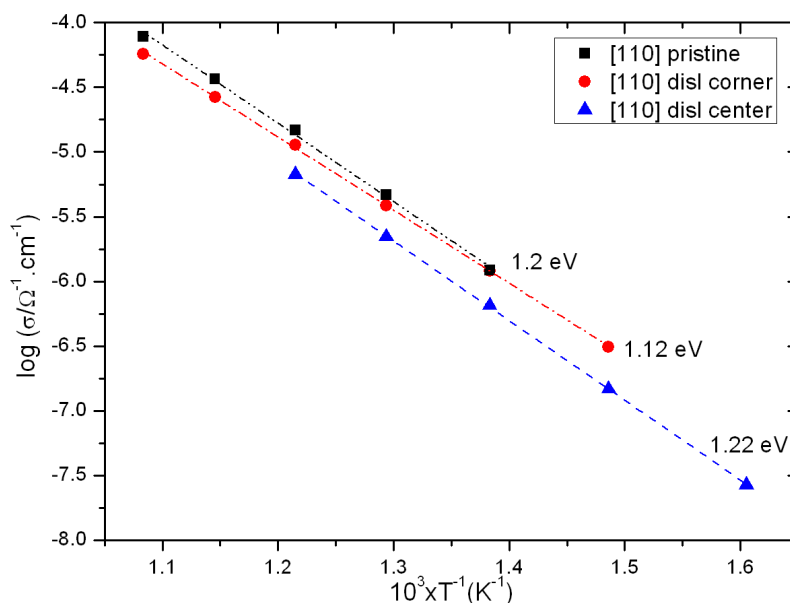


Figure 4.13: Electrical conductivity as a function of reciprocal temperature in 1 bar oxygen for [110] sample with ('disl.') and without dislocations (pristine). center and corner indicates the samples from different regions of the compressed sample

4.3 Partial conductivities in [001] crystals

From section 4.2.1, it is evident that the overall positively charged carrier conductivity has been enhanced up to 3 orders of magnitude in case of the 'center' sample. Since this sample shows the maximum effect, the partial conductivity by electron holes and ions are measured only on this sample, which from now on will be called as '[001]disl' for convenience. From the AC impedance measurement with symmetric Pt-paste electrodes it is not possible to quantify the electron and ionic conductivities. Instead, a Hebb-Wagner type setup is required to selectively block one of the charge carriers. This is achieved by depositing dense Au (200 nm) electrodes with

4.3 Partial conductivities in [001] crystals

Ti (20 nm) as the buffer and adhesion layer. The asymmetric cell arrangement is the following



With the above arrangement it is possible to block ions at the Au electrodes and extract only the hole conductivity from the DC signal when the steady state is achieved i.e. when only electronic carriers contribute to the current (see Figure 4.14). A reversal of cell polarity does not change the result. Figure 4.15 shows the partial conductivities of holes and ions in the [001] sample at high $p\text{O}_2$. Since the $p\text{O}_2$ -dependence of the electronic conductivity clearly indicates p-type behavior, Hebb-Wagner experiments with large voltages (which would yield σ_{ion} as a function of the modified effective $p\text{O}_2$ within in the sample) were not performed. It is evident that the majority contribution in the enhanced conductivity is by ions (approx. 3 orders) compared to holes (approx. by a factor 5). The calculated ionic transference number (ratio of ionic conductivity to total conductivity) is 0.94 to 0.99 as $p\text{O}_2$ varies from 1 bar to 10^5 bar respectively. These measurements shows that the formation of dislocations can potentially switch the conductivity from predominant electronic to ionic.

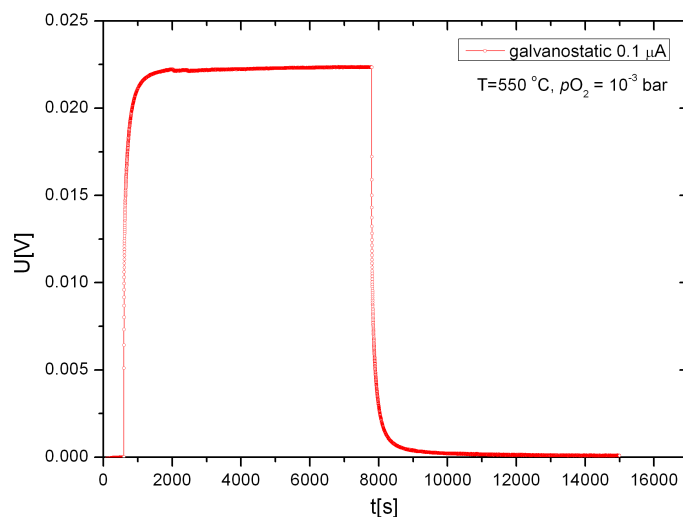


Figure 4.14: DC polarization curve for the [001] single crystal with dislocations.

4. SINGLE CRYSTAL TiO_2

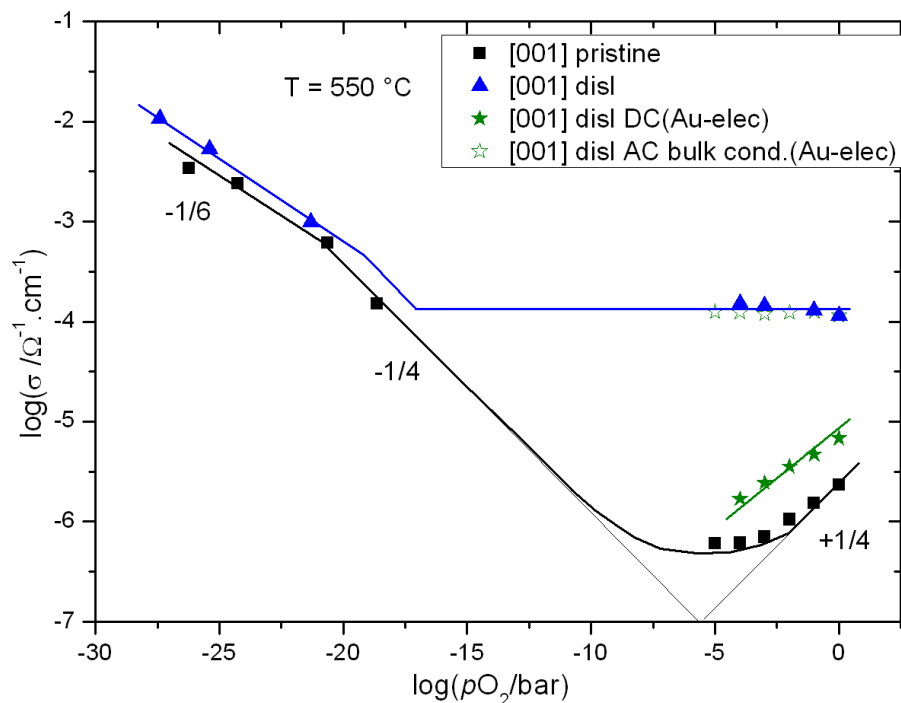


Figure 4.15: Electrical conductivity as a function of $p\text{O}_2$ for [001] sample with ('disl.') and without dislocations (pristine). Partial electron hole conductivity measured by Au electrodes represented as 'DC Au-elec' and total bulk conductivity is labelled as 'AC Pt-elec'.

4.4 Oxygen tracer experiments

Based on the Hebb-Wagner type polarization measurements on [001] crystals it is very convincing that the majority charge carriers are ions. The enhanced ionic conductivity could be either due to $\text{Ti}_i^{\bullet\bullet\bullet\bullet}$ or $\text{V}_\text{O}^{\bullet\bullet}$. Since both defects show the same $p\text{O}_2$ exponent (m) it is impossible to distinguish between them via conductivity vs. $p\text{O}_2$ plots (see Section 2.3). Tracer diffusion experiments which are sensitive to the specific sublattice defects (i.e., oxygen tracer for oxygen defects) are the best way to separate the individual contributions of these defects to the enhanced ionic conductivity. Figure 4.16 is a typical ^{18}O concentration profile from SIMS analysis for [001] crystals with and without dislocations (pristine) after isotope exchange at 800 °C and 0.5 bar $p\text{O}_2$ for 48 h. The profiles show two regimes, a very high diffusivity close to the surface (~ 200 nm) of the sample followed by the typical exponential decay of the ^{18}O concentration as the depth increases. The reason for

4.4 Oxygen tracer experiments

such box-type profiles close to the surface is most probably due to the polishing damage of the samples (similar profiles were observed e.g. for donor doped PZT with high D^* close to the surface [117]). Due to the spatially varying diffusivity, these profiles can not be solved for the semi-infinite case (derived for constant diffusion coefficient e.g. [118, 119]), but would require fitting the whole profile with variable D^* by finite differences or finite element methods.

Since the current interest is to know the difference in the tracer diffusivity due to

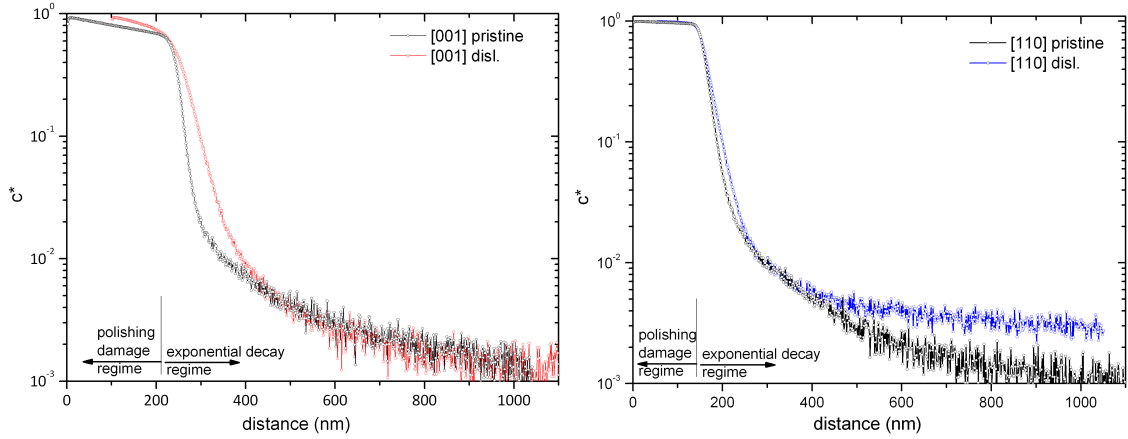


Figure 4.16: Normalized ^{18}O concentration profiles for [001] and [110] crystals (pristine and compressed) after isotope exchange at 800 °C for 48 h ($p\text{O}_2 = 0.5$ bar), the box-type profiles up to ~ 200 nm depth are due to the polishing damage.

dislocations rather than the absolute diffusion coefficient, as a first approximation the SIMS profiles are fitted only in the exponential decay regime (Figure 4.16) with the solution of the diffusion equation for a semi-infinite system according to Equation (4.2). (It is assumed that the effect of the high diffusivity close to the surface due to polishing damage is comparable for all the samples).

$$\begin{aligned}
 c^*(x, t) &= \frac{c(x, t) - c_{bg}}{c_g - c_{bg}} \\
 &= \operatorname{erfc} \left[\frac{x}{2\sqrt{D^*t}} \right] - \left[\exp \left(\frac{k_s^* x}{D^*} + \frac{k_s^{*2} t}{D^*} \right) \times \operatorname{erfc} \left(\frac{x}{2\sqrt{D^*t}} + k_s^* \sqrt{\frac{t}{D^*}} \right) \right]
 \end{aligned} \tag{4.2}$$

where $c(x, t)$ is the ^{18}O isotope fraction in the solid obtained from SIMS analysis,

4. SINGLE CRYSTAL TiO₂

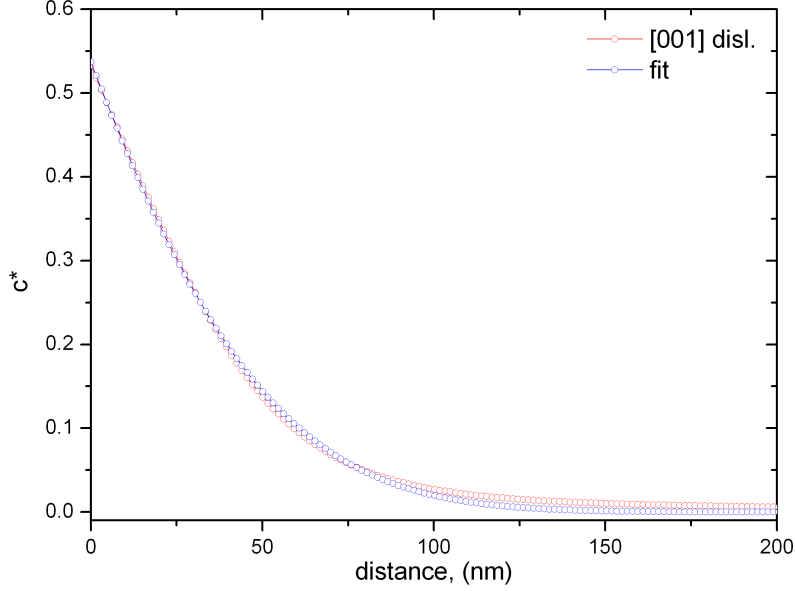


Figure 4.17:]

Normalized ¹⁸O concentration profile and fit result according to Equation (4.2) for [001] compressed crystal after isotope exchange at 800 °C for 48 h.

D^* is the apparent oxygen tracer diffusion coefficient*, k_s^* is the surface exchange coefficient†, t is the isotope anneal time, c_{bg} (0.2%) and c_g (95%) mean the background and enriched isotopic gas concentration in ¹⁶O and ¹⁸O gas respectively.

Figure 4.17 shows the fitting obtained by solving Eq. (4.2) for the [001] crystal with dislocations, isotope annealed at 800 °C for 48 h. The calculated tracer diffusivities at different isotope annealing temperatures are presented in Figure 4.18 for pristine and dislocation containing samples for both orientations. It is evident that the oxygen tracer diffusivity is enhanced by approximately 1 order of magnitude due to dislocations in the [001] crystals (Figure 4.18a). On the other hand, no significant variation is observed for tracer diffusivity in [110] crystals (Figure 4.18b), which is in agreement with the conductivity plots (Figures 4.12 and 4.13). The real values

* $D^* = \varphi_{sc}D_{sc}^{\parallel} + (1 - \varphi_{sc})D_b$ includes the contributions from the bulk (D_b) and space charge zones (D_{sc}^{\parallel}) and φ_{sc} is the respective volume fraction. In the present case lateral resolution of the SIMS measurement is not sufficient to differentiate these two regions. Since no variation in D_b is expected for compressed and pristine samples, changes in D^* are attributed to the diffusion along space charge zones.

†due to polishing damage close to the surface, the data is fitted only for exponential decay regime, therefore, k_s^* obtained in this fitting has no physical meaning

4.5 Discussion based on the space charge model

for tracer diffusion coefficient could slightly differ from the data in Figure 4.18. The activation energy for tracer diffusivity in pristine samples (2.5 ± 0.3 eV) and samples with dislocations (2.1 ± 0.2 eV) is in agreement with the available data in the literature, which is approx. 2.1 to 2.7 eV based on the impurity content [26, 120, 121].

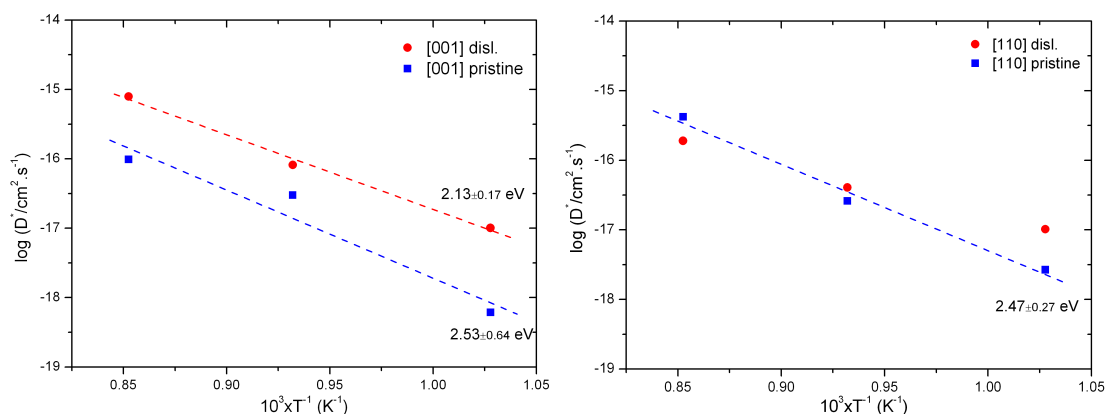


Figure 4.18: Bulk oxygen tracer diffusion coefficients obtained for (a) [001] crystals and (b) [110] crystals as a function of inverse temperature at 0.5 bar $p\text{O}_2$.

4.5 Discussion based on the space charge model

As described in the section 4.2.1, the enhanced ionic and hole conductivity at high $p\text{O}_2$ in the [001] sample is only possible by presence of negatively charged defects (this is essential to keep the crystal overall electroneutrality) most probably $V_{\text{Ti}}^{\prime\prime\prime}$. These excess negative charges in the dislocation cores will be compensated by adjacent space charge accumulation zones by positively charged defects such as h^\bullet , $V_{\text{O}}^{\bullet\bullet}$ and $\text{Ti}_i^{\bullet\bullet\bullet\bullet}$ (cf. section 2.5 Gouy-Chapmann situation). This is the key reason for the enhanced conductivity at high $p\text{O}_2$, as schematically shown in Figure 4.19. Since the charged defects in the dislocation cores are formed due to structural reasons, one can consider the excess charge density in the dislocation cores to be in good approximation independent of $p\text{O}_2$. This unaltered core charge reflects in a $p\text{O}_2$ independent majority charge carrier concentration ($V_{\text{O}}^{\bullet\bullet}$ and $\text{Ti}_i^{\bullet\bullet\bullet\bullet}$) in the space charge zone, as observed in Figure 4.15.

The Hebb-Wagner type polarization measurements (Figure 4.15) indicate the ac-

4. SINGLE CRYSTAL TiO_2

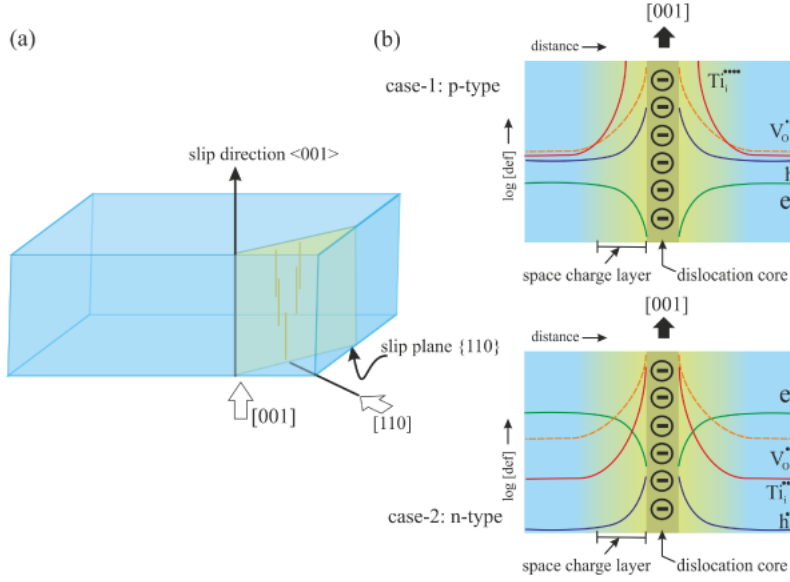


Figure 4.19: (a). Schematic representation of the slip system and measurement axis (only one plane is showed for better view). (b) A possible space charge model for p-type and n-type.

cumulation of holes adjacent to the negatively charged dislocations by a factor 5 (averaged over the whole sample) supports the Gouy-Chapmann situation. Based on the space charge arguments* this would result in an increase of factor 25 (i.e. 5^2) for $V_o^{\bullet\bullet}$ concentration (according to equation 2.19), due to their double charge. For mobile $\text{Ti}_i^{\bullet\bullet\bullet\bullet}$ [26, 77], an increase by factor 625 (i.e. 5^4) would be expected which corresponds to approx. 3 orders in the magnitude. All these values nicely match with the observed experimental results, i.e. $[V_o^{\bullet\bullet}]$ increased by approx. 1 order in magnitude (from the tracer experiments, see Section 4.4) and the total ionic conductivity by $\text{Ti}_i^{\bullet\bullet\bullet\bullet}$ increased by 3 orders in magnitude (Figure 4.15), and all support the assumption that space charge accumulation zones determine the conductivity. The whole situation is schematically described in Figure 4.19(b) case-I for p-type regime.

It is also worth noting that the dislocation cores are either extending throughout the crystal over the entire thickness, or a number of shorter dislocations must have overlapping space charge zones along the measurement axis. These two scenarios will lead to a percolating path which explains the enhanced conductivity in [001]

*i.e. assuming no changes in the defect mobilities

4.5 Discussion based on the space charge model

samples (in particular, also in the DC experiment). Based on the TEM analysis, (Figure 4.3, showing many dislocations that are closely spaced and also extending throughout the specimen thickness) and regarding these regions as representative of the samples for electrical measurement, the formation of percolating pathways appears to be very likely. This enhancement is therefore observed as long as the slip planes lie on the electrical measurement axis (scalar dot product between $\{110\}$ and $[001]$ is zero), which means that the dislocations are parallel to the measurement axis.

In case of the $[110]$ crystals, the electrical measurement axis is perpendicular to the slip planes (and space charge zones) and the influence of dislocations on the electrical conductivity will be negligible as long as the space charge zones do not overlap along the measurement axis. The condition for space charge zones to overlap is given by $2\lambda \geq d_{\text{dis}}$; where λ is the Debye length and d_{dis} is the distance between the dislocations. This situation is not possible in $[110]$ samples as the Debye length (approx. 3 nm* for approx. 100 ppm of impurities as indicated in table 3.1) is at least two orders lower than the estimated average distance between dislocations which is approx. 0.3 μm (see section 4.1.2).

At low $p\text{O}_2$, there are no changes observed in the conductivity. The negative core charge model is still valid and can also explain the reason for the unchanged conductivity. In the n-type regime (Figure 4.19(b)), the electron concentration is much higher in the bulk (region free of dislocations) than in the space charge zones and hence conduction through the bulk lattice is preferred over the space charge zones with electron depletion. Even though the $V_{\text{O}}^{\bullet\bullet}$ concentration is close to the electron concentration in the bulk ($n=2[V_{\text{O}}^{\bullet\bullet}]$), the mobility of electrons is much higher than that of the ions [26, 79], therefore the conductivity is still dominated by the electrons.

In case of the $[110]$ samples, neither at high nor low $p\text{O}_2$ such changes are observed as long as space charge zones do not overlap in the direction of the electrical measurement (leading to a percolating path with accumulated positive defects) or in the plane perpendicular to the current (leading to a depletion of negative carriers). In addition, the depletion zones in the samples extend to only about 1 % of the distance between the dislocations ($\lambda=3$ nm and $d_{\text{dis}}=0.3$ μm) which does not cover a significant volume compared to the highly conductive undisturbed bulk region.

*calculated based on eq. 2.22 at 550 °C

4. SINGLE CRYSTAL TiO_2

Hence in the n-type regime, no changes in the electrical conductivity is observed in any direction [001] or [110] with respect to the pristine crystals.

An alternative to the proposed model would be a model with a positive dislocation core charge due to $V_{\text{O}}^{\bullet\bullet}$ or $\text{Ti}_i^{\bullet\bullet\bullet\bullet}$ with adjacent negative space charge accumulation zones. Even though this model could explain the conductivity enhancement in the p-type regime - provided $V_{\text{O}}^{\bullet\bullet}$ or $\text{Ti}_i^{\bullet\bullet\bullet\bullet}$ are sufficiently mobile through the positive dislocation cores, - it fails to explain the unmodified conductivity in the n-type regime. In the n-type regime a positive dislocation core should lead to conductivity enhancement by electron accumulation in the space charge zones which is in contrast to the present observations. This further supports the argument of dislocations forming a negative core by $V_{\text{Ti}}^{\prime\prime\prime}$.

4.6 Conclusions on single crystals

In this chapter it is shown that 1-D line defects influence the ionic and electronic transport in single crystal TiO_2 . The effects are maximum at high $p\text{O}_2$ when the electrical measurement axis lies in the slip planes and no effects are observed when it is perpendicular. The enhanced electron hole and ionic conductivity is consistently interpreted in the framework of an excess negative dislocation core charge due to $V_{\text{Ti}}^{\prime\prime\prime}$ and adjacent space charge accumulation zones. The proposed model is able to explain the experimental observations including the systematic increase in ionic conductivity at high $p\text{O}_2$ and the unchanged electron conductivity at low $p\text{O}_2$.

5

Polycrystalline TiO₂

Chapter 4 highlighted the influence of dislocations in TiO₂ single crystals, the key finding was that the dislocations enhance the conductivity only in [001] direction i.e., along the slip planes with no changes perpendicular to the slip plane. In this chapter, the focus will be on polycrystalline TiO₂ samples which are more relevant for various technological applications. Since polycrystalline materials consist of grains with random orientation, the shear stress required to initiate slip will be different for each grain based on its orientation relative to the compression axis. Therefore, as a first approximation, one might already assume that the results on polycrystalline materials represent an averaged effect of dislocations.

The influence of dislocations on the electrical properties of polycrystalline TiO₂ was studied by preparing TiO₂ ceramics with and without dislocations. In order to generate dislocations, TiO₂ powders were sintered under uniaxial pressure in a spark plasma sintering machine (SPS samples). Due to the high pressure (400 MPa) and temperature (1000 °C), sintering of TiO₂ particles occurred along with dislocation generation (due to creep deformation) as indicated in the deformation mechanism map (Figure 3.4). In contrast, samples without dislocations were prepared by pressureless conventional sintering after cold isostatic compression of TiO₂ powder (CS sample). Experimental details for both samples are described in section (3.3). SEM images of the CS and SPS samples are shown in Figure 5.1.

5. POLYCRYSTALLINE TiO₂

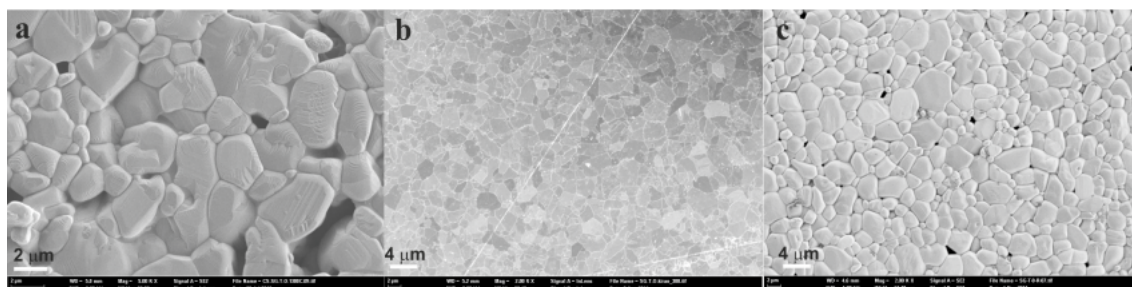


Figure 5.1: SEM images of (a) conventionally sintered (CS) sample sintered at 1300 °C for 5 h in air, (b) spark plasma sintered sample (SPS) annealed for 1000 °C for 1 h in air and (c) SPS sample after recovery treatment at 1300 °C for 5 h in air, all samples were mechanically polished and thermally etched at 1000 °C for 30 min.

5.1 Defect characterization

Dislocations in polycrystalline TiO₂ ceramics were characterized by Philips CM 200 TEM. Figure 5.2(a-c) shows three representative images of the sample, Figures 5.2a and b indicate dislocations within a large grain with beam axis parallel to [111] direction. A high contrast for dislocations was achieved by using a two beam condition with $\mathbf{g} = 110$ (Figure 5.2b) indicating the slip planes of TiO₂ to be on {110} and {101}, which is in agreement with the literature [39–41, 104]. Figure 5.2c is taken from the same specimen from a region with smaller grains which are free of dislocations. This clearly indicates that the mode of creep deformation is a function of grain size (see section 5.3.1, the smaller the grain size, the larger the stress required to generate dislocations in the grain interior). Throughout the sample, cube shaped features were observed in the large grains (Figure 5.2a and d). There is no differences observed either in energy dispersive x-ray analysis (EDAX) or in SAD, i.e., no change in the crystal composition or structure. So, the only option left for such contrast is varying thickness. Figure 5.2d shows the thickness map generated by a Zeiss 912 Omega microscope within a large grain indicating the contrast is due to decreased effective thickness of the sample. A probable reason could be due to accumulation of vacancies by moving dislocations in the dislocation creep regime [122].

TEM characterization was not performed on the CS sample, as there is no possibility to generate high density of dislocations without high temperature deformation. The

possibility of dislocation formation during TEM preparation technique was ruled out, as it was already shown in Chapter 4 that no artifacts were found on pristine TiO_2 single crystals Figure 4.1.

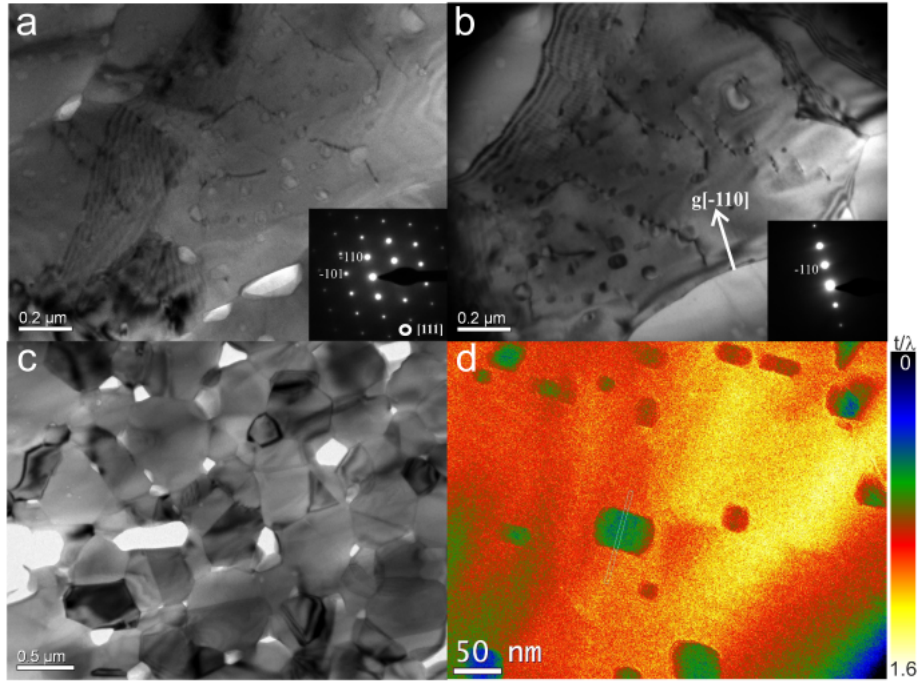


Figure 5.2: Bright field TEM images of the SPS sample annealed at 1000 °C for 1 h, (a) beam axis parallel to $[111]$ pole, (b) two beam condition with $\mathbf{g} = (-110)$, (c) view of small grains with out any dislocations and (d) thickness map within a large grain, the square features correspond to the coalescence of vacancies (t =sample thickness, λ = inelastic mean free path).

5.2 Electrical characterization

5.2.1 Conventionally sintered samples

Figure 5.3 presents the impedance spectrum for the CS sample measured at 550 °C in pure oxygen. Two distinct semicircles were observed at high and low frequencies indicating two physical processes in the system. The high frequency semicircle is attributed to the bulk contribution based on the permittivity value ($\epsilon_r=80$) as calculated from Equation (3.3) based on the measured capacitance (10^{-11} F). The

5. POLYCRYSTALLINE TiO₂

low frequency semicircle has a low capacitance value (10^{-10} F) compared to a typical grain boundary capacitance (around 10^{-9} F). Since the samples suffer from high porosity (up to 30 %), it is expected to have such a low capacitance due to current constriction at the grain boundaries. The depression of the low frequency semicircle also supports this interpretation.

The bulk and GB conductivities are calculated based on the sample geometry*

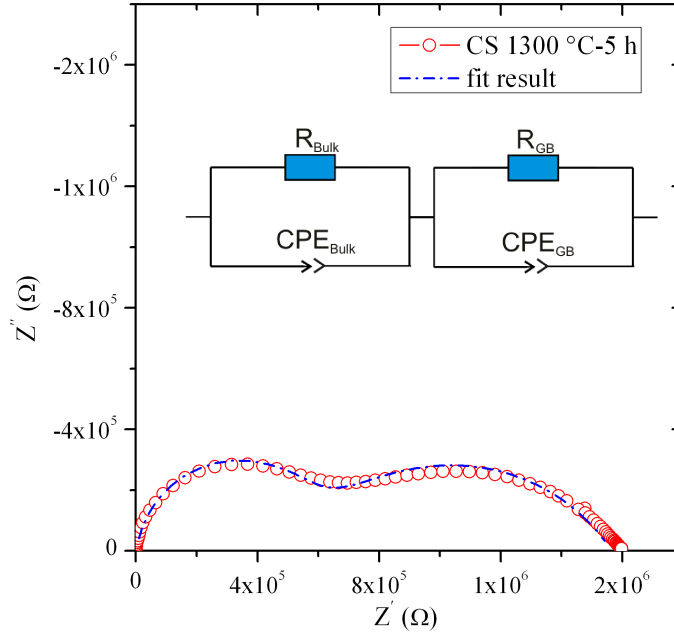


Figure 5.3: Impedance spectrum measured at 550 ° C in 1 bar pO_2 for the CS sample sintered at 1300 ° C for 5 h in air, inset shows the equivalent circuit used for fitting the data with $\psi_{HF}=0.95$, $\psi_{LF}=0.6$

according to Equations (3.1) and (3.2) and plotted versus pO_2 in Figure 5.4. Since the CS samples have a very low density (~ 70 %), the bulk and GB conductivity was corrected for porosity based on the Maxwell dilute limit equation [123], which can be described as

$$R_{corr}^i = R_{meas}^i \left(1 - \frac{3}{2}f \right) \quad (5.1)$$

R_{corr} and R_{meas} mean the corrected and measured value of the resistance respectively, i refers to the arc (bulk or GB) and f represents the volume fraction of pores.

*The specific GB boundary conductivity (Equation 3.5) would be lower by almost 2 orders of magnitude

This ignores the current constriction, which is naturally present at these high porosity values leading to a further substantial resistance increase at low frequencies. As discussed in the literature for pure bulk effects such correction factors do not change on temperature or pO_2 as long as the morphology does not change.

The electrical properties of the polycrystalline CS sample are similar to the TiO_2 single crystal shown in Figure 4.9 i.e., p-type semiconductor at high pO_2 and n-type semiconductor at low pO_2 . The pO_2 exponents of +1/4, -1/4 and -1/6 at the various pO_2 regimes are in agreement with the bulk defect chemistry of TiO_2 (Section 2.3) and other earlier findings in literature [3,37,73]. The pO_2 exponent for the GB conductivity is the same as for the bulk conductivity (+1/4) indicating the majority charge carriers to be electron holes in the bulk as well as at GB's. The activation energy for conduction of electron holes in 1 bar of oxygen is 0.9 eV and 1.24 eV for the bulk and GB respectively, as plotted in Figure 5.5. The bulk conductivity data perfectly match with the single crystal data (along c-axis) indicating the same conduction mechanism due to electron holes. The difference between the bulk and GB activation energy suggests that the low frequency semicircle in Figure 5.3 is not solely due to current constriction* but results from the combined effect from blocking GB's due to space charge depletion and current constriction. The finding of the same pO_2 dependence for bulk and GB means that the GB space charge potential must essentially be pO_2 -independent. Indeed, only minor pO_2 -dependences were observed, e.g. for the space charge potential of $SrTiO_3$ [124].

5.2.2 Spark plasma sintered samples

The SPS samples are very dense (95 %) in comparison to the CS samples, therefore current constriction effects can be ruled out. Figure 5.6 presents the impedance spectrum of the SPS sample with dislocations. It is obvious that there is only one physical process occurring in the system. Based on the measured capacitance, the calculated permittivity ($\epsilon_r=110$) is within the range of bulk permittivity values for TiO_2 . The impedance spectrum was fitted with the equivalent circuit shown as an inset in Figure 5.6, and the conductivity values were calculated based on Equation 3.1. The conductivity values are plotted as a function of pO_2 in Figure 5.4 named

*pure bulk current constriction will always lead to same pO_2 exponent and activation energy.

5. POLYCRYSTALLINE TiO_2

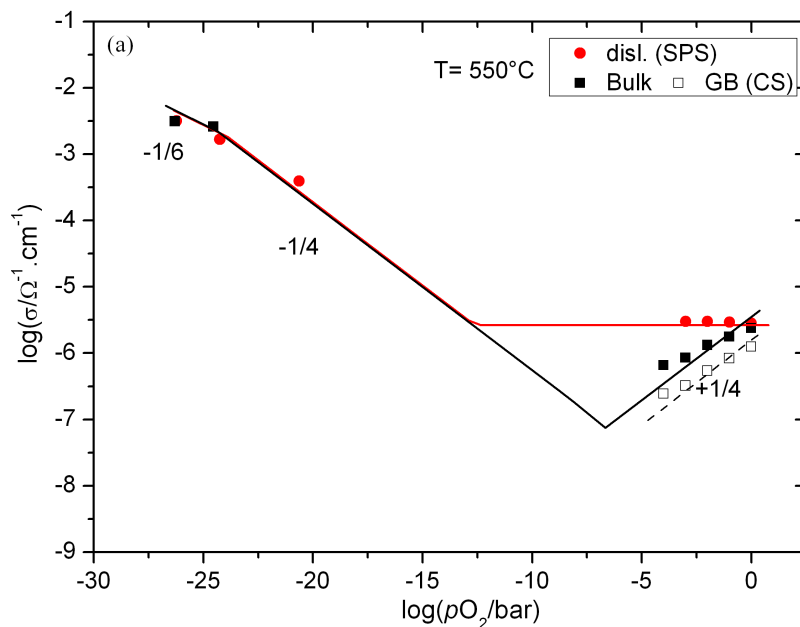


Figure 5.4: Total electrical conductivity as a function of $p\text{O}_2$ for the SPS sample (with dislocations) and the CS sample (without dislocations). The slopes in the low $p\text{O}_2$ -regime are drawn according to the values expected from the bulk defect model.

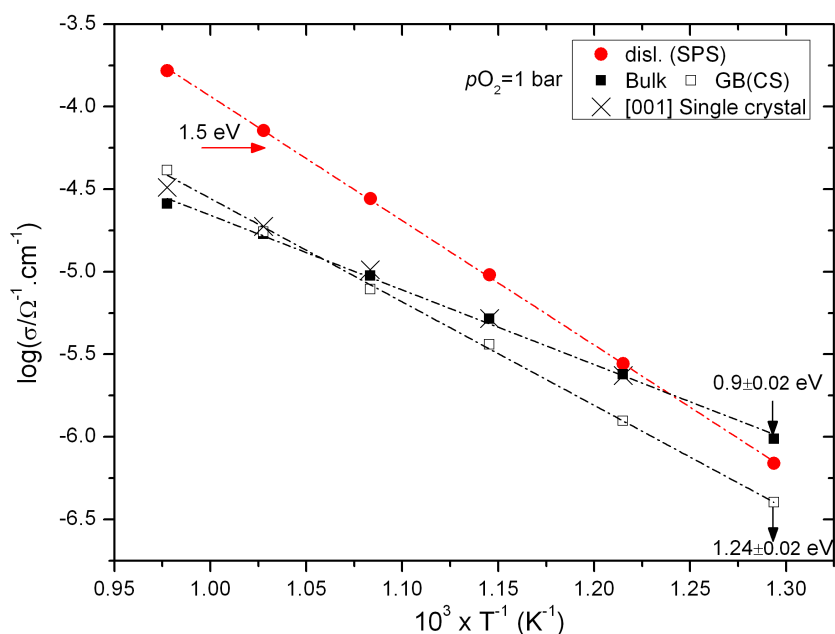


Figure 5.5: Arrhenius plot for the SPS sample (with dislocations) and the CS sample (without dislocations)

'disl.' (SPS). It is very evident from the plot that at high pO_2 the conductivity is independent of oxygen partial pressure indicating predominant ionic conductivity in the sample. These modified electrical properties compared to the CS sample are solely attributed to the dislocations in the SPS sample since both samples are prepared from the same powder, i.e. have the same impurity or acceptor content. Based on the experimental conditions during sintering, there is no contamination of the samples by any kind of acceptor impurities.

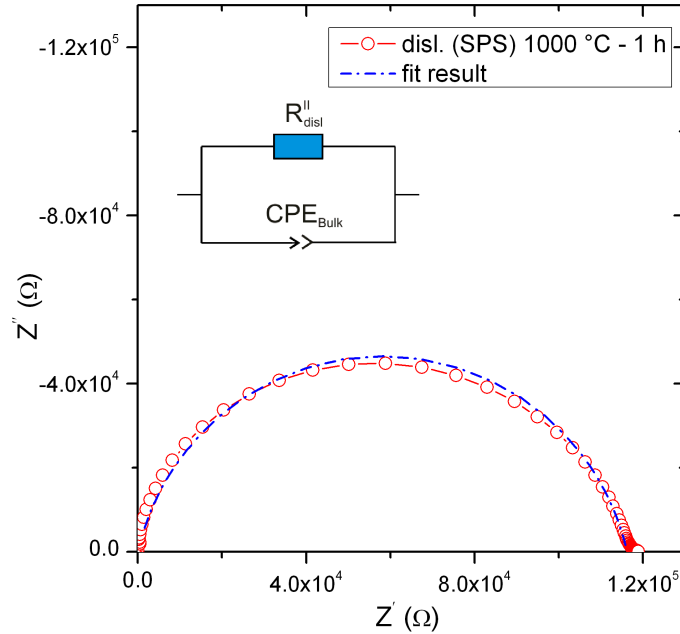


Figure 5.6: Impedance spectrum measured at 550 ° C in 1 bar pO_2 for the SPS sample, inset shows the equivalent circuit used for fitting the data with $\psi_{HF}=0.9$.

In consideration of the electrical conductivity data in Figure 5.4, a careful interpretation is needed to assign the observed modified conductivity either to the bulk or enhanced conductivity along GB's (nano size effect) as both pathways lead to a single semicircle with a bulk capacitance value in the impedance spectra as illustrated in Figure 2.10 (see ref. [13]). The latter effect does not fit for the present sample, as the grains in the SPS sample are of micron size (Figures 5.2, 3.3). On the other hand, this can also not be the bulk conductivity of the sample as this should lead to p-type conductivity as shown by the CS sample. So the only possible pathway that

5. POLYCRYSTALLINE TiO₂

can explain the observed single physical process in the impedance spectra (Figure 5.6) and the increased ionic conductivity (Figure 5.4) is by enhanced conduction parallel to the line-defects in the sample, very similar to what is observed in the [001] rutile single crystals (Chapter 4). The fact that the ionic conductivity of the SPS sample is enhanced implies that a percolating network of dislocations is formed throughout the sample, i.e. they are well connected even at the GB's. The activation energy for conduction along the line defects is ~ 1.5 eV (Figure 5.5), which is higher than for the CS sample. While an increase can be expected due to the change from hole (migration barrier 0.4 eV [3]) to ionic defects as regards the dominant species (migration barrier for $V_O^{\bullet\bullet}$ and $Ti_i^{\bullet\bullet\bullet}$ is 0.8 and 0.7 eV respectively [26, 77]), the absolute value is not fully understood yet. A slightly different dislocation network in polycrystalline TiO₂ with GB's in comparison to continuous dislocation network in single crystals could be a reason.

5.2.3 Stoichiometric polarization measurements

Since the measured conductivity in Figure 5.4 is the total conductivity of the SPS sample (including both electronic and ionic parts), the partial ionic conductivity was extracted by stoichiometric polarization measurements [99, 100] as described in section 3.4.4. A thin layer of YSZ film serves as the electron blocking electrode in the cell configuration of Pt-paste/YSZ/TiO₂ pellet/YSZ/Pt-paste.

A Keithley 236 source measure unit (DC characterization) was used generating currents between 1 μ A or 1 nA. Such small currents are necessary to keep the voltage across the sample below 0.1 V. Possible contributions of the electrode or YSZ/TiO₂ interface resistance were investigated by impedance spectroscopy.

Figure 5.7 presents the partial ionic conductivity of the SPS sample compared with the sample with Pt-paste electrodes. It is very evident that at high pO_2 i.e., from 1 bar to 10^{-3} bar, the sample is predominantly an ionic conductor with a transference number of ~ 0.7 which is unexpectedly high for a nominally undoped TiO₂ sample [3]. Based on the history of the sample, it is convincing that the observed increase in ionic conductivity is not due to any acceptor dopants (extrinsic compensation) but caused by the creation of dislocations (intrinsic compensation). The activation energy for the partial ionic conduction in the SPS sample (Figure 5.8) is close to that

5.2 Electrical characterization

of the total conductivity measured with Pt-paste electrodes (Figure 5.5)* indicating no change in the charge carriers, and also supporting the observed increase in ionic transference number.

To compare the enhanced ionic conductivity due to dislocations with the effects of conventional chemical doping, the equivalent acceptor dopant concentration that is required to see such an ionic conductivity is estimated by the Nernst-Einstein equation

$$D_i = \frac{\sigma_i RT}{z_i^2 F^2 c_i} \quad (5.2)$$

Here, D_i is the defect diffusivity of species i - which is $\sim 1.8 \times 10^{-13} \text{ m}^2/\text{s}$ at 550°C for $\text{V}_{\text{O}}^{\bullet\bullet}$ according to ref [26], σ_i is the conductivity of species i (in this case conductivity due to $\text{V}_{\text{O}}^{\bullet\bullet}$ as obtained from Figure 5.7), R is the gas constant, T is the temperature, z_i is the charge of the diffusing species (2 for $\text{V}_{\text{O}}^{\bullet\bullet}$), F is the Faraday constant and c_i is the concentration of the defect i in mol/m^3 . Inserting the respective values yields an oxygen vacancy concentration of $132.7 \text{ mol}/\text{m}^3$, which is equivalent to a trivalent acceptor dopant concentration of approx. 0.5 mol%. Similarly, the lower limit for the acceptor dopant can be estimated on considering only $\text{Ti}_i^{\bullet\bullet\bullet}$ as the majority defect and this results in an acceptor concentration of 0.02 mol% of trivalent acceptor dopants.

In case of homogeneous doping, the solubility of the dopant depends on the ionic radius relative to that of Ti^{4+} ($r = 0.74 \text{ \AA}$), and it is only 0.1 mol% for Y^{3+} ($r = 0.9 \text{ \AA}$) [4] and 1 mol% for Al^{3+} ($r = 0.54 \text{ \AA}$) and Ga^{3+} ($r = 0.62 \text{ \AA}$) [2, 3]. A very high concentration of acceptor dopants is thus necessary to achieve an ionic plateau in TiO_2 , which is not achievable possible due to the limited solubility of the dopants. An increase in acceptor dopant concentration would not only increase the ionic conductivity but also the p-type electronic conductivity [2, 3, 73], as explained in the defect chemistry section 2.3. However, with dislocations, the ionic conductivity prevails over an extended $p\text{O}_2$ range, due to space charge accumulation zones (as explained in the section 5.3) that results in a flat ionic plateau.

*activation energy in both samples differ by $\sim 0.2 \text{ eV}$ which could arise from individual sample preparation.

5. POLYCRYSTALLINE TiO_2

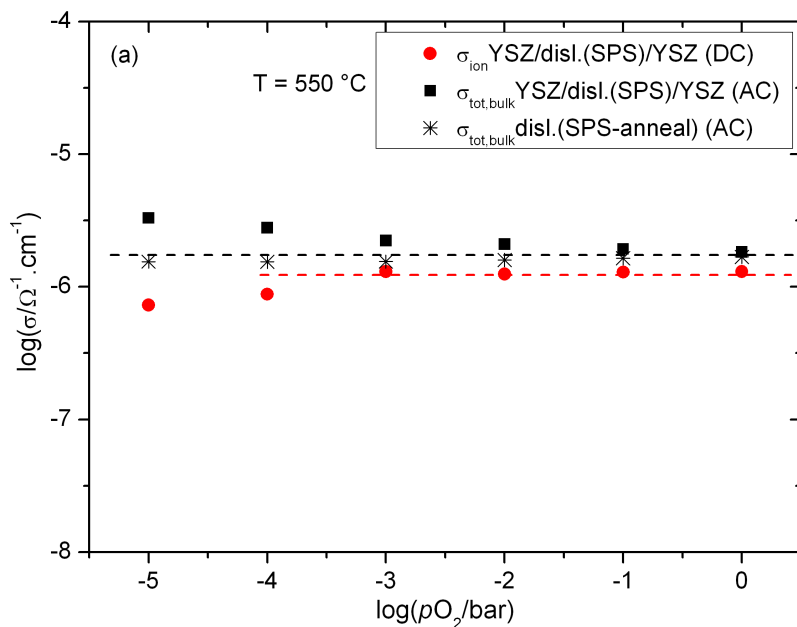


Figure 5.7: Partial ionic conductivity as a function of $p\text{O}_2$ for the SPS sample with dislocations, compared to the total conductivity.

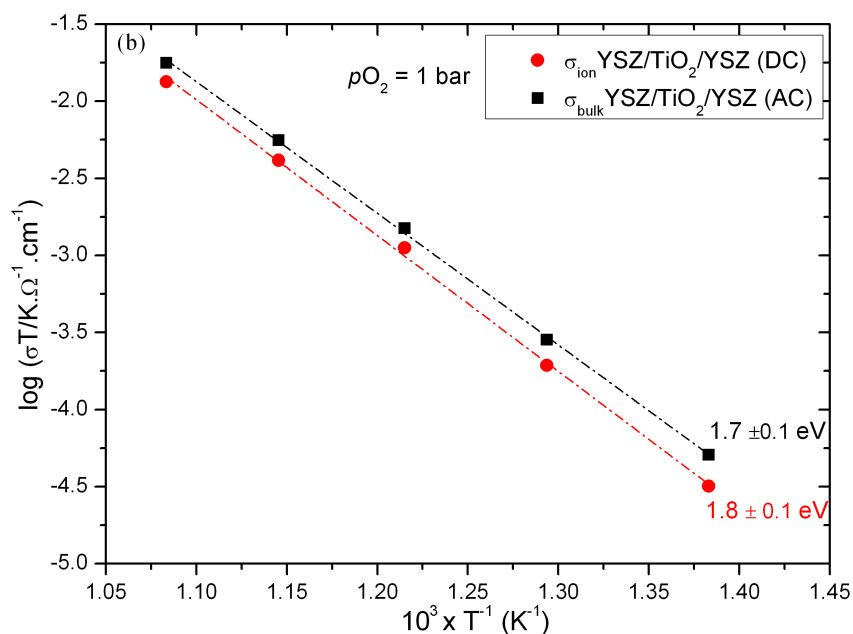


Figure 5.8: Arrhenius plot for the total and partial ionic conductivity of the SPS sample with dislocations.

5.2.4 Stability of dislocations

To investigate the persistence of dislocations, a SPS sample with dislocations was annealed at 1300 °C for 5 h in air similar to the CS sintering conditions. In general, such a high temperature ($0.7 \times$ melting point) favors dislocation migration to the surface or interface and after sufficient time leads to their annihilation. After annealing, the SPS sample is characterized by impedance spectroscopy. Figure 5.9 shows a second semicircle at low frequencies compared with the SPS sample without annealing (Figure 5.6). The measured capacitance of $\sim 10^{-9}$ F corresponds to an apparent relative permittivity (ϵ_r) of $\sim 40,000$, as calculated according to Equation (3.4). Based on this apparent permittivity value, the low frequency semicircle can be assigned to blocking behavior of the GB corresponding to a thickness of 26 nm. The equivalent circuit for this physical model is shown as inset in the Figure 5.9 and the extracted conductivity values are plotted as a function of pO_2 and temperature in Figure 5.10 (labeled as 'SPS-anneal'). Comparing the high frequency data with the SPS sample without annealing indicates only a slight decrease in the conductivity and activation energy, which confirms the persistence of most of the dislocations in the sample.

According to the earlier findings [106, 125] on dislocation annihilation studies in TiO_2 , the activation energy for recovery (dislocation annihilation) at zero applied stress (pressureless annealing) is double the activation energy required for creep. Therefore, it is possible to achieve complete annihilation of dislocations only at higher temperatures (greater than $0.7 \times$ melting point) i.e. approaching typical sintering conditions and prolonged annealing times (see [106] for details). So, it is not surprising that the samples largely retain the modified conductivity even after a high temperature anneal.

5.2.5 Spark plasma sintering sample without dislocations

To confirm that the present effect of enhanced ionic conductivity in the SPS sample (Figure 5.4) is only due to the dislocations but not an artifact caused by the sintering technique, another SPS sample was prepared at a lower temperature (850 °C) and pressure (40 MPa) to avoid deformation by dislocation creep instead activating creep deformation via the diffusion mode, see the deformation mechanism map for

5. POLYCRYSTALLINE TiO₂

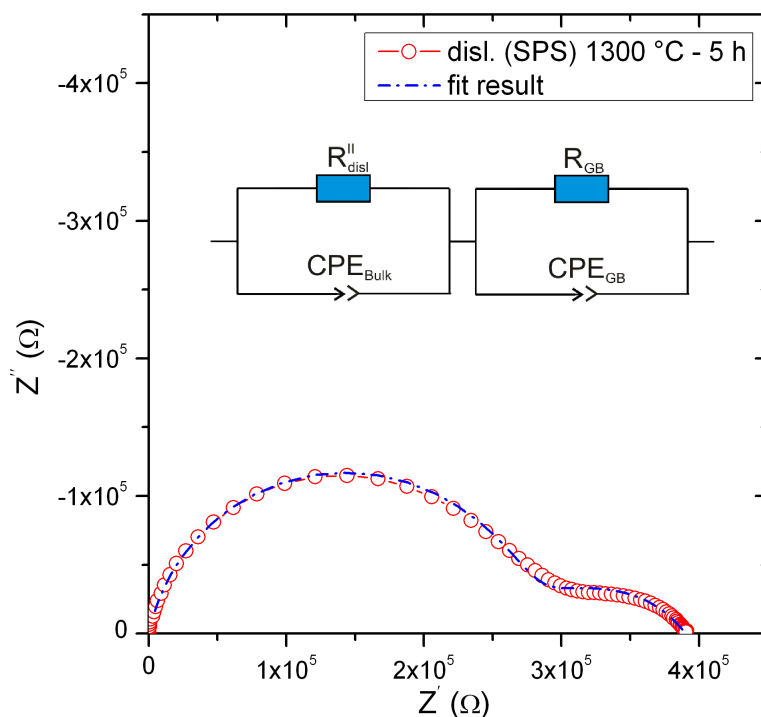


Figure 5.9: Impedance spectrum measured at 550 ° C in 1 bar $p\text{O}_2$ for the SPS sample after annealing at 1300 ° C for 5 h, inset shows the equivalent circuit used for fitting the data with $\psi_{HF}=0.9$ and $\psi_{LF}=0.6$.

optimum conditions (Figure 3.4). The density of the sample was lower (80 %) than the SPS sample sintered at high pressure (95 %). Figure 5.11 shows the impedance spectrum of the SPS sample without dislocations, the plot also gives the fit result obtained by considering a equivalent circuit that consists of two physical processes from the bulk and GB. The bulk conductivity for the SPS sample without dislocations ('SPS-nodisl') is plotted as a function of $p\text{O}_2$ in Figure 5.12 and compared with the CS sample. The high frequency data (bulk conductivity) matches perfectly at high $p\text{O}_2$ (1 bar to 10^{-5} bar) for both the samples with a positive slope of $+1/4$ confirming hole conductivity. This shows that the observed enhanced conductivity at high $p\text{O}_2$ in SPS samples prepared at high pressure (400 MPa) and temperature (925 ° C) is solely due to the dislocation creation in TiO₂ polycrystalline samples.

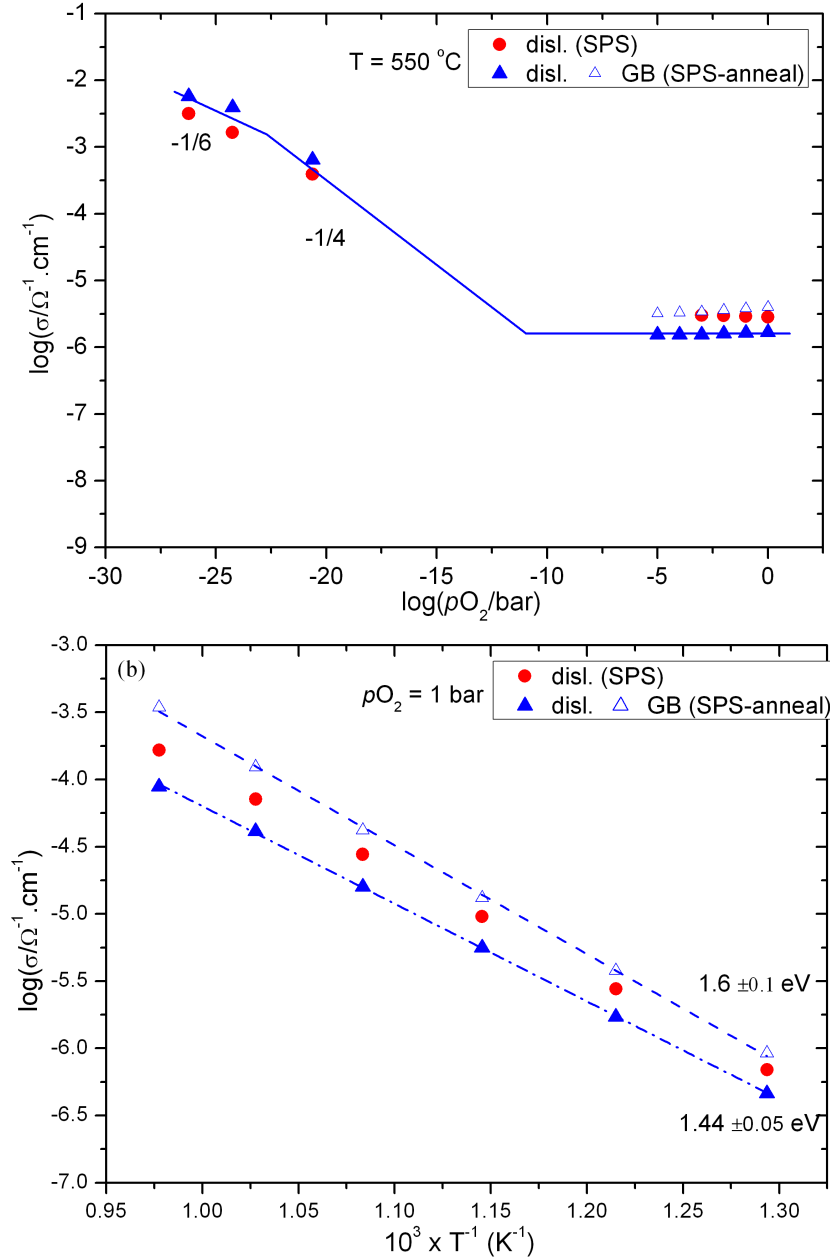


Figure 5.10: (a) Total electrical conductivity as a function of $p\text{O}_2$ for the SPS sample with dislocations before ('disl-SPS') and after annealing at $1300\text{ }^\circ\text{C}$ for 5 h ('SPS-anneal'). (b) Arrhenius plot for the same samples in 1 bar oxygen. The slopes in the low- $p\text{O}_2$ regime are drawn according to the values expected from the bulk defect chemical model.

5. POLYCRYSTALLINE TiO_2

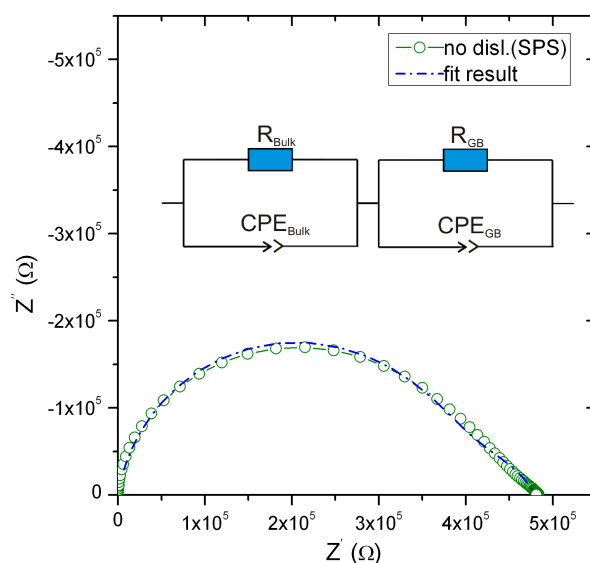


Figure 5.11: Impedance spectrum measured at 550°C in 1 bar $p\text{O}_2$ for the SPS sample without dislocations, obtained by compression at 40 MPa and 850°C for 15 min, inset shows the equivalent circuit used for fitting the data with $\psi_{HF}=0.91$ and $\psi_{LF}=0.68$.

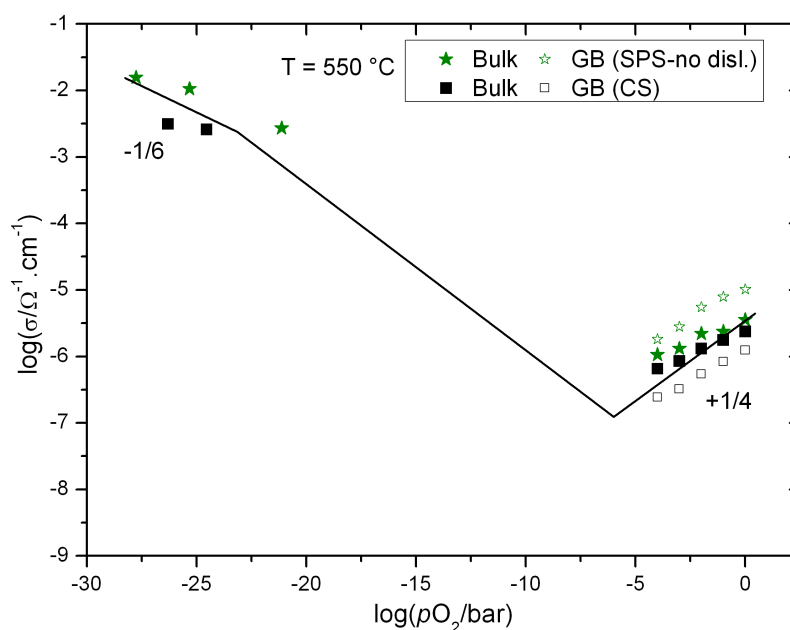


Figure 5.12: Total electrical conductivity as a function of $p\text{O}_2$ for the SPS sample with negligible dislocations, pressed at 40 MPa, 850°C for 10 min and the CS sample (without dislocations) for comparison. The slopes in the low- $p\text{O}_2$ regime are drawn according to the values expected from the bulk defect chemical model.

5.3 Discussion

5.3.1 Grain size dependence of deformation mechanism maps

As described in the section 3.5.1, a deformation mechanism map provides information about the mode of material transport (creep mechanism) at given temperature and pressure. The creep deformation modes also depend on the strain rate and grain size. Figure 5.13 depicts this effect for two grain sizes viz. 100 nm and 1 μm . As grain size decreases, the dislocation creep field shrinks (towards higher temperatures) and also shifts to higher pressures. The temperature and pressure applied for the two SPS samples ('SPS-disl' and 'SPS-no disl') marked in both plots show that 'SPS-no disl' sample always lie in the diffusion creep regime (either in Coble or Nabarro-Herring creep) which does not lead to dislocation creation. Hence, the conductivity of the SPS sample without dislocations will be close to the bulk conductivity of the CS sample as shown in the Figure 5.12.

In case of the SPS sample with dislocations, the experimental conditions 925 $^{\circ}\text{C}$ and 400 MPa fall under the dislocation creep regime when the grain size is 1 μm and fall in the diffusion creep regime for smaller grains (<100 nm). As described in Section 3.3.2 and SEM image shown in Figure 5.1a, the SPS sample has a bimodal distribution of grain size with smaller and larger grains. When the grains are larger (over 1 μm), dislocation creep is activated to generate dislocations (Figure 5.2a,b) and for smaller grains (below 100 nm) no dislocations will be observed (Figure 5.2c).

5.3.2 Space charge model

The modified electrical properties of TiO_2 through the presence of dislocations can be explained in the framework of the space charge model. The key result of this chapter is Figure 5.4, which shows the modification of electrical properties from the typical hole conductivity to predominant ionic conductivity at high $p\text{O}_2$ due to introduction of dislocations. As already explained in Section 4.5, the increase in positively charged carrier concentration in the system (evidenced by ionic conductivity due to $\text{V}_{\text{O}}^{\bullet\bullet}$ and $\text{Ti}_i^{\bullet\bullet\bullet}$) has to be balanced by negatively charged defects in the system i.e., by $\text{V}_{\text{Ti}}^{\bullet\bullet\bullet}$ in the dislocation cores. The complete picture can be described

5. POLYCRYSTALLINE TiO₂

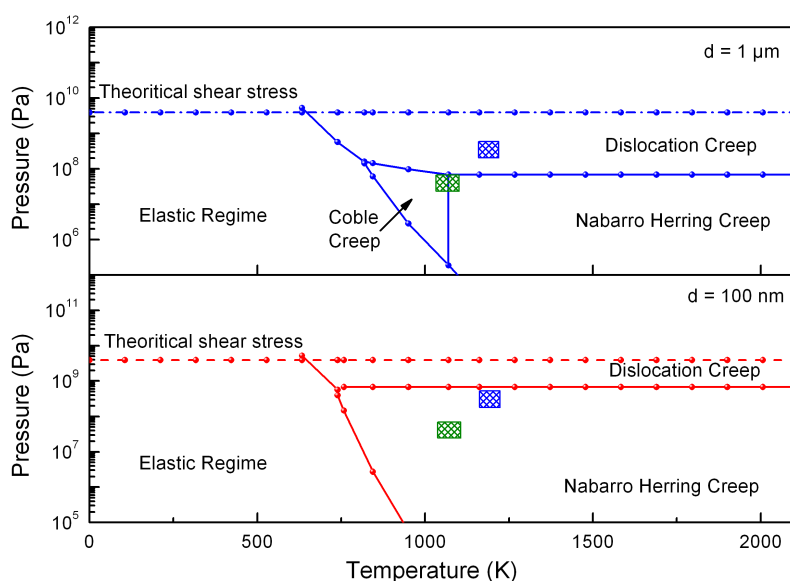


Figure 5.13: Deformation mechanism map for TiO₂, constructed based on the data available from [109], for the grain size (a) 1 μm and (b) 100 nm at a strain rate of $10^{-8}/\text{s}$. The shaded boxes indicate the parameters for SPS samples (blue ~ 400 MPa, green ~ 40 MPa).

as accumulation of positive charge carriers in space charge zones adjacent to negatively charged dislocation cores (Figure 4.19). Since the defect screening strength in the space charge zone depends on the charge of the defect (z_i in Equation (2.19)), the ionic defect concentration steeply rise over that of electronic defects in the space charge zone leading to a predominant ionic conduction (Figure 5.4). Further the single semicircle in the impedance spectrum shown in Figure 5.6 indicates that the dislocations or the accumulation zones form a continuous network throughout the sample, as schematically illustrated in Figure 5.14b. By annealing at high temperature (1300 $^{\circ}\text{C}$) for prolonged time (5 h) the grain size increased at least by a factor of two resulting also in interruption of the dislocation network at the grain boundaries as schematically illustrated in Figure 5.14c. This most probably is the reason for observing an additional semicircle at low frequency in the impedance spectrum (Figure 5.9). However, an important observation is that this extended annealing treatment did not completely annihilate dislocations, this shows that they are very persistent. Figure 5.15 shows an earlier finding [106] on the effect of annealing on dislocation structure of a creep deformed TiO₂ single crystal. Bell et. al found that

annealing lead to a sub-boundary formation (dislocation walls) with an increase in the dislocation spacing. According to their work, the complete annihilation of dislocations is possible only under an applied stress, where the sub-boundaries can be migrated to the surface, ref. [106].

At very low pO_2 , in the n-type regime no changes can be observed as the long as

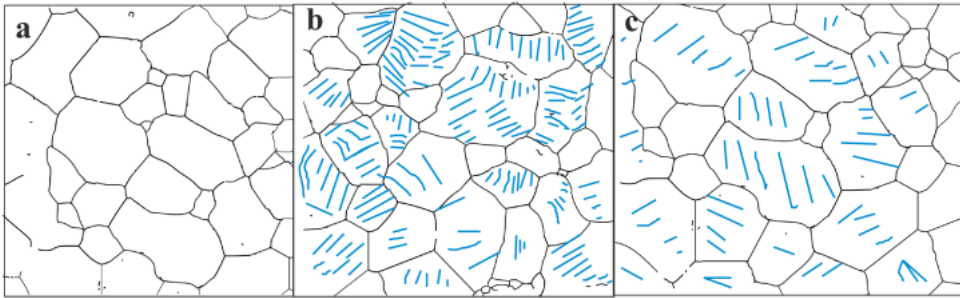


Figure 5.14: Schematic microstructural features as expected from observed impedance spectra and conductivity data for (a) conventionally sintered (CS) sample (b) spark plasma sintered sample (SPS-disl) with dislocations, (c) SPS sample after long annealing treatment (SPS-anneal) at 1300 °C for 5 h, blue lines indicate dislocations.

dislocations are well separated (as explained in the previous chapter, section 4.5). The high concentration of electrons in the sample lead to inductive loops in the impedance spectra without any well separated features for the CS and SPS samples. Hence, in the n-type regime no conclusions can be drawn based on conductivity results that corresponds to the bulk or GB.

Another alternative explanation for the observed increase in the conductivity at high pO_2 could be due to strain induced increased ion mobility in the vicinity of the dislocations. However, in such situations typically a lower activation energy is expected [25]. This is in contradiction to the results which show a rather high activation energy of approximately 1.5 eV (Figure 5.5). So it is to be assumed that the observed effects are mainly caused by space charge accumulation zones rather than by strain effects.

5. POLYCRYSTALLINE TiO₂

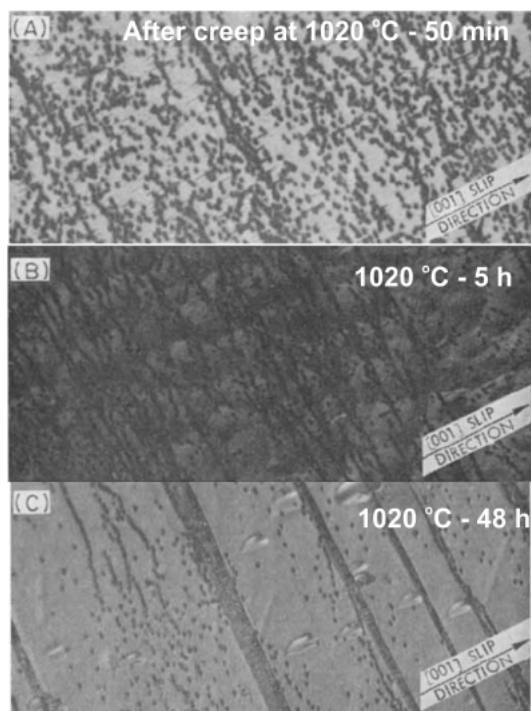


Figure 5.15: Dislocation structure configuration on (110) faces of rutile creep specimens by etch-pit technique (A) without annealing treatment (B) Annealing for 50 min and (C) annealing for 48 h at 1020 °C. Images reprinted from ref. [106].

5.4 Conclusions on polycrystalline TiO₂

Finally, comparing the results of this chapter on polycrystals with the previous chapter on single crystals, it is obvious that the absolute conductivity enhancement is lower in case of polycrystalline materials. This is plausible, given the random orientation of grains in polycrystals which can lead to a varying dislocation generation in grains based on their critical resolved shear stress (CRSS). Another reason could be that the presence of GBs increase the strength of the material - e.g. in Figure 5.13 the stress required to create dislocations in nanosize grains is higher than in macrosized grains. This is also a reason for sintering the SPS samples at 400 MPa compared to the single crystals (40 MPa) to form a perceptible amount of dislocations.

In polycrystalline materials Hebb-Wagner type polarization measurements indicated an ionic transference number of 0.7 at 1 bar to 10⁻³ bar *p*O₂. The equivalent trivalent

5.4 Conclusions on polycrystalline TiO₂

acceptor concentration required to achieve such an enhancement in the homogeneous bulk would be 0.5 mol% - which is often unattainable by chemical acceptor doping especially for dopants of larger ionic radii. High temperature annealing showed only a moderate decrease of this conductivity proving the persistence of the dislocations.

5. POLYCRYSTALLINE TiO_2

6

Y-doped/decorated polycrystalline TiO₂

The previous chapters demonstrate that 1-D defects influence the electrical properties of TiO₂. In this chapter, a special focus is laid on acceptor dopant (viz., Y³⁺) effects on the dislocation generation and electrical properties of polycrystalline TiO₂. Three different cases are considered to investigate the dopant effect on dislocations and electrical properties. They differ mainly in the sample preparation methods such as (1) homogeneous doping followed by conventional sintering (referred as CS-dop) (2) homogeneous doping followed by spark plasma sintering (SPS-dop) and (3) GB decoration followed by spark plasma sintering (SPS-dec). Since due to the diffusion of the dopant into the bulk, conventional sintering of a GB decorated sample approaches closely case (1), this case was not studied. Case (2) and case (3) differ owing to the fast sintering process in the SPS which keeps the dopant largely at the GB's.

6.1 Sample preparation

Experimental details of introducing dopants into TiO₂ powders are described in section 3.2.1. For conventional sintering, samples were sintered at 1300 °C for 5 h in air and for the SPS samples (compacted with same conditions as earlier - 925 °C, 400 MPa for 5min), re-oxidation treatment was done at 1000 °C for 1 h to 5 h in air.

6. Y-DOPED/DECORATED POLYCRYSTALLINE TiO₂

SEM images of the 0.1 mol % Y doped TiO₂ samples are shown in Figure 6.1. The density of the SPS-dop and SPS-dec samples are approx. 90 % and 93 % respectively, as determined by the Archimedes principle, therefore, the visible porosity in SEM images is mostly due to open porosity. The CS samples are approx. 92 % dense as calculated from the geometry. The average grain size of CS-dop, SPS-dop and SPS-dec samples, as determined from ImageJ program, is $8.7(\pm 4)$ μm , $2.7(\pm 0.9)$ μm and $4.6(\pm 1.6)$ μm respectively.

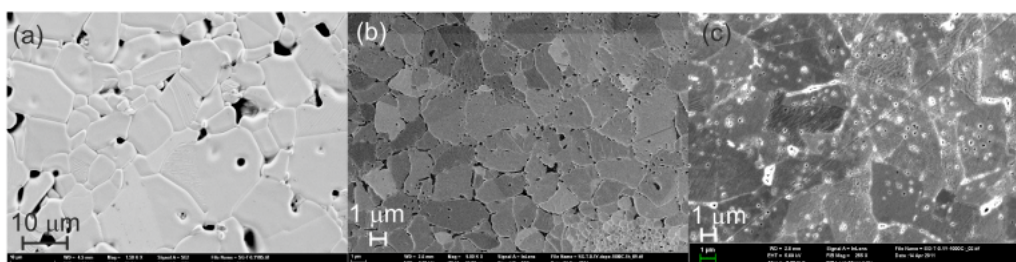


Figure 6.1: SEM images of 0.1 mol% Y doped (a) conventionally sintered (CS-dop) (b) spark plasma sintered TiO₂ (SPS-dop) post heat treatment at 1000 °C - 1 h and (c) Y decorated TiO₂ (SPS-dec) post heat treatment at 1000 °C - 5 h. Samples are polished and thermally etched at 50 degrees below the sintering temperature for 30 min.

6.2 Defect characterization

1-D Defect characterization was performed by a Phillips CM 400 microscope as in the previous chapters. At least two specimens were prepared from the center of the original samples.

6.2.1 Acceptor decorated TiO₂

Figure 6.2 shows a bright field TEM image of the 0.1 mol% Y decorated TiO₂ sample (SPS-dec) focused inside a large grain with beam axis parallel to [010]. Several dislocations (dark contrast) are observed to be on {101}, very similar to that observed in polycrystalline undoped TiO₂ (Chapter 5) and in the literature [39–41, 104]. Figure 6.2b is from the same grain with only the [101] reflection operating, indicating that most of the dislocations lie on {101} planes. Several grains were

examined (not shown here) and it was found that the dislocation densities were well comparable to that of the undoped polycrystalline TiO_2 (cf. Figure 5.2).

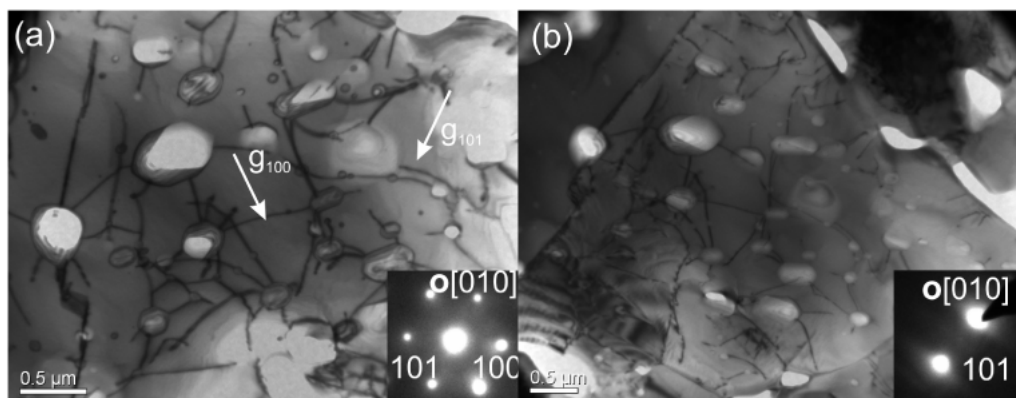


Figure 6.2: Bright field TEM images of 0.1 mol% Y decorated TiO_2 (SPS-dec) (a) with beam axis parallel to $[010]$ and (b) the same grain with $\mathbf{g}=101$.

6.2.2 Acceptor doped TiO_2

In case of acceptor doped TiO_2 (SPS-dop), Y is homogeneously distributed throughout the sample. Figure 6.3 shows a bright field TEM image of the 0.1 mol % Y doped TiO_2 focussed on two grains (grain 1 and 2), with grain 1 oriented parallel to the $[101]$ beam axis. There is no dislocation contrast observed in any of the grains. In order to improve the dislocation contrast a two beam condition was selected with $\mathbf{g}=(-101)$ (Figure 6.3b) which is one of the favorable planes to view dislocations in TiO_2 [39–41, 104]. There were no observable dislocations under this condition even for the grains that are of comparable size to the undoped SPS and 0.1 mol% Y decorated TiO_2 (SPS-dec) which showed dislocations. Several grains were studied and it is obvious that much fewer dislocations were observed in homogeneously doped TiO_2 in comparison to the undoped and Y-decorated samples. Only a few grains (approximately one in 20 or even a lower fraction) show a small number of dislocations as depicted in Figure 6.4. The inset of Figure 6.4 shows the diffraction pattern of the image, and the satellite spots correspond to a twin defect.

To summarize, TEM characterization showed that only 0.1 mol % Y decorated TiO_2 (SPS-dec) has a similar dislocation density and structure as that of an undoped TiO_2 . Interestingly, a very low dislocation density is observed in case of

6. Y-DOPED/DECORATED POLYCRYSTALLINE TiO₂

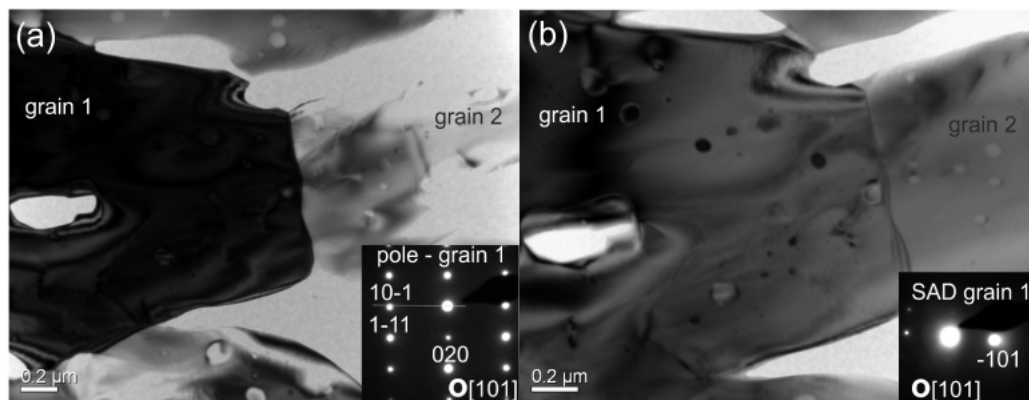


Figure 6.3: Bright field TEM images of 0.1 mol% Y doped TiO₂ (SPS-dop)(a) with beam axis [101] parallel to grain 1 and (b) with $g=-101$ for grain 1.

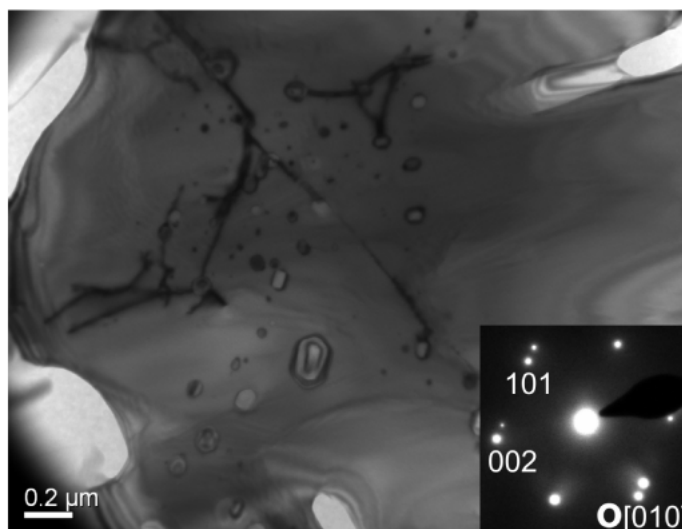


Figure 6.4: Bright field TEM images of 0.1 mol % Y doped TiO₂ (SPS-dop) with beam axis parallel to [010].

homogeneously acceptor doped TiO_2 . Conventionally sintered Y doped samples were not characterized by TEM as the possibility of dislocation generation is negligible for room temperature compression and pressure-free sintering.

6.3 Electrical characterization

6.3.1 Conventionally sintered and spark plasma sintered 0.1 mol % Y doped TiO_2

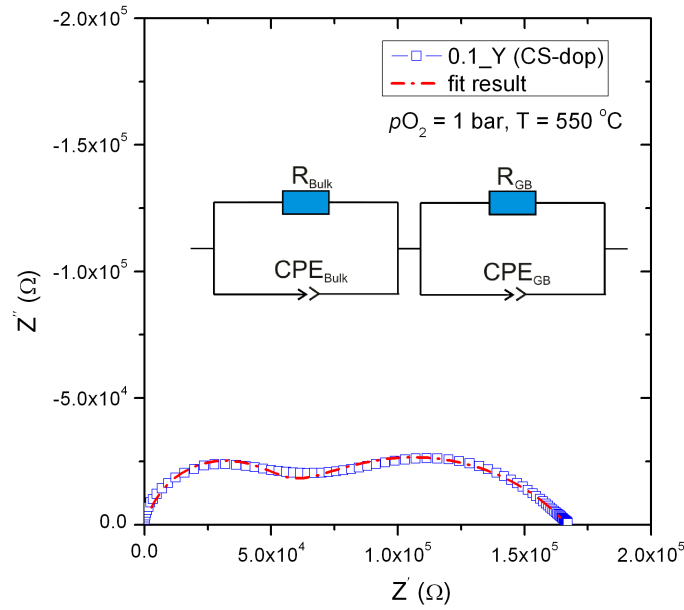


Figure 6.5: Impedance spectrum measured at 550 °C in 1 bar $p\text{O}_2$ for the CS 0.1 mol % Y doped TiO_2 sample sintered at 1300 °C for 5 h, the ideality factor at high frequency (HF) and low frequency (LF) is $\psi_{HF}=0.91$ and $\psi_{LF}=0.53$.

A typical impedance spectrum for CS 0.1 mol % Y doped TiO_2 is shown in Figure 6.5, the inset shows the equivalent circuit used to extract the fit parameters. The presence of two distinguished semicircles at high frequency (HF) and low frequency (LF) indicates two different physical processes. The capacitance of the HF semicircle of approx. 10^{-11} F corresponds to the bulk permittivity value of TiO_2 ($\epsilon_r=120$, calculated according to Equation (3.3)). The measured LF capacitance of

6. Y-DOPED/DECORATED POLYCRYSTALLINE TiO₂

approx. 10^{-9} F corresponds to an apparent permittivity of 10,000 and can probably be attributed to GB's. A low ideality factor ($\psi = 0.53$) points towards inhomogeneous grain boundary contacts, due to porosity (Figure 6.1) leading to current constriction.

The bulk and GB conductivities measured at different pO_2 and analyzed according to Equations (3.1) and (3.2) are shown in Figure 6.6, data of the CS-undoped sample is also shown for comparison. At high pO_2 (1 bar to 10^{-5} bar), increase in p-type conductivity over 1 order of magnitude compared to the CS (undoped) sample shows the effect of acceptor dopant. The pO_2 exponent (m) = $+1/4$ indicates that the majority charge carriers are holes, which is in agreement with the TiO₂ defect model (Section 2.3) and earlier experimental results in the literature [3, 37, 73]. The GB conductivity exhibits the same pO_2 dependence exponent indicating no changes in the nature of charge carriers compared to the bulk. At low pO_2 ($<10^{-10}$ bar), the pO_2 exponent equals $-1/4$ and $-1/6$ (at even lower pO_2) representing n-type conductivity (Section 2.3).

The activation enthalpy for conduction of electron holes in the bulk and GB for

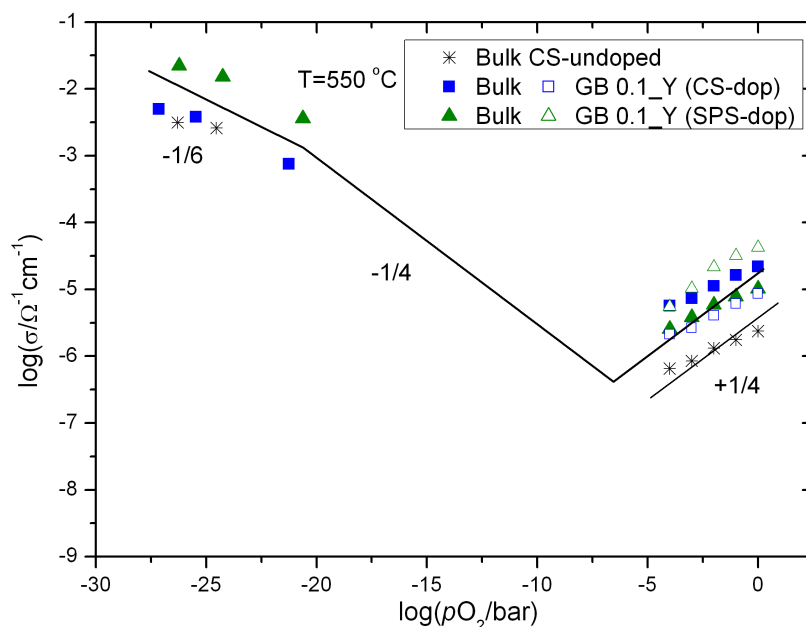


Figure 6.6: AC conductivity as a function of pO_2 for the CS and SPS 0.1 mol % Y doped TiO₂ samples (with negligible dislocations). The slopes in the low- pO_2 regime are drawn according to the values expected from the bulk defect chemical model.

the CS 0.1 mol % Y doped sample is shown in Figure 6.7. At 1 bar pO_2 , the bulk activation energy corresponds to 0.9 eV and 1.4 eV for GB's, which is very close to the undoped CS samples in Chapter 5 (Figure 5.5).

A typical impedance spectrum of 0.1 mol % Y doped sample (SPS-dop) is shown

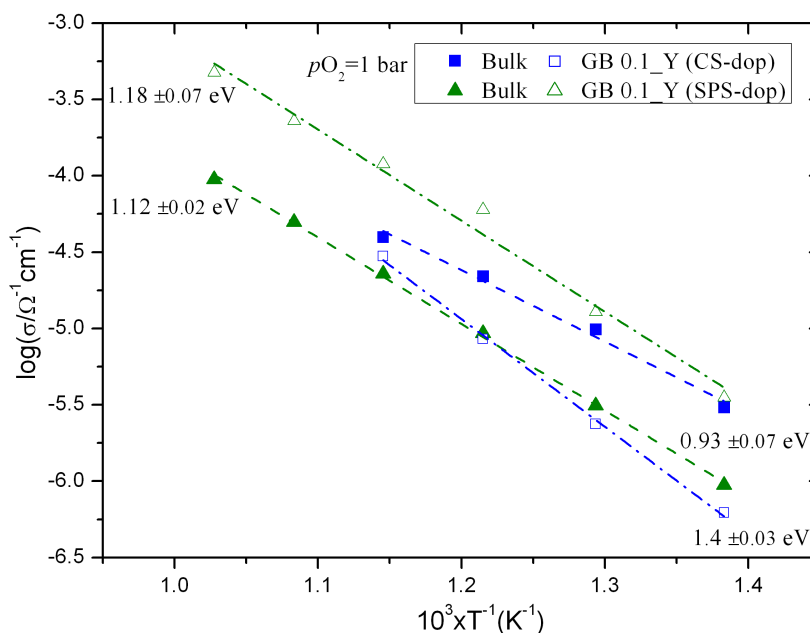


Figure 6.7: Arrhenius plot for the CS and SPS 0.1 mol % Y doped TiO_2 samples (with negligible dislocations).

in Figure 6.8. The spectrum consists of two relaxation processes where the low frequency contribution is much smaller than the high frequency part. Based on the measured capacitance (2×10^{-11} F), a relative permittivity ($\epsilon_r=90$) was calculated according to Equation (3.3) which corresponds to the bulk contribution of the sample. Since there are no continuous dislocations as determined by TEM (Figure 6.3), the observed HF contribution can be assigned to the regular bulk conductivity of the sample (no enhanced dislocation conductivity which would also be combined with a bulk capacitance (cf. Section 5.2.2)). The calculated apparent permittivity (~ 5000) at low frequency can be assigned to the GB's (measured capacitance was 1×10^{-9} F). It is evident from the spectrum that the boundary resistance of the SPS sample is at least a factor of 5 smaller than for the CS-dop sample with similar density. A plausible reason could be the modification of boundary morphology by SPS (com-

6. Y-DOPED/DECORATED POLYCRYSTALLINE TiO₂

paction at elevated temperature and reducing conditions). Another reason could be a more homogeneous boundary-boundary contact by local Joule heating [126] which decreases porosity at GB's that may lead to current constriction.

The electrical conductivity as function of pO_2 is shown in Figure 6.6 for the SPS 0.1

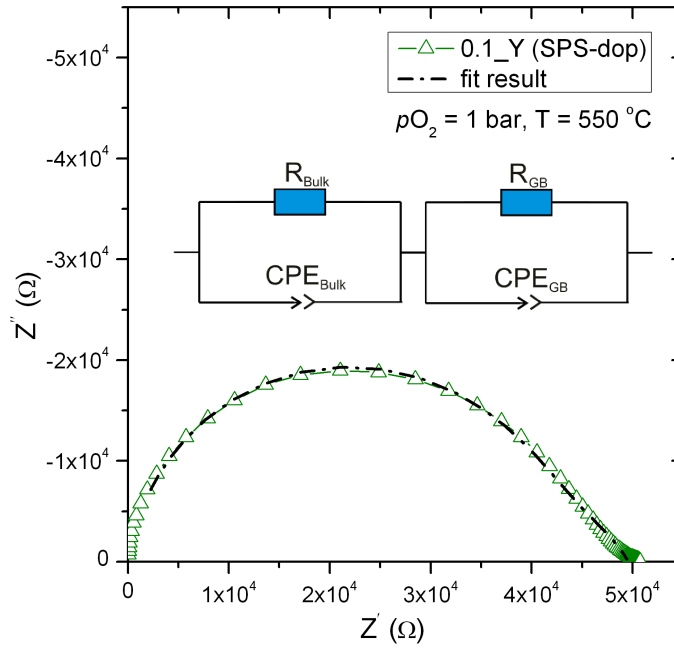


Figure 6.8: Impedance spectrum measured at 550 °C in 1 bar pO_2 for the SPS 0.1 mol % Y doped TiO₂ (SPS-dop) sample re-oxidized at 1000 °C for 1 h, inset shows the equivalent circuit used for fitting the data with $\psi_{HF}=0.93$ and $\psi_{LF}=0.65$.

mol % Y doped sample. The pO_2 exponent at high ($> 10^{-10}$ bar) and low ($< 10^{-10}$ bar) partial pressures exactly match with the CS 0.1 mol % Y doped sample (Figure 6.6) and agree with the bulk defect chemistry (Section 2.3 and earlier such experimental results on TiO₂ [3, 37, 73]). At high pO_2 , the total conductivity of the SPS sample is very close to the CS 0.1 mol % Y doped TiO₂ indicating no structural changes (like dislocations) in the samples. The observed match in the conductivity is further supported by the TEM characterization of the SPS 0.1 mol % Y doped sample where no dislocations were observed (Figure 6.3). The invariance of the conductivity is very interesting when compared with the undoped SPS samples in Chapter 5 which were prepared under same SPS conditions (925 °C, 400 MPa for 5min) and showed an entirely different (pO_2 -independent) conductivity at high pO_2 .

The enhancement in n-type conductivity by half an order of magnitude in Figure 6.6 should not be over-emphasized given the uncertainty in the interpretation of EIS data at such low pO_2 , to assign the measured conductivity either to the bulk or GB (spectra show inductive loops). So the difference in conductivity values at low pO_2 is rather due to uncertainties in calculating the low impedance values.

Figure 6.7 shows the Arrhenius plot for the Y doped SPS sample in 1 bar pO_2 . The measured bulk and GB activation energies are approx. 1.1 and 1.2 eV, respectively. The bulk conductivity is close to the CS sample (taking possible experimental error into consideration) and the activation energy of the GB conductivity is 0.2 eV lower compared to the CS sample.

6.3.2 Spark plasma sintered 0.1 mol % Y decorated TiO_2

Figure 6.9 presents a typical impedance spectrum of 0.1 mol % Y decorated TiO_2 sample (SPS-dec) measured at 550 °C under 1 bar pO_2 . The spectrum shows a large HF and small LF contributions, very similar to the SPS doped sample. However, the high frequency semicircle now corresponds to the enhanced conductivity along the dislocations rather than to the bulk conductivity (both lead to the same bulk capacitance cf. Section 5.2.2). This assignment is based on the TEM characterization, which showed a dense network of dislocations throughout the specimen very similar to the undoped single crystals and polycrystals in the previous chapters. The measured high frequency capacitance of 3×10^{-11} F results in a relative permittivity of 180 which is slightly higher than the bulk permittivity of TiO_2 (which is around 60-120, see Table 2.1). The low frequency semicircle contribution is lower, with a capacitance of 3×10^{-9} F (corresponding to an apparent permittivity of 20,000).

The conductivity due to the dislocations (labeled as disl.) is plotted as a function of pO_2 in Figure 6.10. At high pO_2 (1 bar to 10^{-10} bar) the measured conductivity is independent of pO_2 indicating a predominant ionic conductivity which is different from the CS and SPS 0.1 mol % Y doped samples that showed a predominant p-type conductivity (Figure 6.6). On the other hand, conductivity of SPS-dec is similar to the undoped polycrystalline SPS sample (with a very similar 1-D defect structure) as shown in Figure 6.10. At high pO_2 the conductivities of both the samples are very close. At low pO_2 , the n-type conductivity is higher in the SPS Y-decorated

6. Y-DOPED/DECORATED POLYCRYSTALLINE TiO₂

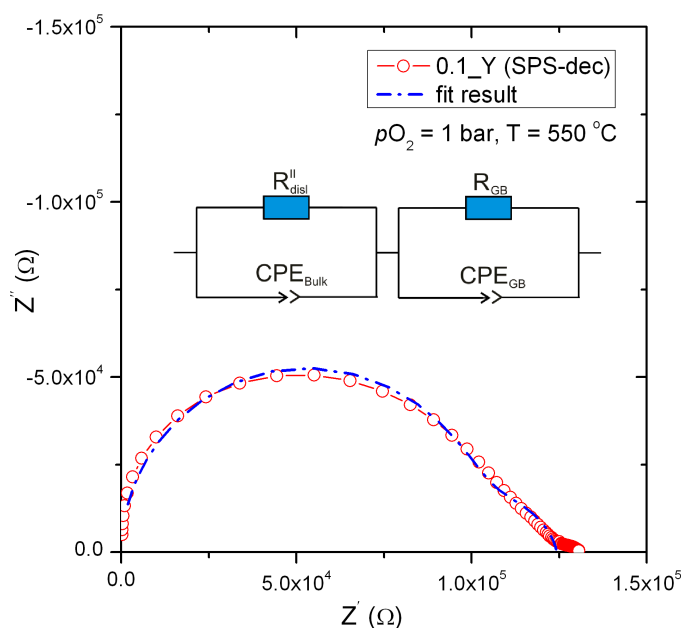


Figure 6.9: Impedance spectrum measured at 550 °C in 1 bar pO_2 for the SPS 0.1 mol % Y decorated TiO₂ (SPS-dec) sample re-oxidized at 1000 °C for 5 h, inset shows the equivalent circuit used for fitting the data with $\psi_{HF}=0.99$ and $\psi_{LF}=0.95$.

sample compared to the undoped ones, which is in contrast with the regular defect chemistry*. The probable explanation may be that changes occur in the sintering process in presence of dopants (note that the n-type conductivity exactly matches with that of the SPS 0.1 mol % Y doped sample in Figure 6.6). Additionally, there are experimental limitations at these low impedance measurements (typically 40 Ω at 10^{-26} bar) which lead to an inductive loop thereby making the data analysis very difficult.

The activation enthalpy for conduction via positively charged defects at high pO_2 is shown in Figure 6.11, the activation energy for conduction along the dislocations is approx. 1.5 eV which is similar to the undoped SPS samples with dislocations. This match in the activation energy points to the same conductivity mechanism in both samples due to the presence of dislocations. The increased activation energy in comparison to the CS and SPS 0.1 mol % Y doped samples also indicates the change in the predominant charge carrier from holes to ions.

*A decrease in n-type conductivity is expected on introducing negative charged defects such as acceptors

6.3 Electrical characterization

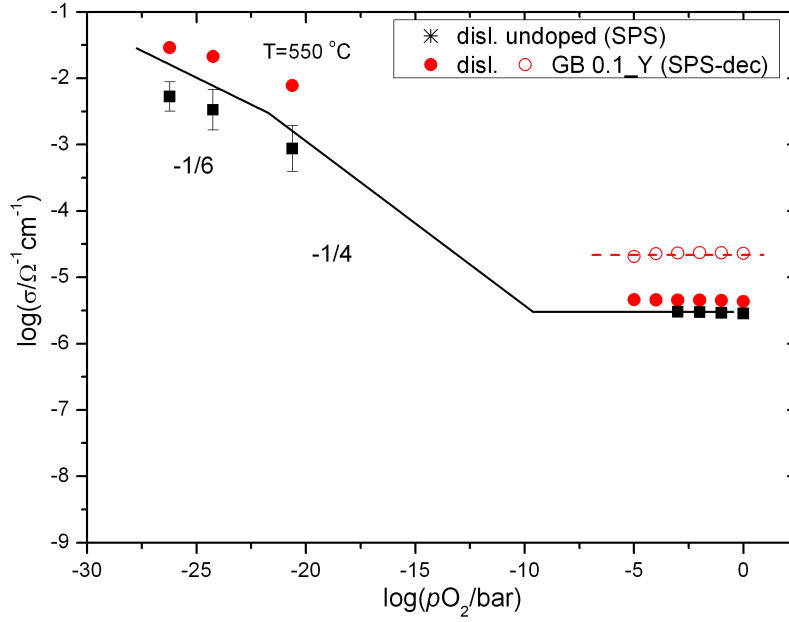


Figure 6.10: AC conductivity as a function of $p\text{O}_2$ for the SPS 0.1 mol % Y decorated TiO_2 samples (with dislocations), the SPS undoped polycrystalline sample data is shown for comparison. The slopes in the low- $p\text{O}_2$ regime are drawn according to the values expected from the bulk defect chemical model.

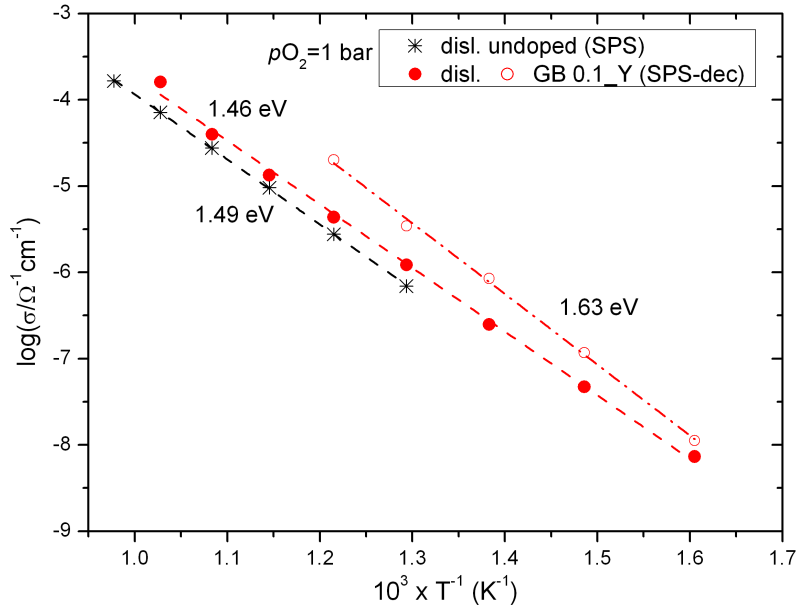


Figure 6.11: Arrhenius plot for the SPS 0.1 mol % Y decorated and undoped TiO_2 samples with dislocations.

6.4 Discussion

In this section, the two key observations from the experimental results (summarized in Figure 6.12) will be re-addressed:

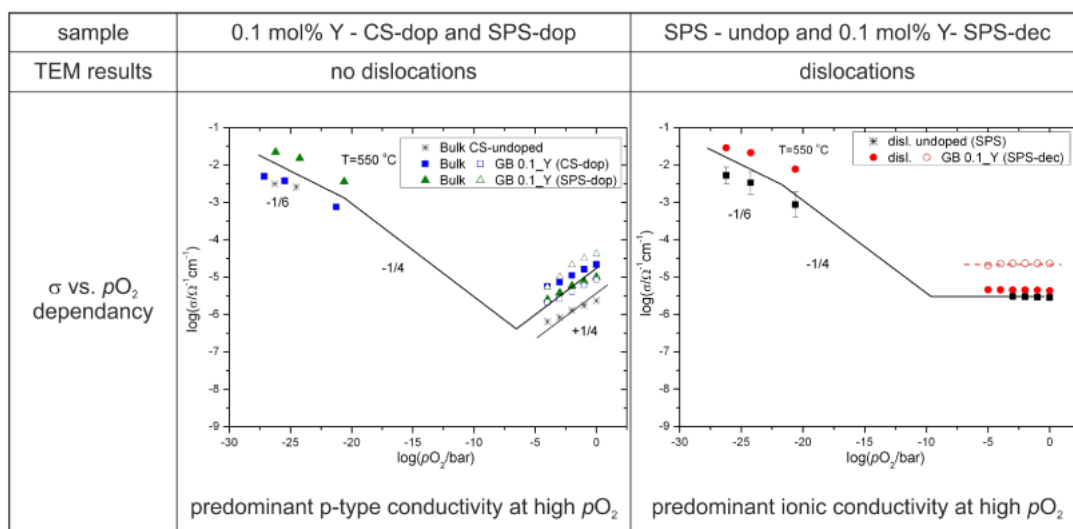


Figure 6.12: Summary of conductivity plots of 0.1 mol % Y doped and decorated TiO₂ samples.

- At high pO_2 (1 bar to 10^{-5} bar) there is no change in the 0.1 mol % Y doped TiO₂ conductivity irrespective of the sintering procedure, i.e., CS or SPS, while similar SPS parameters consistently lead to dislocation creation in both undoped and 0.1 mol % Y decorated TiO₂ samples.
- There is a conductivity change in the 0.1 mol % Y decorated TiO₂ SPS samples in comparison to the 0.1 mol % Y doped CS and SPS samples. The modified conductivity is very similar to the undoped SPS sample.

A striking feature of the 0.1 mol % Y doped SPS sample is the absence of any dislocation network as shown in Figure 6.3. Undoped or decorated samples compressed with same SPS parameters always lead to dislocation network formation (cf. Figure 5.2 and Figure 6.2). The grain size of the Y SPS-dop sample is comparable to the undoped and Y decorated SPS samples, hence, a grain size (microstructure) effect on the creep deformation properties (refer Section 5.3.1) can be ruled out. So, the

only change in the sample comes from the homogeneous doping of Y in TiO_2 . Such a bulk doping is supposed to lead to an increase in the bulk strength of the material as commonly known as solid solution strengthening. Because of this effect, the yield stress required to create dislocations is increased to values that may be beyond 400 MPa (the present experimental condition). The solid solution strengthening is a common phenomenon in doped metallic systems for eg. in Al alloys [127], Cu alloys [128, 129] and Mg alloys [127, 130]. In semiconductor GaAs, In doping resulted in decreased dislocation density due to solid solution hardening [131, 132]. Further, it appeared also in oxide systems, e.g., for 0.01 mol %Y doped Al_2O_3 , leading to an increase in creep strength by about two orders of magnitude [133]. Similar observations for other rare-earth acceptor type dopants [134, 135] are also known. In YSZ, where acceptor dopants with larger ionic radii compared to Zr^{4+} lead to an increase in strength of the material, the strengthening effect was related with the ionic radii of dopants [136, 137]. The reasoning for this improvement was explained by modification of bulk diffusivity by the doped cation which thereby influence the true stress of the material [136]. Based on these observations in literature, it is convincing that Y doping lead to a solid solution strengthening of TiO_2 and hence no dislocations are created in the grains. Therefore, the absence of dislocations in the SPS doped sample resulted in a regular bulk defect chemistry of acceptor doped TiO_2 similar to the CS Y-doped sample.

The predominant ionic conductivity in 0.1 mol % Y decorated SPS sample (Figure 6.10) can be rationalized in the framework of negative dislocation core and accumulation space charge zones in the p-type regime (cf. Figure 4.19) as described in the previous chapters (Chapter 4 and 5). Figure 6.10 presents comparable ionic conductivities in both the undoped and 0.1 mol % Y decorated SPS samples indicating very similar dislocation features, and no influence of the decorated dopant on the bulk point defect chemistry*. This can be attributed to the fast sintering process in SPS that keeps the dopants confined close to the GB's. A long equilibration time (annealing) may redistribute the dopants and tend to modify conductivity of these samples. Based on the Sc^{3+} tracer diffusivity data by Sasaki et. al. [31], for a grain size of 3-4 μm (averaged grain size of the SPS-dec sample) the average annealing

*An acceptor dopant in TiO_2 results in an increase of $[\text{V}_{\text{O}}^{\bullet\bullet}]$, which in turn also increases the hole concentration at high $p\text{O}_2$

6. Y-DOPED/DECORATED POLYCRYSTALLINE TiO₂

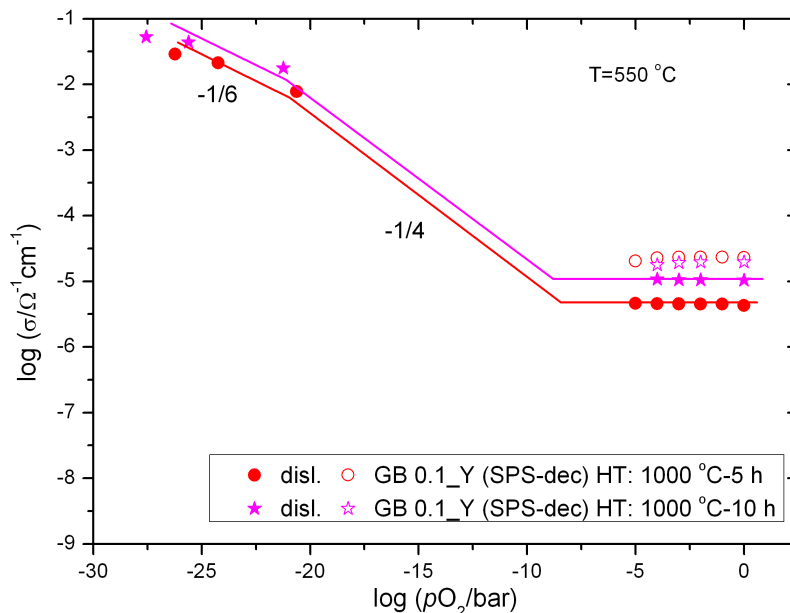


Figure 6.13: AC conductivity as a function of $p\text{O}_2$ for the SPS 0.1 mol % Y decorated TiO₂ samples after annealing at 1000 °C for 10 h. The slopes in the low- $p\text{O}_2$ regime are drawn according to the values expected from the bulk defect chemical model.

time required to diffuse dopants that are of comparable size to Sc^{3+} ($r=0.745 \text{ \AA}$) is approx. 10 h at 1000 °C. For Y^{3+} ($r=0.9 \text{ \AA}$) this might be considerably longer.

Figure 6.13 shows the effect of longer annealing time (1000 °C for 10 h) on the electrical conductivity of 0.1 mol % Y decorated SPS sample. At high $p\text{O}_2$ (1 bar to 10^{-5} bar), the bulk conductivity from positively charged ionic carriers ($\text{V}_{\text{O}}^{\bullet\bullet}$ or $\text{Ti}_i^{\bullet\bullet\bullet\bullet}$) is increased up to half an order in magnitude. Since no significant change in the dislocation structure is expected from this annealing treatment (cf. Section 5.2.4 and also Figures 6.2 and 6.16), the increased conductivity should still be dominant by dislocations (i.e. via space charge regions) rather than by the bulk contribution. Further, a dominant bulk contribution would lead to a p-type hole conductivity but not $p\text{O}_2$ -independent ionic conductivity in TiO₂ as observed in Figure 6.6. The $p\text{O}_2$ -independent conductivity also suggests that the Y is not homogeneously distributed within the grain (cf. p-type conductivity for 0.1 mol % Y-dop sample Figure 6.6). The slight enhancement in Figure 6.13 could be due to one or a combination of the following possibilities.

1. According to Equation (2.23), at a fixed core charge density, for a large space

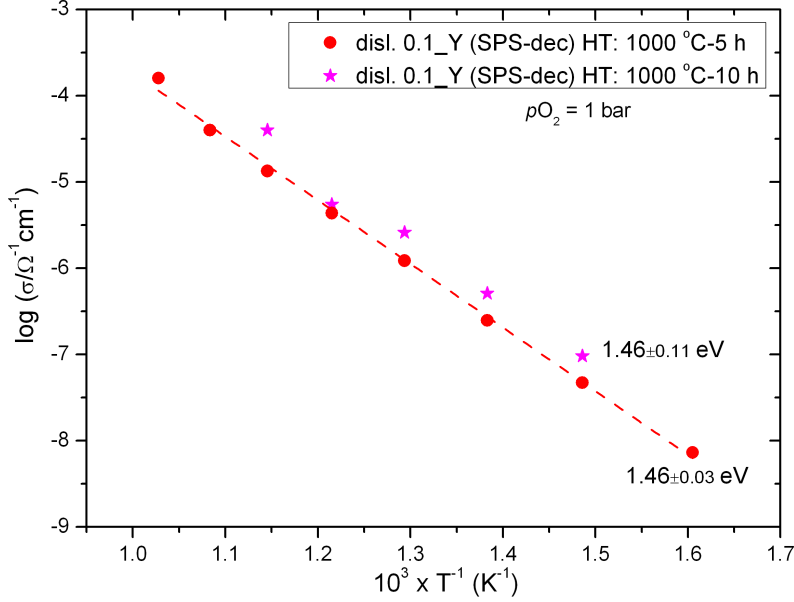


Figure 6.14: Arrhenius plot for the SPS 0.1 mol % Y decorated TiO_2 samples before and after annealing at 1000 °C for 10 h.

charge potential (typically, $z_i \Delta \phi^\circ \geq 0.5V$) an increase in bulk dopant concentration ($[A'_{\text{Ti}}] = 2[V_{\text{O}}^{\bullet\bullet}]$) would not change the defect accumulation, but for a small space charge potential ($z_i \Delta \phi^\circ \leq 0.3V$) there would be a slight increase of the accumulated positive charge carriers close to the dislocation core - a zone with possibility of increased mobility due to strain.

- It is widely accepted that impurities tend to segregate to the GB or dislocation cores with either electrostatic attraction and/or release of dopant size misfit as the driving force. A recent work on MgO revealed that the energy for dopant incorporation is 1.0-2.5 eV lower at dislocations compared with the bulk structure leading to dopants segregation [138]. A similar situation could arise in the long-annealed sample, if the mismatch driving force dominates over the electrostatic repulsive force (case of small space charge potential), leading to a further increase in the core charge density. In order to compensate this excess negative core charge, the adjacent space charge zones accumulate more positive charge carriers, as schematically shown in Figure 6.15, increasing the conductivity of the long-annealed sample.

6. Y-DOPED/DECORATED POLYCRYSTALLINE TiO₂

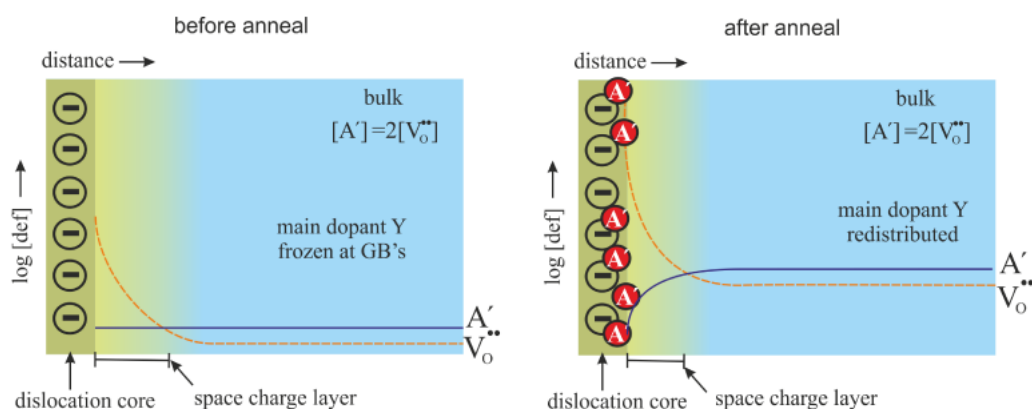


Figure 6.15: Schematic representation of oxygen vacancy defect profile in the bulk and space charge zone for the SPS 0.1 mol % Y decorated TiO₂ sample with increase in annealing time.

The predominance of the ionic conductivity over electron hole conductivity can be understood from the influence of the space charge potential on the charged defects, which increase the ionic defect concentration over the electronic defects according to Equation (2.19). The unchanged activation energy (Figure 6.14) indicates that the conductivity mechanism is unchanged with the annealing treatment. To support this interpretation, TEM characterization was performed on the long annealed sample, shown in Figure 6.16. It revealed persistent dislocations even after the long annealing treatment. Comparing Figures 6.2 and 6.16 it is qualitatively obvious that there is not much variation in the density of dislocations. The conductivity plots (Figures 6.13 and 6.14) together with TEM characterization (Figure 6.16) nicely demonstrate that point defects diffuse at a much faster rate compared to 1-D defects (dislocations) in TiO₂.

6.5 Chapter conclusions

The influence of acceptor type doping/decoration on dislocation formation and the electrical properties of TiO₂ is investigated in this chapter. Homogeneous acceptor doping of 0.1 mol % Y in TiO₂ suppresses dislocation generation by solid solution strengthening. Therefore, in absence of dislocations, the electrical properties of the spark plasma sintered and conventionally sintered 0.1 mol % Y doped TiO₂ are similar and in agreement with the bulk defect chemistry of acceptor doped TiO₂.

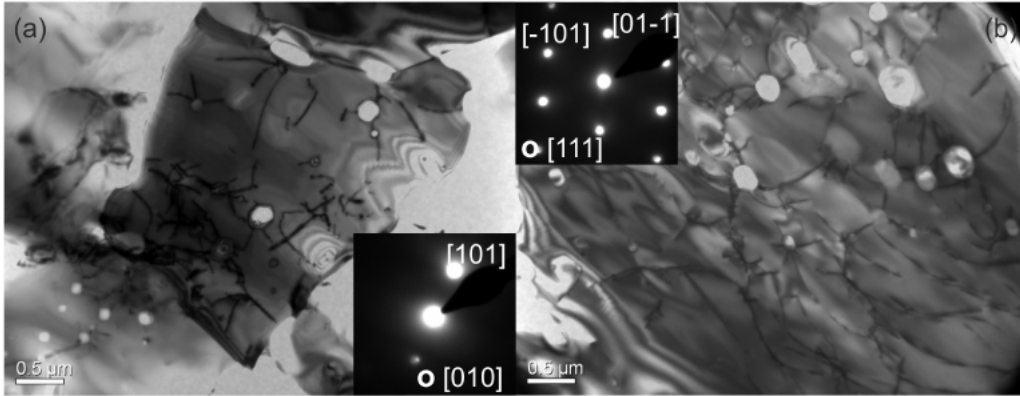


Figure 6.16: Bright field TEM images of 0.1 mol % Y decorated TiO_2 after a long annealing treatment at 1000 °C for 10 h, (a) with beam axis parallel to [010] and (b) the same grain with $\mathbf{g}=101$.

In case of the Y decorated SPS sample, the absence of dopants in the bulk (no solid-solution strengthening) leads to the formation of persistent dislocations. In the presence of dislocations the electrical properties are close to that of the undoped SPS samples (Chapter 5). At high $p\text{O}_2$, both samples showed a predominant ionic conductivity due to a percolating network of negatively charged dislocation core and accumulation space charge zones. Electrical conductivity of 0.1 mol % Y decorated SPS sample can be tuned by redistributing the Y dopants from the GB's in to the bulk by an annealing treatment at 1000 °C for 10 h. Most probably due to dopant redistribution and segregation to the dislocation core, the overall positive defects are slightly increased in the space charge zone resulting in an increase in ionic conductivity by approx. half an order of magnitude.

6. Y-DOPED/DECORATED POLYCRYSTALLINE TiO_2

Part II

Results and discussion on 2-D defects

7

Symmetric tilt boundaries

The second part of this thesis mainly focusses on 2-D planar defects viz. grain boundaries and their influence on the electrical properties of TiO_2 . Since polycrystalline TiO_2 consists of many grain boundaries that separate grains of random orientations, it is difficult to define and characterize each of them. Further, in oxides such as SrTiO_3 , it was observed that different grain boundaries have varying electrical properties [21]. Therefore, electrical measurement of a polycrystalline material delivers an apparent value that is averaged over several hundreds of grain boundaries. Bicrystals with a well defined grain boundary orientation can serve as model materials for these studies. In this work, mainly two symmetric tilt boundaries viz. a $\Sigma 5$ boundary (a $(210)[001]$ tilt boundary) and 6° tilt boundary along $[001]$ were synthesized and characterized (see section 3.6.1 for details). The effect of acceptor decoration (Y) was also studied in these bicrystals by depositing Y_2O_3 on one of the bonding surfaces by PLD, this ensures that a large portion of the dopant remains in the GB core, see Section 3.6.1 for experimental details.

7.1 Structural characterization - TEM

Phillips CM 400 and JEOL 4000FX microscopes were used for the boundary characterization of bicrystals. TEM specimens were prepared from a (001) section, the selection of TEM specimen from the initial $10 \times 10 \times 1 \text{ mm}^3$ bicrystal and the specimen orientation with respect to the electron beam axis is schematically shown in

7. SYMMETRIC TILT BOUNDARIES

Figure 7.1. As shown in the figure, the electron beam axis is chosen parallel to the boundary plane as to achieve a strong and well-separated signal from the bulk and the GB. TEM specimens was prepared with usual thinning procedures mentioned in Section 3.7.2. After sample thinning, the specimens were inspected under an optical microscope (Zeiss AXIO imager D1 m), representative images of $\Sigma 5$ and 3° symmetric tilt boundary (both undoped and Y-decorated specimens) are shown in Figure 7.2. Very few pores were observed in some samples irrespective of boundary type (undoped or decorated), the origin of these pores could be from the specimen preparation or from the initial synthesis (diffusion bonding) procedure. In general, the boundary is intact over the entire length of the crystal indicating a very well bonded bicrystal. The diffusion bond is so strong that these bicrystals can be mechanically polished or diced without any problem of shearing at the GB (grain boundary).

An overview of the $\Sigma 5$ boundary is shown in Figure 7.3, the TEM bright field

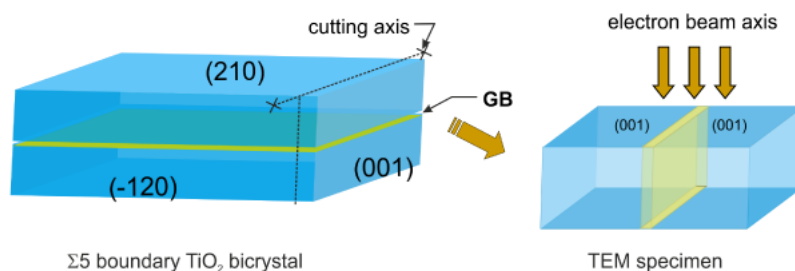


Figure 7.1: Schematic cartoon showing the TEM specimen and its orientation with respect to the electron beam axis in the microscope.

image shows that the boundary is perfectly bonded and free from any secondary phases. The periodical array of contrasts on the boundary is a result of dislocations and respective strain fields. As shown in the figure, the boundary is slightly curved and similar observations were found on other bicrystals as well.

$\Sigma 5$ (210)[001] tilt boundary

Figure 7.4 is a high-resolution transmission electron microscopy image (HRTEM) of the $\Sigma 5$ undoped boundary with a near atomic column resolution. The figure indicates that the two single crystals are perfectly bonded even at atomic scale without any impurity phases such as amorphous phase or precipitates. A slight variation in the atomic column contrast on either side of the boundary is due to the twist

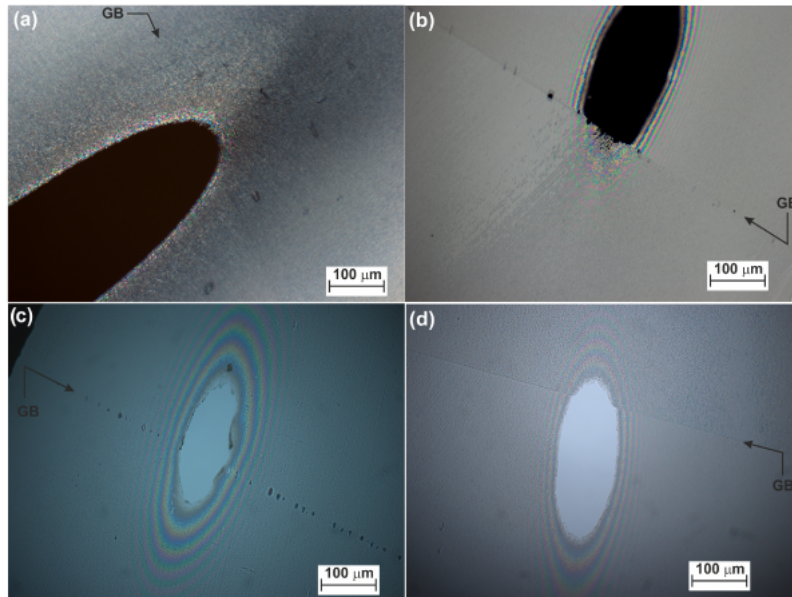


Figure 7.2: Optical light microscopy images of (a) 6° undoped, (b) $\Sigma 5$ undoped, (c) 6° - 0.5 nm Y decorated (transmission mode), (d) $\Sigma 5$ 1 nm Y decorated symmetric tilt boundaries, the large hole in the specimen (blade) is due to ion milling.

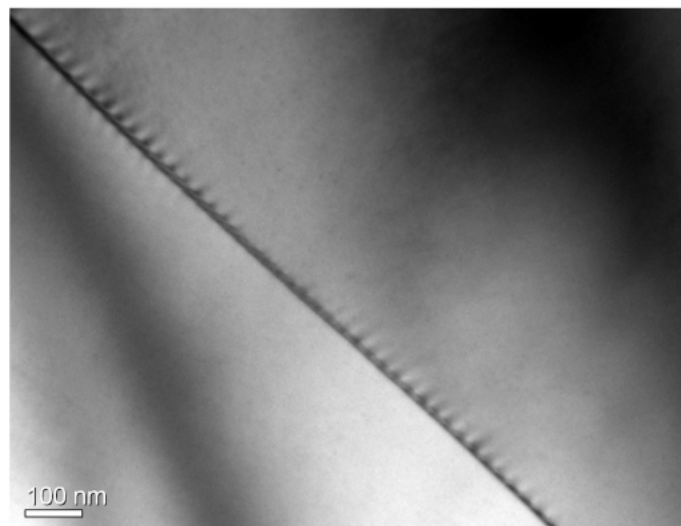


Figure 7.3: A TEM bright field image of the $\Sigma 5$ undoped symmetric (210)[001] tilt boundary.

7. SYMMETRIC TILT BOUNDARIES

in crystal alignment prior to the diffusion bonding. Insets in the figure represent diffraction patterns of respective crystals obtained by fast Fourier transform. The tilt angle between $[100]$ directions in both the crystals was estimated to be 53.8° , with a slight deviation ($\sim 1^\circ$) from the ideal $\Sigma 5$ misorientation of 53.1° . Taking the experimental limitations into consideration yields a very good match with the $\Sigma 5$ relation. The slight curvature in the boundary (Figure 7.3) can be rationalized from the 1° misfit from the exact $\Sigma 5$ relation and also the slight twist in the boundary.

The boundary structure of the same sample is further investigated in the Phillips

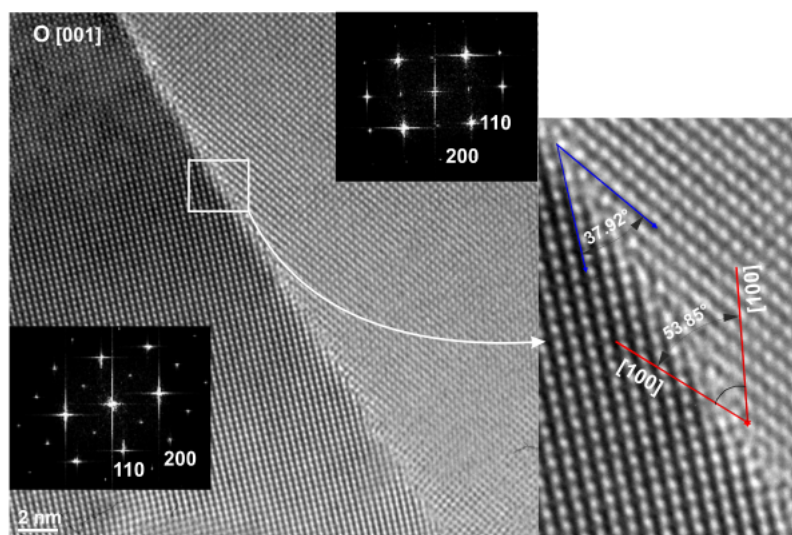


Figure 7.4: HRTEM image of the $\Sigma 5$ undoped symmetric tilt boundary, insets are the diffraction patterns of respective crystals obtained by fast Fourier transform.

CM microscope to understand the nature of dislocations in the GB core. Additionally, this will also help to investigate the effects of minor loading (~ 5 MPa) used for holding the crystals in diffusion bonding. This investigation is very critical for understanding the electrical properties, as the presence of dislocations in the crystal bulk results in modified electrical properties (cf. Part I Results and discussion). Figure 7.5 is a TEM bright field image of the $\Sigma 5$ undoped boundary showing an array of equally spaced (~ 30 nm) dislocations on the GB plane due to the twist in the crystal alignment. The bulk region of the bicrystal is free from dislocations, indicating that no plastic deformation occurred during the diffusion bonding. A similar characterization was performed on all the bicrystals and all the $\Sigma 5$ boundary samples show identical features.

In Figure 7.6, a high-resolution TEM image of a 1 nm Y-decorated $\Sigma 5$ boundary

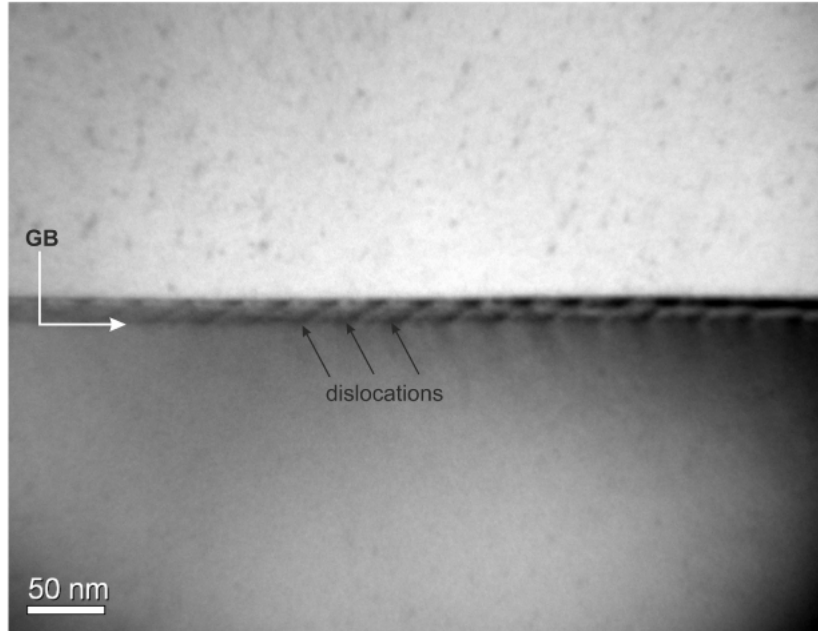


Figure 7.5: TEM bright field image of the $\Sigma 5$ symmetric tilt undoped boundary, the boundary plane was slightly tilted for a better view of dislocations.

is shown. The boundary has an almost perfect contact even at atomic scale and the measured tilt angle between $[100]$ is close to the ideal $\Sigma 5$ boundary. Since there are negligible possibilities of contamination of the samples, the contrast at the GB should arise from the Y dopant. EDAX analysis could not resolve the GB composition, due to a very low concentration of Y.

6° tilt boundary along $[001]$

A high-resolution TEM image in HREM mode with the boundary set at an edge-on condition is shown for the 6° tilt boundary (both undoped and 0.5 nm Y decorated) in Figure 7.7. The two single crystals have a perfect contact with a periodic array of dislocations that are equally spaced (~ 4 nm) to accommodate the tilt in the boundary. According to Frank's rule* for low angle tilt boundaries [139], the observed distance between the dislocation cores (~ 4 nm) in Figure 7.7 has a perfect match

* $d_{dis} = |b|/(2 \sin \theta/2)$ where d_{dis} is the distance between the dislocations, \mathbf{b} is the magnitude of the Burgers vector and θ is the misorientation angle

7. SYMMETRIC TILT BOUNDARIES

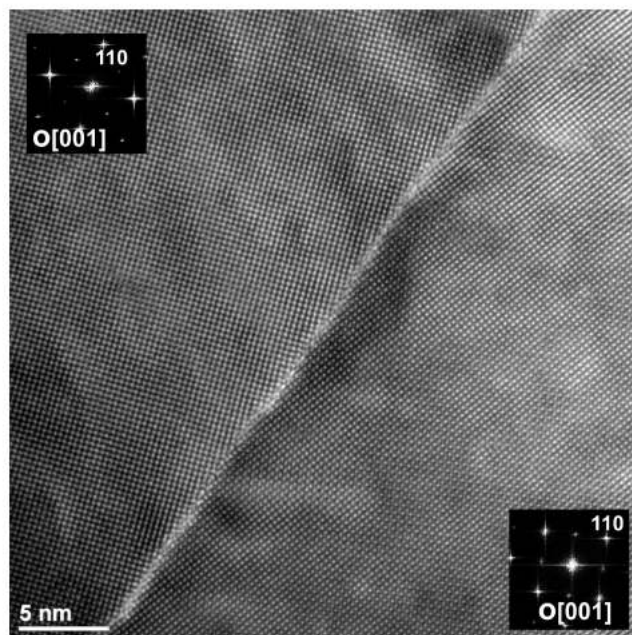


Figure 7.6: HRTEM image of the $\Sigma 5$ symmetric tilt Y-decorated boundary, insets are the diffraction patterns of respective crystals obtain by fast Fourier transform.

to what is estimated for a 6° tilt boundary (i.e., 3.7 nm, when $\mathbf{b} = 3.9 \times 10^{-10}$ m).

Figure 7.8 shows bright field TEM images of 6° symmetric tilt undoped and 0.5

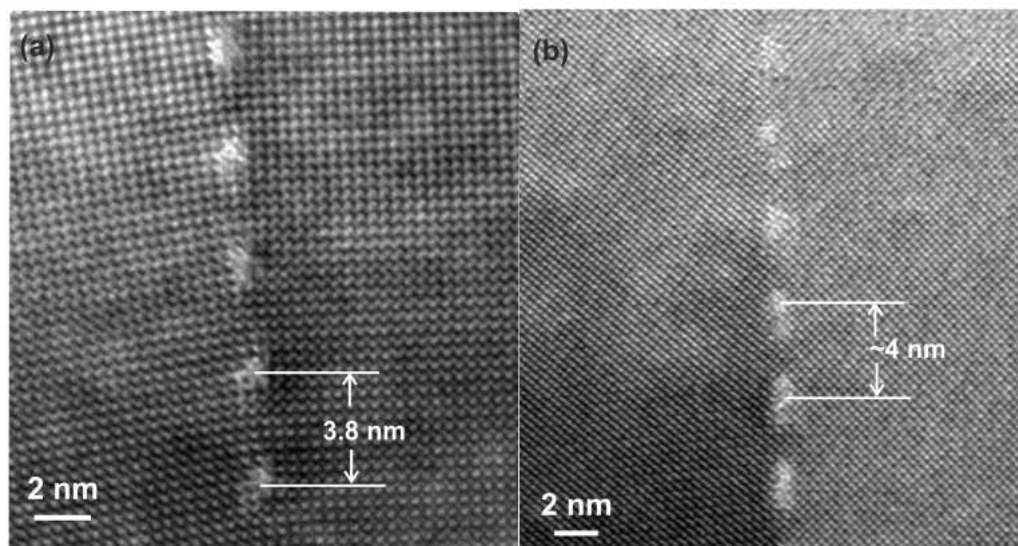


Figure 7.7: HRTEM image at an edge-on condition for the 6° (a) undoped and (b) 0.5 nm Y decorated symmetric tilt boundary when viewed along $[001]$.

nm Y decorated boundaries imaged with the Phillips CM microscope in diffraction mode. The boundary plane is largely inclined to the electron beam axis to obtain a better diffraction contrast for dislocations. On the GB plane, the periodic arrangement of dark and bright features correspond to the dislocations and the distance between them is ~ 4 nm, which is almost the same as for the situation shown in Figure 7.7. There are also other dislocations with larger distance (~ 120 nm) on the boundary plane of both the samples (distances slightly higher for 0.5 nm Y decorated sample). These dislocations are similar to that observed for the $\Sigma 5$ boundary in Figure 7.5. According to Frank's rule and the measured dislocation distance in Figure 7.7, it can be rationalized that a slight twist by 0.2° would lead to a dislocation distance of approximately 120 nm. Therefore, the dislocation spacing of these largely spaced dislocations can be conceived to originate from a small misalignment of the single crystals prior to diffusion bonding.

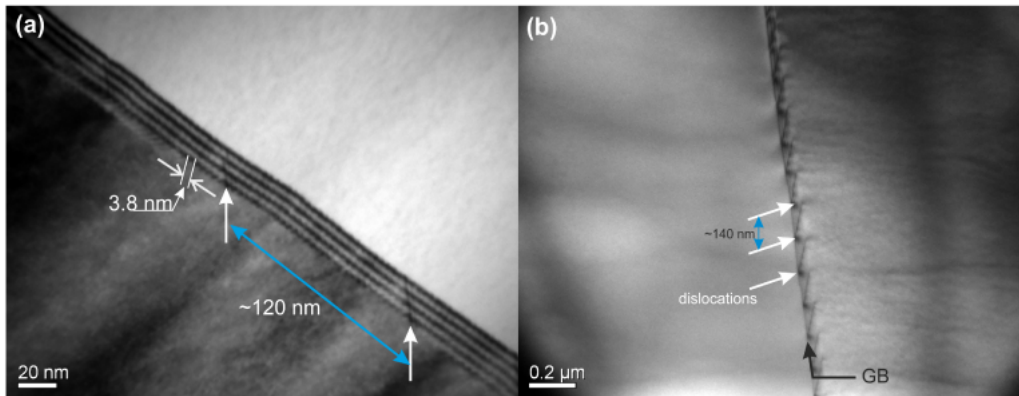


Figure 7.8: TEM bright field images of the 6° symmetric tilt (a) undoped and (b) 0.5 nm Y decorated grain boundary, sample tilted from beam axis for a better view of dislocations.

7.2 Electrical characterization - EIS

In this section electrical properties of various bicrystals will be compared with a special focus on the boundary type and dopant decoration. For brevity undoped boundaries will be discussed first and later each specific boundary will be compared

7. SYMMETRIC TILT BOUNDARIES

with its decorated boundary. Electrical characterization of the bicrystals was performed by applying thin Pt-paste electrodes on either side of the large surfaces with the boundary perpendicular to the measurement direction, an equivalent electric circuit for this analysis is shown in Figure 2.8.

7.2.1 Undoped $\Sigma 5$ and 6° symmetric tilt boundaries

In Figure 7.9 impedance spectra obtained for $\Sigma 5$ and 6° tilt boundaries at 550°C under 1 bar of oxygen are presented. In each case, the spectrum consists two semicircles at high (HF) and low frequencies (LF) in contrary to a single crystal with only a HF semicircle. Based on the capacitance (10^{-11} F) and the relative permittivity ($\epsilon_r = 55$), the HF semicircle was assigned unambiguously to the bulk response. The LF semicircle has a lower capacitance (10^{-7} F) than expected for a bicrystal ($\sim 10^{-6}$ F). Therefore, it is not clear from EIS data whether the LF response correspond to GB or current constriction effects [81]. For brevity, this semicircle will be represented as ' σ_{LF} ' and a possible distinction will be made later in Section 7.2.4.

By fitting impedance spectra acquired at various $p\text{O}_2$, the bulk and LF conductivities are calculated based on the sample geometry (according to Equations (3.1) and (3.2)) and plotted as function of $p\text{O}_2$ in Figure 7.10. The bulk conductivity of bicrystals is compared with the single crystals used for synthesizing bicrystals and the same $p\text{O}_2$ dependency is found. This comparison provides a preliminary information of contamination (impurities acting as dopants) or artifacts (e.g. dislocations in bulk) that may arise during diffusion bonding (such effects could lead to variation in the bulk conductivity). The $p\text{O}_2$ exponent, $m = +1/4$ at high $p\text{O}_2$ and $-1/4$ at low $p\text{O}_2$ and $-1/6$ at very low $p\text{O}_2$ is in agreement with the bulk defect chemistry of TiO_2 (Section 2.3). Interestingly, there is no significant changes observed in the σ_{LF} conductivity of $\Sigma 5$ and 6° tilt boundaries and both have the same $p\text{O}_2$ exponent ($m=+1/4$) at high $p\text{O}_2$. At very low $p\text{O}_2$, like in other samples discussed in this work, only a total resistance is extractable due to inductive type loops in impedance spectra.

In Figure 7.11 the electrical conductivity of the bulk and the effective conductivity calculated from the LF semicircle (σ_{LF}) are plotted as a function of temperature. The activation energy of ~ 1 eV for the bulk conductivity is comparable with other

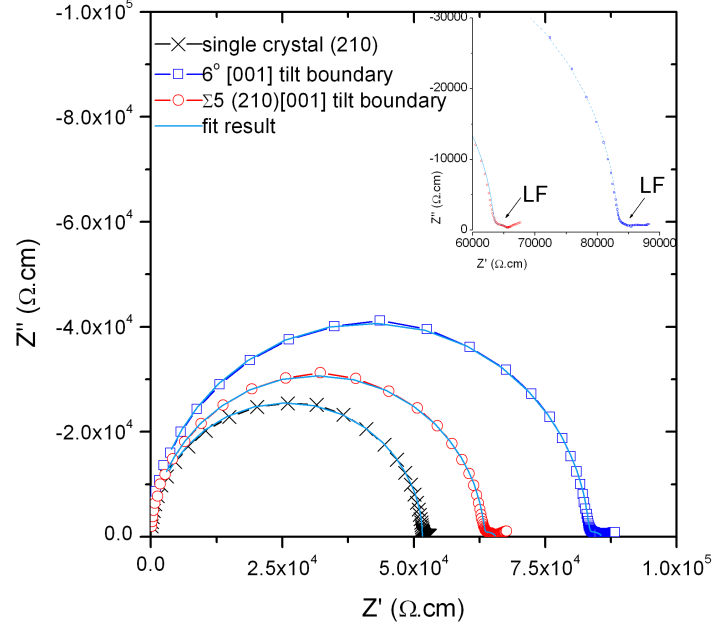


Figure 7.9: Impedance spectra for undoped $\Sigma 5$ and 6° symmetric tilt boundary of TiO_2 bicrystals, (210) single crystal data is also shown for comparison, the ideality factor for fitting are $\psi_{HF}=0.99$ and $\psi_{LF}=0.6$. Data is normalized over sample geometry.

single crystalline and polycrystalline samples measured in this work (Chapter 4 and 5). The reproducibility of the bulk conductivity data for the various bicrystals is remarkable. The activation energy for σ_{LF} is very similar for both special boundaries, and is slightly higher than for the bulk conductivity. Even though this points towards a resistive GB ruling out a pure current constriction, however, the reasons for the observed low capacitance value in EIS are not clear. It is possible that this results from a combination of both effects similar to the CS sample discussed in Chapter 5.

7.2.2 Y-decorated $\Sigma 5$ symmetric tilt boundary

In Y-decorated $\Sigma 5$ boundary samples ($\Sigma 5$ -1nm Y) approximately 1 nm of Y_2O_3 is placed in the boundary (prior to bonding) which roughly correspond to 1-2 monolayers of Y_2O_3 . Figure 7.12 shows the impedance spectra of $\Sigma 5$ undoped and $\Sigma 5$ -1nm Y bicrystals. Based on the relative permittivity value ($\epsilon_r=55$, $C_{HF}=10^{-11}$ F) the HF

7. SYMMETRIC TILT BOUNDARIES

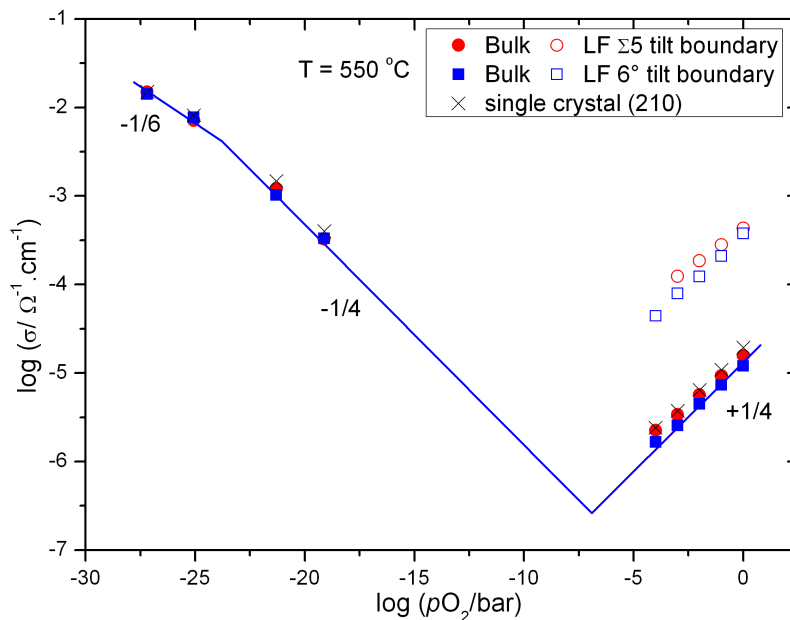


Figure 7.10: Electrical conductivity as a function of $p\text{O}_2$ for undoped $\Sigma 5$ and 6° symmetric tilt boundary TiO_2 bicrystals, single crystal data are also shown for comparison.

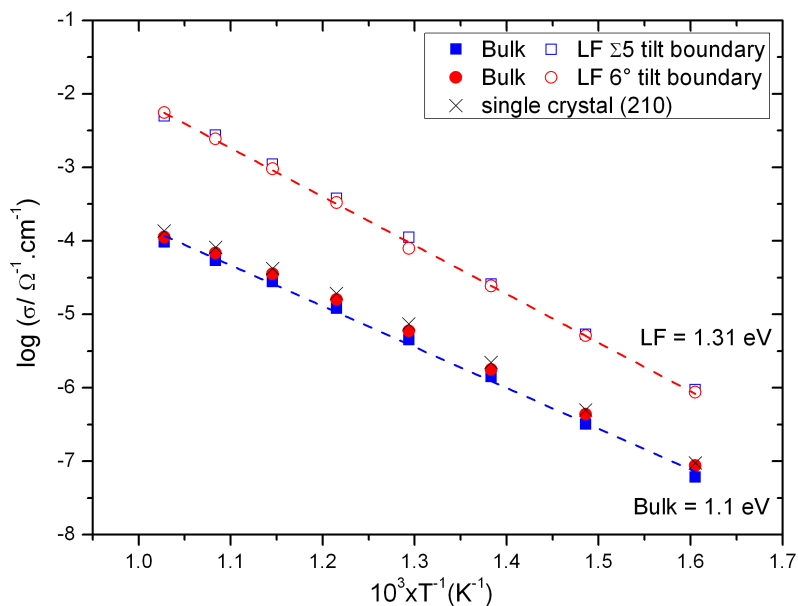


Figure 7.11: Arrhenius plot for undoped $\Sigma 5$ and 6° symmetric tilt boundary of TiO_2 bicrystals, single crystal data are also shown for comparison.

semicircle is assigned to the bulk response and the LF to the GB/current constriction effect (a lower capacitance value similar to undoped bicrystals was observed).

Figure 7.13 present the electrical conductivity of $\Sigma 5$ undoped and $\Sigma 5$ -1nm Y bicrys-

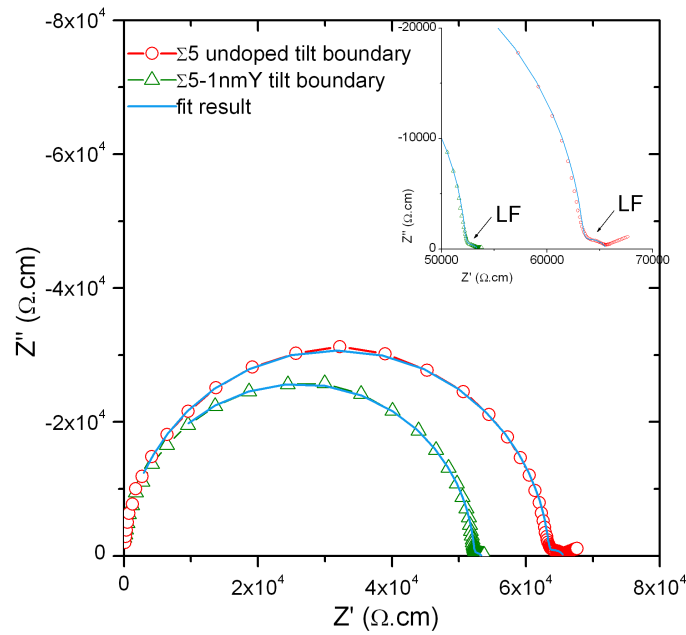


Figure 7.12: Impedance spectra for Y-decorated $\Sigma 5$ symmetric tilt boundary of TiO_2 bicrystal, the ideality factor for fitting are $\psi_{HF}=0.99$ and $\psi_{LF}=0.6$.

tals as a function of $p\text{O}_2$ at $550\text{ }^\circ\text{C}$. It is very evident from the figure that there is no influence of acceptor dopant on the bulk conductivity of the decorated sample. This is consistent with the majority of the dopant concentration being retained at the GB. Both samples show a p-type conductivity at high $p\text{O}_2$ and n-type conductivity at low $p\text{O}_2$. The results are in good agreement with the previous measurements on TiO_2 single crystals discussed in this thesis. The LF conductivity as a function of $p\text{O}_2$ is also same for both the samples. Figure 7.14 shows the Arrhenius plot for the bulk and LF conductivity, again a perfect match is observed with the bulk and LF conductivities. A higher activation energy for LF conductivity is observed compared to the bulk conductivity.

7. SYMMETRIC TILT BOUNDARIES

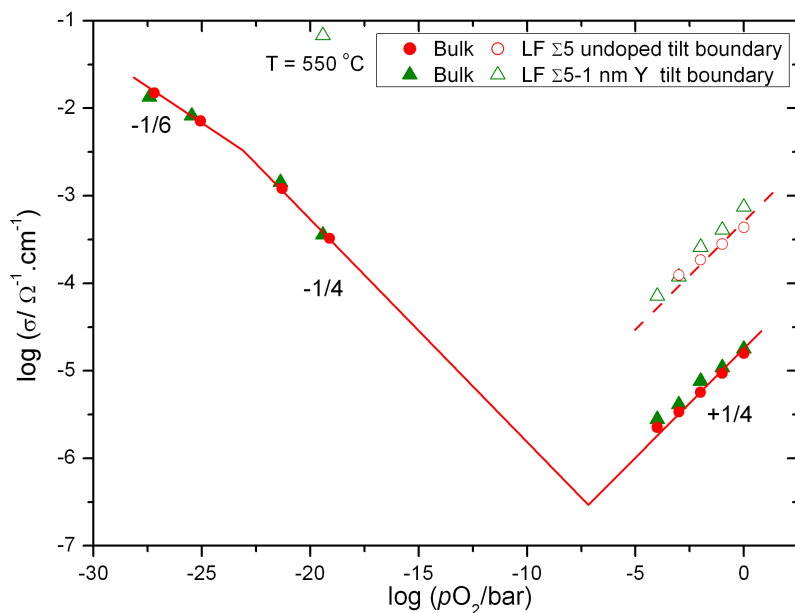


Figure 7.13: Electrical conductivity as a function of $p\text{O}_2$ for Y-decorated and undoped $\Sigma 5$ symmetric tilt boundary of TiO_2 bicrystals.

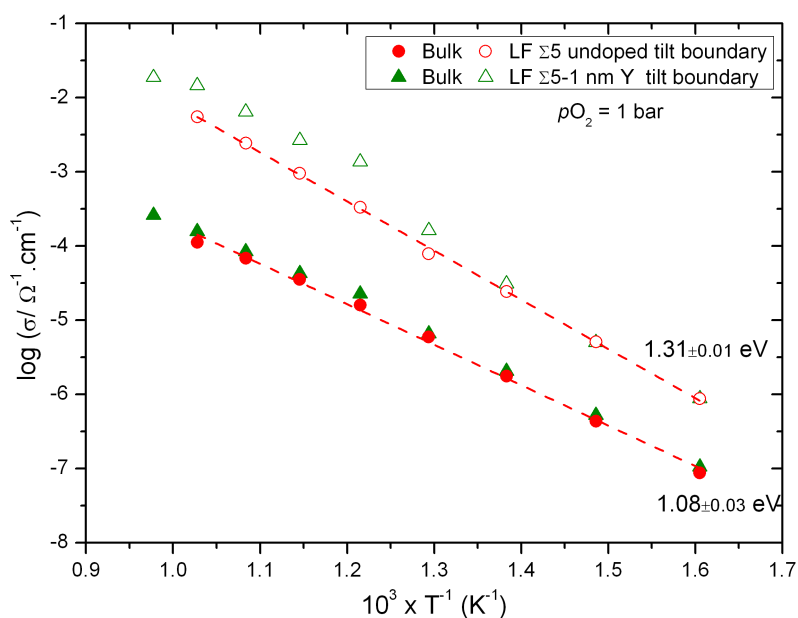


Figure 7.14: Arrhenius plot for undoped and Y-decorated $\Sigma 5$ symmetric tilt boundary TiO_2 bicrystals.

7.2.3 Y-decorated 3° symmetric tilt boundary

In Figure 7.15 impedance spectra of the undoped and Y-decorated 6° tilt boundary TiO₂ bicrystals at 550 °C in 1 bar pO_2 is presented. Similar to the analysis for the undoped bicrystal, the HF semicircle corresponds to the bulk ($\varepsilon_r = 70$, $C_{HF} = 10^{-11}F$) and the LF arc is ambiguous based on its low capacitance ($10^{-8} F$) to be assigned to GB. The conductivity data of the bulk and σ_{LF} at 550 °C is plotted as a function of pO_2 in Figure 7.16. A good match in the bulk conductivity of both samples indicates that there is no influence of acceptor dopant. A perfect match is also observed for σ_{LF} data, indicating no changes in the boundary conductivity or constriction effect. Figure 7.17 shows the activation energy for bulk conductivity and σ_{LF} (very similar to other bicrystals) with slightly higher activation energy for σ_{LF} .

To summarize the electrical characterization section, it was observed that there

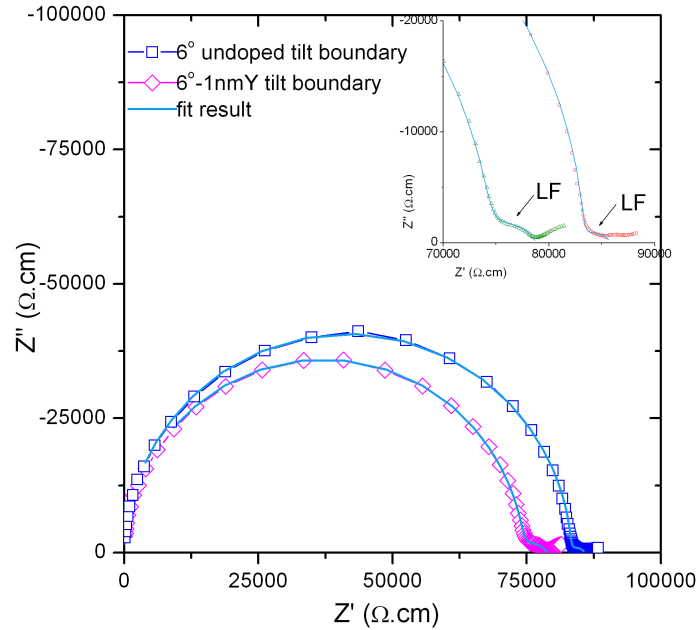


Figure 7.15: Impedance spectra for Y-decorated 6° symmetric tilt boundary of TiO₂ bicrystal, the ideality factor for fitting are $\psi_{HF}=0.99$ and $\psi_{LF}=0.6$.

were no changes in the electrical properties and their pO_2 dependence. The bulk conductivities of all samples are in good agreement with the bulk defect chemistry of TiO₂. There is no influence of acceptor decoration either on the bulk or σ_{LF}

7. SYMMETRIC TILT BOUNDARIES

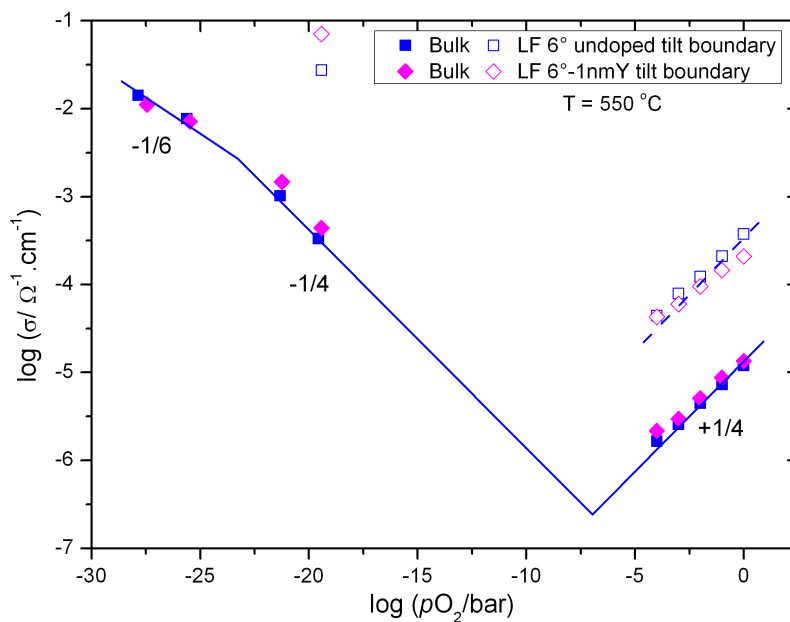


Figure 7.16: Electrical conductivity as a function of $p\text{O}_2$ for Y-decorated and undoped 6° symmetric tilt boundary of TiO_2 bicrystals.

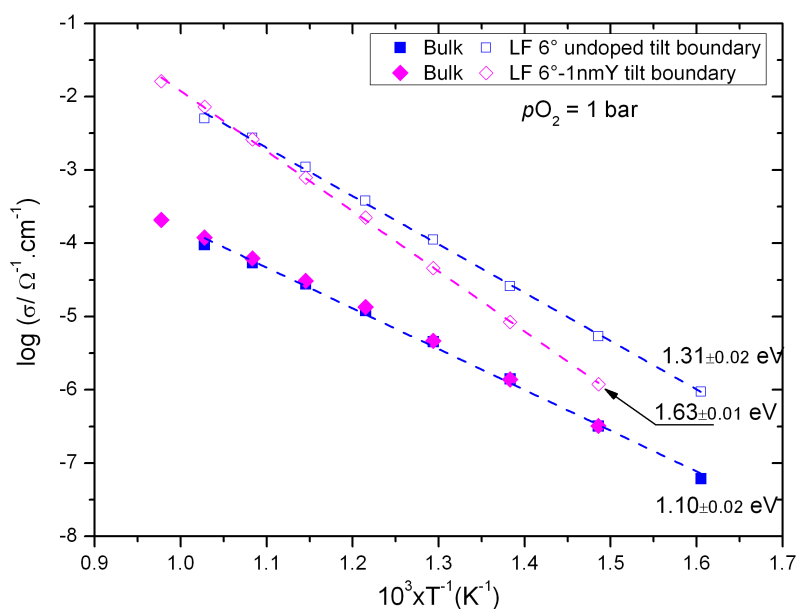


Figure 7.17: Arrhenius plot for undoped and Y-decorated 6° symmetric tilt boundary of TiO_2 bicrystals.

conductivity as a function of pO_2 . A slight increase in activation energy of LF conductivity is observed in the presence of Y decoration pointing towards blocking GB. Therefore, assigning the LF data either to blocking GB or current constriction is ambiguous and is discussed in the next section.

7.2.4 Discussion

In order to resolve the LF process more clearly, the $\Sigma 5$ bicrystal was thinned from both sides to an overall thickness of ~ 0.2 mm. The effect of sample thickness on the electrical conductivity is shown in Figure 7.18 for a $\Sigma 5$ 0.5 nm Y-decorated boundary at 450 °C under 1 bar pO_2 . There is no change in the LF semicircle (unchanged resistance and capacitance) on decrease of the sample thickness from 1 mm to 0.19 mm (\sim factor 5). The fit parameters for both the samples before and after the thickness reduction is given in Table 7.1. Insignificant change in σ_{LF} with the thickness reduction can be interpreted either as the GB resistance due to space charge effects (blocking boundaries for hole conduction) or current constriction.

Since current constriction effects arise from bulk conductivity being restricted to a

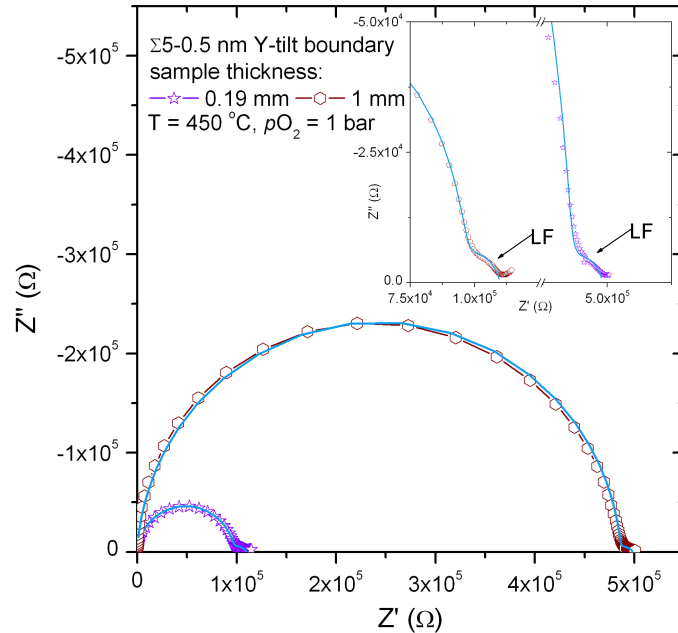


Figure 7.18: Impedance spectra for $\Sigma 5$ Y decorated tilt boundary sample before and after thickness reduction.

7. SYMMETRIC TILT BOUNDARIES

	thickness =1 mm		thickness =0.19 mm	
	HF (bulk)	LF	HF (bulk)	LF
R (Ω)	485000	12781	96001	14076
σ ($\Omega^{-1}.cm^{-1}$)	1.23×10^{-6}		1.17×10^{-6}	
ψ	0.97	0.7	0.97	0.7
Q (F)	1.7×10^{-11}	1.6×10^{-6}	5.5×10^{-11}	3.2×10^{-7}

Table 7.1: Fit results for Figure 7.18 from Z-View software.

smaller area at grain-to-grain contact (e.g. due to pores or second phase), they are considered to be only very weakly dependent of applied bias voltage (see e.g. [140]). On the other hand, the effect of space charge zones are strongly dependent on the bias voltage. Typically conductivity increases with increasing DC bias voltage [91, 141]. Therefore, the space charge effect can be distinguished from current constriction by application of a DC bias voltage. In Figure 7.19 the effect of DC bias on the impedance spectra of mechanically thinned (0.2 mm) $\Sigma 5$ undoped boundary at 450 °C and 1 bar pO_2 is presented. An increase of DC bias resulted in shrinkage of HF semicircle at bias ≥ 0.4 V and only slight changes of the LF semicircle. The conductivity data of the bulk and LF are presented as inset in the same figure. A largely bias-independent σ_{LF} point towards a constriction effect rather than a space charge effect. On the other hand it must be considered that even after decreasing the thickness of the bicrystal most of the applied bias drops over the bulk resistance (since $R_{HF} \gg R_{LF}$), and that the distorted shape of the LF semicircle makes its quantification less reliable. The variation in the bulk conductivity on increased bias voltage can be related to the stoichiometric polarization of slightly irreversible Pt-paste electrodes. Similar experiments on [001] oriented TiO_2 single crystal also revealed a bias dependent bulk conductivity as shown in Figure 7.19b.

The LF contribution is therefore considered to be mainly due to current constriction effects in TiO_2 bicrystals. The very localized (small area) inspection in TEM could be the reason for not having observing a significant pores in the sample. So far, optical inspection of the TEM specimens revealed only a few pores that are distantly spaced, see Figure 7.2. On the other hand, the electrical conductivity (DC bias) averages over the whole sample. While the increase activation energy of σ_{LF} points towards some space charge depletion at the GB in the bicrystals, the absence of

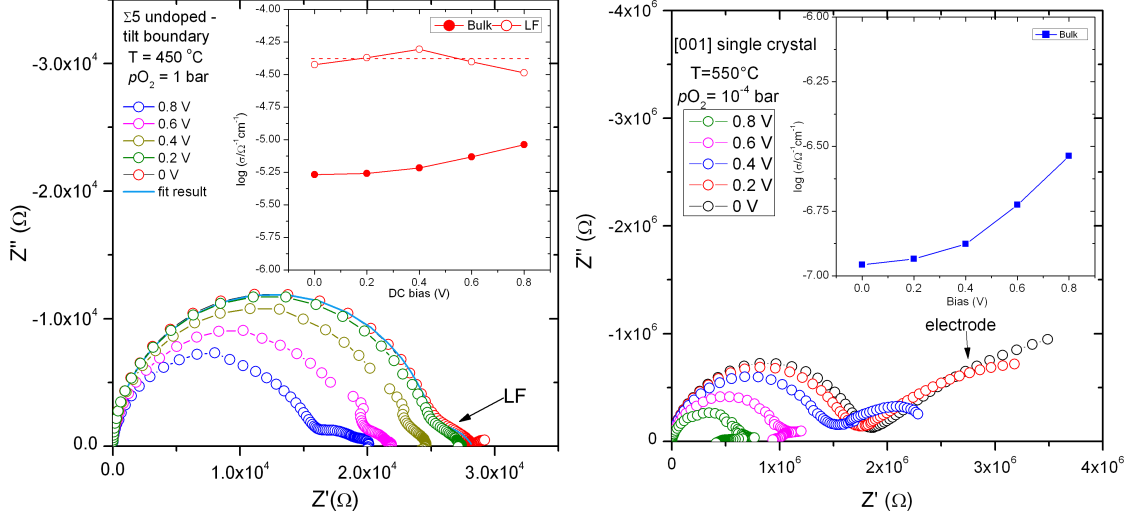


Figure 7.19: Impedance spectra for $\Sigma 5$ undoped tilt boundary and [001] single crystal under an applied DC bias of 0 V to 0.8 V, inset shows the plot for electrical conductivity as a function of DC bias. Each spectra was collected at an interval of 30 min.

a strong bias dependence of σ_{LF} rather indicates that current constriction makes a significant contribution to the blocking behavior of the GB. It should also be noted that the bicrystal GB studied here are less blocking than the bicrystal GB in SrTiO_3 [21, 124].

7.3 Chapter conclusions

In summary, TEM on $\Sigma 5$ and 6° symmetric tilt boundaries of TiO_2 bicrystals revealed that the 2-D boundary is a result of periodic arrangement of 1-D defects (dislocations). Dislocations in the low angle tilt boundary (6°) are closely spaced at an interval of 3.8 nm, due to higher tilt angle and boundary symmetry $\Sigma 5$ boundary does not have such closely spaced dislocations. Both crystals have distantly spaced dislocations due to varying twist in the crystal alignment, prior to the diffusion bonding. The symmetric tilt boundaries have the same bulk and interface electrical properties, exhibiting a LF semicircle at high $p\text{O}_2$, but with a very small resistance compared to the bulk value (i.e. the GB's are very weakly blocking for positive charge carriers such as holes). Hence, acceptor decoration (effectively nega-

7. SYMMETRIC TILT BOUNDARIES

tive charge) in the GB also did not result in any change of the electrical properties. It is concluded that the interface electrical properties are largely determined by current constriction effects rather than space charge effects. Therefore, it can be concluded that low angle and symmetric tilt boundaries in TiO_2 have no or only a very minor excess positively charged, which is in contrast to the observation in other wide band gap oxides such as SrTiO_3 , YSZ and CeO_2 [13, 89–91] (which, however, have crystal structures different from Rutile).

8

Summary

The influence of extended defects on the electrical properties of TiO_2 (rutile) is studied in this work. Two main types of extended defects (dislocations and grain boundaries) that are commonly observed in crystalline solids are discussed.

Dislocations in single crystals and polycrystalline TiO_2 are generated based on the creep deformation maps of TiO_2 . With the help of TEM it is observed that dislocations preferably form on $\{110\}$ planes, hence electrical properties are characterized parallel to $\{110\}$ planes (i.e. along $[001]$) and perpendicular to $\{110\}$ planes (i.e. $[110]$), i.e., parallel and perpendicular to the dislocations. Increased electrical conductivity was observed in $[001]$ (electrical measurement axis) samples, with the enhancement being a function of dislocation density. At high $p\text{O}_2$, the increase in dislocation density resulted in enhanced conductivity from positively charged carriers in $[001]$ samples. In contrary, no changes in the electrical properties were observed in case of $[110]$ samples. The reasons for enhanced ionic and hole conductivity in $[001]$ and absence of changes in $[110]$ samples is rationalized in the framework of a percolating network of dislocations with negatively charged core (most probably accumulated $V_{\text{Ti}}^{\prime\prime\prime}$ in the core) and adjacent space charge accumulation zones. The space charge model is supported by the fact that the concentration of ionic defects steeply raised over electronic defects in the following sequence $\text{Ti}_i^{\bullet\bullet\bullet} > V_{\text{O}}^{\bullet\bullet} > h^{\bullet}$ according to their higher charge. The absence of such a network in $[110]$ samples explains the unchanged conductivity in these samples. At low $p\text{O}_2$, the n-type bulk conductivity is so high that predominates over the space charge zones with electron

8. SUMMARY

depletion (which, however, do not sufficiently overlap to block the current). Hence, no changes in the electrical properties were observed at low pO_2 .

In continuation to the work on single crystals, dislocations were created in polycrystalline ceramics by spark plasma sintering at high temperature and pressures. TEM revealed that dislocations are formed only in larger grains, grains smaller than 100 nm are free from dislocations. This observation is in agreement with the creep deformation map of TiO_2 , where a decrease in grain size increases the strength of the material. Dislocations in TiO_2 ceramics changed the defect chemistry at high pO_2 from predominant hole conductivity to ionic conductivity. Hebb-Wagner type polarization measurements indicated an ionic transference number of 0.7 at 10^{-3} to 1 bar pO_2 . The equivalent trivalent acceptor concentration required to achieve such an enhancement in the homogeneous bulk would be 0.5 mol% - which would usually be unattainable by chemical acceptor doping especially for dopants of larger ionic radii. However, compared to single crystals the total conductivity enhancement is lower in polycrystalline TiO_2 due to varying dislocation density from a randomly oriented grains with respect to the compression axis and part of creep is accommodated by grain boundaries further increasing the strength of the material.

The influence of acceptor dopants on the dislocation formation (and thereby electrical properties) were investigated for 0.1 mol % Y homogeneously doped or selectively GB decorated samples. Homogeneous doping suppressed the dislocation generation by solid solution strengthening. In absence of dislocations, the electrical properties of these samples match exactly with conventionally sintered samples without any dislocations. On other hand, decorated samples have dislocations that are very similar to undoped TiO_2 ceramics, hence the defect chemistry of these samples are comparable to the undoped sample with dislocations. (predominant ionic conductivity due to a percolating network of negatively charged dislocation and space charge accumulation zone at high pO_2).

In the second part of this thesis, 2-D planar defects were created by diffusion bonding TiO_2 single crystals to bicrystals with well defined symmetric tilt boundaries. High-resolution TEM revealed that a slight twist in the crystal alignment is

accommodated by periodical dislocations, whose spacing is inversely proportional to the misorientation angle. The low angle tilt boundary (6°) bicrystals have dislocations that are closely spaced with a distance of 3.8 nm, which is agreement with the Frank's rule for dislocation spacing. The $\Sigma 5$ boundary does not have such closely spaced dislocations, as expected for a well ordered CSL (coincident site lattice) boundary. All the bicrystals, irrespective of the boundary orientation, showed similar electrical properties for the bulk (high frequency contribution in EIS) and the interface (low frequency contribution in EIS). Based on the DC bias experiments, it is concluded that the observed LF contribution in EIS is due to current constriction effects rather than space charge effects. A comparison of the electrical properties of all samples indicates the boundaries are not blocking for the positively charged defects at high pO_2 (unlike in other wide band gap oxides, such as $SrTiO_3$, ZrO_2). This suggests that TiO_2 symmetric tilt boundaries are either almost neutral or negatively charged due to dislocations. The latter could well be plausible from the results of Part-I of this thesis.

These results on extended defects, indicate that dislocations can be used as an option for modifying electrical properties of TiO_2 . With the possibility to form dislocations by local interaction (e.g. indentation experiments), one can imagine to spatially modify point defect concentrations (long-time persistent at moderate temperatures) which would not be possible with the usual chemical doping approach. Such a defect-chemical structuring by locally increasing ionic and electronic carrier concentrations, even changing the material from predominant electronic to ionic conduction, may become relevant in fields such as information storage or catalysis. A recent work by Cha et al. [142] showed that TiO_2 (rutile) with dislocations in [001] improved the photocatalytic activity compared to conventionally used P25 nano anatase particles. These findings are in line with this thesis, that extended defects especially dislocations, can be viewed as an electrochemically active regions where high concentrations of electronic and ionic defects are expected.

A further extension of this present work to $SrTiO_3$ single crystals revealed that there the dislocations formed by uniaxial compression are positively charged and therefore deplete the positive carriers in the space charge zones (a perfect counter

8. SUMMARY

example to TiO_2). However, a striking finding on these crystals, very similar to TiO_2 , is the enhancement of ionic conductivity at high $p\text{O}_2$ (1 bar to 10^{-5} bar). Comparing and contrasting these two ionic solids, it seem promising that this technique can be utilized to tune ionic/electronic conductivities for a number of materials and electrochemical devices in future as an alternative to zero-dimensional doping (homogeneous doping by dissolving dopants) and two-dimensional doping (heterogeneous doping by introducing interfaces).

References

- [1] A. Trenczek-Zajac and M. Rekas. Electrical properties of Nb-doped titanium dioxide TiO_2 at room temperature. *Materials Science-Poland*, 24(1):53, 2006.
- [2] L. Xu, M. P. Garrett, and B. Hu. Doping effects on internally coupled seebeck coefficient, electrical, and thermal conductivities in aluminum-doped TiO_2 . *Journal Of Physical Chemistry C*, 116(24):13020, 2012.
- [3] D. K. Lee and H. I. Yoo. Electrical conductivity and oxygen nonstoichiometry of acceptor (Ga)-doped titania. *Physical Chemistry Chemical Physics*, 10:6890, 2008.
- [4] Q. L. Wang, G. Lian, and E. C. Dickey. Grain boundary segregation in yttrium-doped polycrystalline TiO_2 . *Acta Materialia*, 52(4):809, 2004.
- [5] J. Maier. Ionic-conduction in-space charge regions. *Progress in Solid State Chemistry*, 23(3):171, 1995.
- [6] C. C. Liang. Conduction characteristics of lithium iodide aluminum oxide solid electrolytes. *Journal of the Electrochemical Society*, 120(10):1289, 1973.
- [7] K. Shahi and J. B. Wagner. Fast ion-transport in silver-halide solid-solutions and multiphase systems. *Applied Physics Letters*, 37(8):757, 1980.
- [8] J. Maier. Space-charge regions in solid 2-phase systems and their conduction contribution .1. conductance enhancement in the system ionic conductor-inert phase and application on $\text{AgCl-Al}_2\text{O}_3$ and AgCl-SiO_2 . *Journal Of Physics And Chemistry Of Solids*, 46(3):309, 1985.
- [9] N. Sata, K. Eberman, K. Eberl, and J. Maier. Mesoscopic fast ion conduction in nanometre-scale planar heterostructures. *Nature*, 408(6815):946, 2000.

REFERENCES

- [10] J. Maier. Nanoionics: Ion transport and electrochemical storage in confined systems. *Nature Materials*, 4(11):805, 2005.
- [11] J. Maier. Nanoionics: Ionic charge carriers in small systems. *Physical Chemistry Chemical Physics*, 11(17):3011, 2009.
- [12] P. Lupetin, G. Gregori, and J. Maier. Mesoscopic charge carriers chemistry in nanocrystalline SrTiO₃. *Angewandte Chemie-International Edition*, 49(52):10123, 2010.
- [13] S. Kim and J. Maier. On the conductivity mechanism of nanocrystalline ceria. *Journal Of The Electrochemical Society*, 149(10):J73, 2002.
- [14] Y. M. Chiang, E. B. Lavik, I. Kosacki, H. L. Tuller, and J. Y. Ying. Defect and transport properties of nanocrystalline CeO_{2-x}. *Applied Physics Letters*, 69(2):185, 1996.
- [15] Y. M. Chiang, E. B. Lavik, I. Kosacki, H. L. Tuller, and J. Y. Ying. Nonstoichiometry and electrical conductivity of nanocrystalline CeO_{2-x}. *Journal Of Electroceramics*, 1(1):7, 1997.
- [16] P. Knauth and H. L. Tuller. Electrical and defect thermodynamic properties of nanocrystalline titanium dioxide. *Journal Of Applied Physics*, 85(2):897, 1999.
- [17] A. Kushima and B. Yildiz. Oxygen ion diffusivity in strained yttria stabilized zirconia: Where is the fastest strain? *Journal of Materials Chemistry*, 20(23):4809, 2010.
- [18] J. C. Lewis, J. McCardle, and R. W. Whitworth. Evidence for glide of charged dislocations on (111) planes in NaCl-crystals. *Physica Status Solidi a-Applied Research*, 64(1):K67, 1981.
- [19] R. W. Whitworth. Charged dislocations in ionic-crystals. *Advances in Physics*, 24(2):203, 1975.
- [20] V. F. Petrenko and R. W. Whitworth. Charged dislocations and the plastic-deformation of II-VI compounds. *Philosophical Magazine a-Physics of Condensed Matter Structure Defects and Mechanical Properties*, 41(5):681, 1980.

REFERENCES

- [21] R. A. De Souza, J. Fleig, J. Maier, Z. L. Zhang, W. Sigle, and M. Rühle. Electrical resistance of low-angle tilt grain boundaries in acceptor-doped SrTiO₃ as a function of misorientation angle. *Journal Of Applied Physics*, 97(5), 2005.
- [22] C. L. Jia and K. Urban. Atomic-resolution measurement of oxygen concentration in oxide materials. *Science*, 303(5666):2001, 2004.
- [23] C. Korte, A. Peters, J. Janek, D. Hesse, and N. Zakharov. Ionic conductivity and activation energy for oxygen ion transport in superlattices - the semicoherent multilayer system YSZ (ZrO₂ + 9.5 mol % Y₂O₃)/Y₂O₃. *Physical Chemistry Chemical Physics*, 10(31):4623, 2008.
- [24] N. Schichtel, C. Korte, D. Hesse, and J. Janek. Elastic strain at interfaces and its influence on ionic conductivity in nanoscaled solid electrolyte thin films-theoretical considerations and experimental studies. *Physical Chemistry Chemical Physics*, 11(17):3043, 2009.
- [25] R. A. De Souza, A. Ramadan, and S. Hoerner. Modifying the barriers for oxygen-vacancy migration in fluorite-structured CeO₂ electrolytes through strain: A computer simulation study. *Energy & Environmental Science*, 5(1):5445, 2012.
- [26] D. K. Lee and H. I. Yoo. Unusual oxygen re-equilibration kinetics of TiO_{2-δ}. *Solid State Ionics*, 177(1-2):1, 2006.
- [27] J. F. Marucco, J. Gautron, and P. Lemasson. Thermogravimetric and electrical study of nonstoichiometric titanium-dioxide TiO_{2-x} between 800 and 1100 °C. *Journal Of Physics And Chemistry Of Solids*, 42(5):363, 1981.
- [28] R. T. Dirstine and C. J. Rosa. Defect structure and related thermodynamic properties of nonstoichiometric rutile (TiO_{2-x}) and Nb₂O₅ doped rutile: 1. defect structure of TiO_{2-x} (rutile) and partial molar properties for oxygen solution at 1273 k. *Zeitschrift Fur Metallkunde*, 70(5):322, 1979.
- [29] R. N. Blumenthal, J. Baukus, and W. M. Hirthe. Studies of defect structure of nonstoichiometric rutile TiO_{2-x}. *Journal of the Electrochemical Society*, 114(2P1):172, 1967.
- [30] J. F. Baumard. Chemical diffusivity of oxygen in oxygen deficient rutile for compositions close to TiO₂. *Solid State Communications*, 20(9):859, 1976.

REFERENCES

- [31] J. Sasaki, N. L. Peterson, and K. Hoshino. Tracer impurity diffusion in single-crystal rutile TiO_{2-x} . *Journal Of Physics And Chemistry Of Solids*, 46(11):1267, 1985.
- [32] P. Kofstad. Thermogravimetric studies of defect structure of rutile TiO_2 . *Journal Of Physics And Chemistry Of Solids*, 23(11):1579, 1962.
- [33] K. S. Forland. Defect structure of rutile. *Acta Chemica Scandinavica*, 18(5):1267, 1964.
- [34] U. Balachandran and N. G. Eror. Electrical-conductivity in non-stoichiometric titanium-dioxide at elevated-temperatures. *Journal Of Materials Science*, 23(8):2676, 1988.
- [35] E. H. Greener, F. J. Barone, and W. M. Hirthe. Electrical conductivity of single and polycrystalline near-stoichiometric rutile in range 600° to 1400° C. *Journal Of The American Ceramic Society*, 48(12):623, 1965.
- [36] T. Bak, J. Nowotny, M. Rekas, and C. C. Sorrell. Defect chemistry and semiconducting properties of titanium dioxide: II. defect diagrams. *Journal Of Physics And Chemistry Of Solids*, 64(7):1057, 2003.
- [37] M. K. Nowotny, T. Bak, and J. Nowotny. Electrical properties and defect chemistry of TiO_2 single crystal. I. electrical conductivity. *Journal of physical chemistry. B*, 110(33):16270, 2006.
- [38] M. K. Nowotny, L. R. Sheppard, T. Bak, and J. Nowotny. Defect chemistry of titanium dioxide. application of defect engineering in processing of TiO_2 -based photocatalysts. *Journal Of Physical Chemistry C*, 112(14):5275, 2008.
- [39] W. M. Hirthe and J. O. Brittain. Dislocations in rutile as revealed by the etch-pit technique. *Journal Of The American Ceramic Society*, 45(11):546, 1962.
- [40] W. M. Hirthe and J. O. Brittain. High-temperature steady-state creep in rutile. *Journal Of The American Ceramic Society*, 46(9):411, 1963.
- [41] K. H. G. Ashbee and R. E. Smallman. Stress-strain behavior of titanium dioxide (rutile) single crystals. *Journal Of The American Ceramic Society*, 46(5):211, 1963.
- [42] L. A. Bursill, M. G. Blanchin, A. Mebarek, and D. J. Smith. Point, linear and extended defect structures in nonstoichiometric rutile. *Radiation Effects and Defects in Solids*, 74(1-4):253, 1983.

REFERENCES

- [43] L. A. Bursill and M. G. Blanchin. Resolution of atomic steps on dislocations in rutile. *Philosophical Magazine a-Physics of Condensed Matter Structure Defects and Mechanical Properties*, 49(3):365, 1984.
- [44] Y. Motohashi, M. G. Blanchin, E. Vicario, G. Fontaine, and S. Otake. Elastic parameters, elastic energy, and stress-fields of dislocations in TiO₂ rutile crystals. *Physica Status Solidi a-Applied Research*, 54(1):355, 1979.
- [45] M. G. Blanchin and G. Fontaine. Transmission electron-microscope observations of deformed rutile (TiO₂). *Physica Status Solidi a-Applied Research*, 29(2):491, 1975.
- [46] P. Y. Simons and F. Dache. Structure of TiO₂ II, a high-pressure phase of TiO₂. *Acta Crystallographica*, 23:334, 1967.
- [47] J. Akimoto, Y. Gotoh, Y. Oosawa, N. Nonose, T. Kumagai, K. Aoki, and H. Takei. Topotactic oxidation of ramsdellite-type Li_{0.5}TiO₂, a new polymorph of titanium-dioxide: TiO₂(r). *Journal Of Solid State Chemistry*, 113(1):27, 1994.
- [48] H. Sato, S. Endo, M. Sugiyama, T. Kikegawa, O. Shimomura, and K. Kusaba. Baddeleyite-type high-pressure phase of TiO₂. *Science*, 251(4995):786, 1991.
- [49] R. Marchand, L. Brohan, and M. Tournoux. TiO₂(b) a new form of titanium-dioxide and the potassium octatitanate K₂Ti₈O₁₇. *Materials Research Bulletin*, 15(8):1129, 1980.
- [50] L. Kavan, M. Gratzel, S. E. Gilbert, C. Klemenz, and H. J. Scheel. Electrochemical and photoelectrochemical investigation of single-crystal anatase. *Journal of the American Chemical Society*, 118(28):6716, 1996.
- [51] I. Exnar, L. Kavan, S. Y. Huang, and M. Gratzel. Novel 2 V rocking-chair lithium battery based on nano-crystalline titanium dioxide. *Journal of Power Sources*, 68(2):720, 1997.
- [52] J. Muscat, V. Swamy, and N. M. Harrison. First-principles calculations of the phase stability of TiO₂. *Physical Review B*, 65(22), 2002.
- [53] P. Balaya and J. Maier. Thermodynamics of nano- and macrocrystalline anatase using cell voltage measurements. *Physical Chemistry Chemical Physics*, 12(1):215, 2010.

REFERENCES

- [54] M. R. Ranade, A. Navrotsky, H. Z. Zhang, J. F. Banfield, S. H. Elder, A. Zaban, P. H. Borse, S. K. Kulkarni, G. S. Doran, and H. J. Whitfield. Energetics of nanocrystalline TiO₂. *Proceedings of the National Academy of Sciences of the United States of America*, 99:6476, 2002.
- [55] A. S. Barnard and P. Zapol. Predicting the energetics, phase stability, and morphology evolution of faceted and spherical anatase nanocrystals. *Journal Of Physical Chemistry B*, 108(48):18435, 2004.
- [56] D. T. Cromer and K. Herrington. The structures of anatase and rutile. *Journal of the American Chemical Society*, 77(18):4708, 1955.
- [57] P. V. Kamat. TiO₂ nanostructures: Recent physical chemistry advances. *The Journal of Physical Chemistry C*, 116(22):11849, 2012.
- [58] A. Fujishima and K. Honda. Electrochemical photolysis of water at a semiconductor electrode. *Nature*, 238(5358):37, 1972.
- [59] O. Carp, C. L. Huisman, and A. Reller. Photoinduced reactivity of titanium dioxide. *Progress in Solid State Chemistry*, 32(1-2):33, 2004.
- [60] C. J. Barbe, F. Arendse, P. Comte, M. Jirousek, F. Lenzmann, V. Shklover, and M. Gratzel. Nanocrystalline titanium oxide electrodes for photovoltaic applications. *Journal of the American Ceramic Society*, 80(12):3157, 1997.
- [61] B. O'Regan and M. Gratzel. A low-cost, high-efficiency solar-cell based on dye-sensitized colloidal TiO₂ films. *Nature*, 353(6346):737, 1991.
- [62] J. J. Yang, M. D. Pickett, X. Li, D. A. A. Ohlberg, D. R. Stewart, and R. S. Williams. Memristive switching mechanism for metal/oxide/metal nanodevices. *Nature Nanotechnology*, 3(7):429, 2008.
- [63] B. J. Choi, D. S. Jeong, S. K. Kim, C. Rohde, S. Choi, J. H. Oh, H. J. Kim, C. S. Hwang, K. Szot, R. Waser, B. Reichenberg, and S. Tiedke. Resistive switching mechanism of TiO₂ thin films grown by atomic-layer deposition. *Journal Of Applied Physics*, 98(3):033715, 2005.
- [64] L. D. Birkefeld, A. M. Azad, and S. A. Akbar. Carbon-monoxide and hydrogen detection by anatase modification of titanium-dioxide. *Journal Of The American Ceramic Society*, 75(11):2964, 1992.

REFERENCES

- [65] Y. S. Hu, L. Kienle, Y. G. Guo, and J. Maier. High lithium electroactivity of nanometer-sized rutile TiO_2 . *Advanced Materials*, 18(11):1421, 2006.
- [66] H. Xiong, M. D. Slater, M. Balasubramanian, C. S. Johnson, and T. Rajh. Amorphous TiO_2 nanotube anode for rechargeable sodium ion batteries. *Journal of Physical Chemistry Letters*, 2(20):2560, 2011.
- [67] B. H. Park, L. S. Li, B. J. Gibbons, J. Y. Huang, and Q. X. Jia. Photovoltaic response and dielectric properties of epitaxial anatase- TiO_2 films grown on conductive $\text{La}_{0.5}\text{Sr}_{0.5}\text{CoO}_3$ electrodes. *Applied Physics Letters*, 79(17):2797, 2001.
- [68] ASM International. *Engineered Materials Handbook: Ceramics and glasses*, volume 4. ASM International, 1991.
- [69] J. Maier. *Physical chemistry of ionic materials - ions and electrons in solids*. John Wiley & Sons, Ltd, 1st edition, 2005.
- [70] F. A. Kroger and H. J. Vink. Relations between the concentrations of imperfections in crystalline solids. *Solid State Physics-Advances in Research and Applications*, 3:307, 1956.
- [71] H. Peng. First-principles study of native defects in rutile TiO_2 . *Physics Letters A*, 372(9):1527, 2008.
- [72] A. H. Cottrell and B. A. Bilby. A mechanism for the growth of deformation twins in crystals. *Philosophical Magazine*, 42(329):573, 1951.
- [73] J. L. Carpentier, A. Lebrun, and F. Perdu. Point-defects and charge transport in pure and chromium-doped rutile at 1273 k. *Journal Of Physics And Chemistry Of Solids*, 50(2):145, 1989.
- [74] Blumenthal.R. N., J. Coburn, J. Baukus, and W. M. Hirthe. Electrical conductivity of nonstoichiometric rutile single crystals from 1000 degrees to 1500 degrees C. *Journal Of Physics And Chemistry Of Solids*, 27(4):643, 1966.
- [75] D. C. Cronmeyer. Electrical and optical properties of rutile single crystals. *Physical Review*, 87(5):876, 1952.
- [76] D. K. Lee, J. L. Jeon, M. H. Kim, W. Choi, and H. I. Yoo. Oxygen nonstoichiometry (δ) of $\text{TiO}_{2-\delta}$ -revisited. *Journal Of Solid State Chemistry*, 178(1):185, 2005.

REFERENCES

- [77] K. Hoshino, N. L. Peterson, and C. L. Wiley. Diffusion and point-defects in TiO_{2-x} . *Journal Of Physics And Chemistry Of Solids*, 46(12):1397, 1985.
- [78] L. R. Sheppard, A. J. Atanacio, T. Bak, J. Nowotny, M. K. Nowotny, and K. E. Prince. Niobium diffusion in niobium-doped titanium dioxide. *Journal Of Solid State Electrochemistry*, 13(7):1115, 2009.
- [79] T. Bak, J. Nowotny, M. Rekas, and C. C. Sorrell. Defect chemistry and semiconducting properties of titanium dioxide: III. mobility of electronic charge carriers. *Journal Of Physics And Chemistry Of Solids*, 64(7):1069, 2003.
- [80] K. S. Cole and R. H. Cole. Dispersion and absorption in dielectrics: I. alternating current characteristics. *Journal Of Chemical Physics*, 9(4):341, 1941.
- [81] J. Fleig. The grain boundary impedance of random microstructures: Numerical simulations and implications for the analysis of experimental data. *Solid State Ionics*, 150(1-2):181, 2002.
- [82] J. R. Macdonald and W. R. Kenan. *Impedance spectroscopy: Emphasizing solid materials and systems*. John Wiley & Sons, 1st edition edition, 1987.
- [83] N. M. Beekmans and L. Heyne. Correlation between impedance, microstructure and composition of calcia-stabilized zirconia. *Electrochimica Acta*, 21(4):303, 1976.
- [84] J. C. Maxwell. *A treatise on electricity and magnetism*. Clarendon Press, Oxford, 2nd edition edition, 1881.
- [85] T. van Dijk and A. J. Burggraaf. Grain-boundary effects on ionic-conductivity in ceramic $\text{Gd}_x\text{Zr}_{1-x}\text{O}_{2-(x/2)}$ solid-solutions. *Physica Status Solidi a-Applied Research*, 63(1):229, 1981.
- [86] M. J. Verkerk, B. J. Middelhuis, and A. J. Burggraaf. Effect of grain-boundaries on the conductivity of high-purity $\text{ZrO}_2\text{-Y}_2\text{O}_3$ ceramics. *Solid State Ionics*, 6(2):159, 1982.
- [87] J. Maier. On the conductivity of polycrystalline materials. *Berichte Der Bunsen-Gesellschaft-Physical Chemistry Chemical Physics*, 90(1):26, 1986.
- [88] K. K. Adepalli, M Kelsch, R Merkle, and J Maier. Point defect chemistry of SrTiO_3 under the influence of dislocations. *to be submitted*, 2013.

REFERENCES

- [89] X. Guo and J. Maier. Grain boundary blocking effect in zirconia: A Schottky barrier analysis. *Journal of the Electrochemical Society*, 148(3):E121, 2001.
- [90] M. Vollman and R. Waser. Grain-boundary defect chemistry of acceptor-doped titanates - space-charge layer width. *Journal Of The American Ceramic Society*, 77(1):235, 1994.
- [91] I. Denk, J. Claus, and J. Maier. Electrochemical investigations of SrTiO₃ boundaries. *Journal of the Electrochemical Society*, 144(10):3526, 1997.
- [92] J. A. S. Ikeda and Y. M. Chiang. Space-charge segregation at grain-boundaries in titanium-dioxide: I, relationship between lattice defect chemistry and space-charge potential. *Journal Of The American Ceramic Society*, 76(10):2437, 1993.
- [93] J. A. S. Ikeda, Y. M. Chiang, A. J. Garrattreed, and J. B. Vandersande. Space-charge segregation at grain-boundaries in titanium-dioxide: II, model experiments. *Journal Of The American Ceramic Society*, 76(10):2447, 1993.
- [94] K. L. Kliewer and J. S. Koehler. Space charge in ionic crystals: I. general approach with application to NaCl. *Physical Review*, 140(4A):A1226, 1965.
- [95] J. Fleig, F. Noll, and J. Maier. Surface conductivity measurements on AgCl single crystals using microelectrodes. *Berichte Der Bunsen-Gesellschaft-Physical Chemistry Chemical Physics*, 100(5):607, 1996.
- [96] G. Wulff. On the question of speed of growth and dissolution of crystal surfaces. *Zeitschrift Für Krystallographie Und Mineralogie*, 34(5/6):449, 1901.
- [97] H. L. Tuller, S. J. Litzelman, and W. Jung. Micro-ionics: Next generation power sources. *Physical Chemistry Chemical Physics*, 11(17):3023, 2009.
- [98] M. Sasabe, K. Kobayashi, M. Tate, Y. Kuwano, and K. Suzuki. Direct measurement of oxygen partial-pressure in the experimental blast-furnace. *Transactions of the Iron and Steel Institute of Japan*, 22(10):794, 1982.
- [99] M. H. Hebb. Electrical conductivity of silver sulfide. *Journal Of Chemical Physics*, 20(1):185, 1952.
- [100] J. B. Wagner and C. Wagner. Electrical conductivity measurements on cuprous halides. *Journal Of Chemical Physics*, 26(6):1597, 1957.

REFERENCES

- [101] I. Yokota. Theory of mixed conduction with special reference to conduction in silver sulfide group semiconductors. *Journal Of The Physical Society Of Japan*, 16(11):2213, 1961.
- [102] K. H. G. Ashbee and R. E. Smallman. Epitaxial growth of rutile thin films on titanium carbide single crystals. *Philosophical Magazine*, 7(83):1933, 1962.
- [103] K. A. G. Ashbee, R. E. Smallman, and G. K. Williamson. Stacking faults and dislocations in titanium dioxide, with special reference to non-stoichiometry. *Proceedings Of The Royal Society Of London Series A-Mathematical And Physical Sciences*, 276(1364):542, 1963.
- [104] K. H. G. Ashbee and R. E. Smallman. Plastic deformation of titanium dioxide single crystals. *Proceedings Of The Royal Society Of London Series A-Mathematical And Physical Sciences*, 274(1356):195, 1963.
- [105] K. H. G. Ashbee and R. E. Smallman. The fracture of titanium dioxide single crystals with particular reference to non-stoichiometry. *Physica Status Solidi*, 4(2):289, 1964.
- [106] H. Bell, J. T. Jones, and Krishnam.V. Recovery of high-temperature creep-resistant substructure in rutile. *Journal Of The American Ceramic Society*, 55(1):6, 1972.
- [107] J. Weertman. Theory of steady-state creep based on dislocation climb. *Journal Of Applied Physics*, 26(10):1213, 1955.
- [108] M. F. Ashby. First report on deformation-mechanism maps. *Acta Metallurgica*, 20(7):887, 1972.
- [109] S. Pejovnik, D. Susnik, and D. Kolar. Densification of TiO_2 by hot pressing. *Ceramurgia International*, 3(3):92, 1977.
- [110] H. J. Frost and M. F. Ashby. *Deformation-mechanism maps: The plasticity and creep of metals and ceramics*. Pergamon Press, 1st edition edition, 1982.
- [111] J. Ayache, L. Beaunier, J. Boumendil, G. Ehret, and D. Laub. *Sample preparation handbook for transmission electron microscopy-techniques*. Springer, 2010.
- [112] P. Fielitz and G. Borchardt. On the accurate measurement of oxygen self-diffusivities and surface exchange coefficients in oxides via SIMS depth profiling. *Solid State Ionics*, 144(1-2):71, 2001.

REFERENCES

- [113] D. B. Williams and C. B. Carter. *Transmission Electron Microscopy I–IV*. Springer US, 2009.
- [114] O. Byl and Jr. Yates, J. T. Anisotropy in the electrical conductivity of rutile TiO_2 in the (110) plane. *Journal Of Physical Chemistry B*, 110(46):22966, 2006.
- [115] M. K. Nowotny, T. Bak, J. Nowotny, and C. C. Sorrell. Titanium vacancies in nonstoichiometric TiO_2 single crystal. *Physica Status Solidi B-Basic Solid State Physics*, 242(11):R88, 2005.
- [116] B. P. Uberuaga and X. M. Bai. Defects in rutile and anatase polymorphs of TiO_2 : Kinetics and thermodynamics near grain boundaries. *Journal of Physics-Condensed Matter*, 23(43), 2011.
- [117] T. Froemling, H. Hutter, and J. Fleig. Oxide ion transport in donor-doped $\text{Pb}(\text{Zr}_x\text{Ti}_{1-x})\text{O}_3$: Near-surface diffusion properties. *Journal Of The American Ceramic Society*, 95(5):1692, 2012.
- [118] H. S. Carslaw and J. C. Jaeger. *Conduction of heat in solids*. Oxford science publications. Clarendon Press, 1959.
- [119] J. Crank. *The mathematics diffusion*. Oxford. Clarendon Press.
- [120] D. K. Moore, D. J. Cherniak, and E. B. Watson. Oxygen diffusion in rutile from 750 to 1000 degrees C and 0.1 to 1000 MPa. *American Mineralogist*, 83(7-8):700, 1998.
- [121] M. Arita, M. Hosoya, M. Kobayashi, and M. Someno. Depth profile measurement by secondary ion mass-spectrometry for determining the tracer diffusivity of oxygen in rutile. *Journal Of The American Ceramic Society*, 62(9-10):443, 1979.
- [122] F. Seitz. On the generation of vacancies by moving dislocations. *Advances in Physics*, 1(1):43, 1952.
- [123] D. S. McLachlan, M. Blaszkiewicz, and R. E. Newnham. Electrical-resistivity of composites. *Journal of the American Ceramic Society*, 73(8):2187, 1990.
- [124] R. A. De Souza, J. Fleig, J. Maier, O. Kienzle, Z. L. Zhang, W. Sigle, and M. Ruhle. Electrical and structural characterization of a low-angle tilt grain boundary in iron-doped strontium titanate. *Journal of the American Ceramic Society*, 86(6):922, 2003.

REFERENCES

- [125] Krishnam.V, J. T. Jones, and H. Bell. Recovery of creep-resistant substructure of rutile in air and vacuum under reduced stress. *Journal Of The American Ceramic Society*, 56(11):604, 1973.
- [126] R. Orru, R. Licheri, A. M. Locci, A. Cincotti, and G. Cao. Consolidation/synthesis of materials by electric current activated/assisted sintering. *Materials Science & Engineering R-Reports*, 63(4-6):127, 2009.
- [127] D. Hardie and R. N. Parkins. Solid-solution hardening of aluminium and magnesium. *Journal of the Institute of Metals*, 85(10):449, 1957.
- [128] P. A. Flinn. Solute hardening of close-packed solid solutions. *Acta Metallurgica*, 6(10):631, 1958.
- [129] C. D. Wiseman. Substitutional solid-solution strengthening in copper alloys. *Transactions of the American Institute of Mining and Metallurgical Engineers*, 212:847, 1958.
- [130] G. W. Groves and M. E. Fine. Solid solution + precipitation hardening in Mg–Fe–O alloys. *Journal Of Applied Physics*, 35(12):3587, 1964.
- [131] H. Ehrenreich and J. P. Hirth. Mechanism for dislocation density reduction in GaAs crystals by indium addition. *Applied Physics Letters*, 46(7):668, 1985.
- [132] S. McGuigan, R. N. Thomas, D. L. Barrett, H. M. Hobgood, and B. W. Swanson. Effects of indium lattice hardening upon the growth and structural-properties of large-diameter, semi-insulating GaAs crystals. *Applied Physics Letters*, 48(20):1377, 1986.
- [133] J. Cho, C. M. Wang, H. M. Chan, J. M. Rickman, and M. P. Harmer. Improved tensile creep properties of yttrium and lanthanum doped alumina: A solid solution effect. *Journal Of Materials Research*, 16(2):425, 2001.
- [134] H. Yoshida, Y. Ikuhara, and T. Sakuma. High-temperature creep resistance in rare-earth-doped, fine-grained Al_2O_3 . *Journal Of Materials Research*, 13(9):2597, 1998.
- [135] D. A. Rani, Y. Yoshizawa, K. Hirao, and Y. Yamauchi. Effect of rare-earth dopants on mechanical properties of alumina. *Journal Of The American Ceramic Society*, 87(2):289, 2004.

REFERENCES

- [136] J. Mimurada, M. Nakano, K. Sasaki, Y. Ikuhara, and T. Sakuma. Effect of cation doping on the superplastic flow in yttria-stabilized tetragonal zirconia polycrystals. *Journal Of The American Ceramic Society*, 84(8):1817, 2001.
- [137] A. Dominguezrodriguez, K. P. D. Lagerlof, and A. H. Heuer. Plastic-deformation and solid-solution hardening of Y_2O_3 -stabilized ZrO_2 . *Journal Of The American Ceramic Society*, 69(3):281, 1986.
- [138] Z. Feiwu, A. M. Walker, K. Wright, and J. D. Gale. Defects and dislocations in mgo: Atomic scale models of impurity segregation and fast pipe diffusion. *Journal of Materials Chemistry*, 20(46):10445, 2010.
- [139] A.P. Sutton and R.W. Balluffi. *Interfaces in Crystalline Materials*. Clarendon press, Oxford.
- [140] M. Gerstl and J. Fleig. The impedance caused by interfacial current constriction: A case study on BaF_2/YSZ bicrystals. *Monatshefte Für Chemie*, 140(9):1129, 2009.
- [141] M. Shirpour, R. Merkle, C. T. Lin, and J. Maier. Nonlinear electrical grain boundary properties in proton conducting $Y-BaZrO_3$ supporting the space charge depletion model. *Physical Chemistry Chemical Physics*, 14(2):730, 2012.
- [142] S. I. Cha, K. H. Hwang, Y. H. Kim, M. J. Yun, S. H. Seo, Y. J. Shin, J. H. Moon, and D. Y. Lee. Crystal splitting and enhanced photocatalytic behavior of TiO_2 rutile nano-belts induced by dislocations. *Nanoscale*, 5(2):753, 2013.

Acknowledgements

This work would not have been possible without the help of several people, I would like to thank each one of them who contributed to this work both professionally and personally.

I express my deep gratitude to Prof. Joachim Maier for giving me this opportunity to pursue my doctoral studies under his supervision. His suggestions at the right time has enormously improved the quality of this work. I greatly appreciate his support even when things did not worked as we expected at the very beginning of this work. I believe this is a privilege to work with him and also to learn from him the most important concepts in solid state ionics.

I am thankful to Prof. Joachim Bill for accepting to be in my thesis committee. I also would like to thank Professor Frank Gießelmann not only for being the chairman of the examination committee but also for the kind invitation to present my work to his group.

I am very fortunate to have Dr. Rotraut Merkle as my internal supervisor, she is not only a good scientist but also a marvelous teacher. My heartfelt thanks to her for introducing me to the space charge concepts in solid state ionics. I greatly appreciate her time and suggestions on this work. I never heard her saying 'No' for discussions at any stage of this work, her readiness had greatly improved our understanding on this topic.

I would like to thank Sofia Weiglein, secretary of Professor Maier, for helping me with various administrative issues whether it is within the institute or outside, this definitely had saved a lot of time. On a similar note, I also would like to thank Dr. Hans-Georg Libuda, coordinator of International Max Planck Research School (IMPRS), for providing valuable information to get started in Stuttgart. I thank the financial support from the IMPRS fellowship.

A very special thanks to these four people, without their contributions I would not have gotten very far. Firstly, I am grateful to Marion Kelsch for performing TEM on single crystals and polycrystalline samples, and Dr. Fritz Phillipp on bicrystals. I am also grateful to Barbara Baum (crystal preparation group) for spending countless hours in dicing and polishing my samples. Finally, Tolga Acartürk for performing

SIMS analysis on various samples. I really admire their willingness to work on any number of samples without any hesitation.

I greatly appreciate the help from my colleagues at Maier group, I especially thank Dr. Lei Wang, Dr. Mona Shirpour, Dr. Piero Lupetin, Dr. Giuliano Gregori, Dr. Dominik Samuelis and Oliver Gerbig for countless discussions on various scientific topics related to this work. I would like to thank Oliver Gerbig, Anja Wedig, Dr. Ji-Yong Shin, Dr. Mona Shirpour, Dr. Lei Wang, Nils Ohmer, Chia-Chin Chen, Dr. Lijun Fu, Michael Weissmayer, Daniel Pötzsch, Dr. Jelena Popović and Christian Pfaffenhuber for being very nice friends. I thoroughly enjoyed the conversations whether it is scientific or non-scientific.

Many thanks to the hardworking technical staff of Maier group, I would like to thank Udo Klock for the support on electronic equipments, Annette Fuchs for SEM, Ewald Schmitt for machining graphite molds, Peter Senk for furnaces, Gabi Götz for XRD measurements and Uwe Traub for IT support. I also thank technicians from technology service group for thin film depositions, interface analysis service group for SIMS measurements, and crystal preparation group for cutting and polishing innumerable samples.

I would like to thank Prof. Peter van Aken, head of Stuttgart center for Electron Microscopy, for opening various TEM facilities required for this work. I also thank Ute Salzberger of preparing TEM bicrystal specimens, Dr. Behnaz Rahmati for performing EELS characterization, Albert Meyer for ICP-OES analysis and Dr. Jong-Sook Lee, former member of Maier group, for the initial bicrystal set-up.

Many thanks to my Indian friends, Dr. Sairamudu Meka, Dr. Roby Cherian, Dr. Aniket Kulkarni, Dr. Gayatri Rane and Dr. Sridhar Neelamraju. The lunch breaks became more exciting by our useless discussions and arguments on Indian politics.

I spent most of my free time in Stuttgart with the families and friends from Bible Church of Stuttgart. I am greatly indebted to all of them for their love and encouragement that made me feel Stuttgart as my second home. I greatly appreciate the support from the Benzings, Blacks, Blalocks, Harlows, Hoesses, Vignolas families and also the international student fellowship for last three years.

I would like to thank my Dad and Mom for their constant support and love during a seemingly endless time I spent in studies all through these years. I will never forget their hard work which bought me thus far and I always proud to be their son. Thanks to my brother and his family for their love, especially to my nephews for making my weekends very entertaining.

Curriculum Vitae

Name	Kiran Kumar Adepalli
Date of Birth	31.01.1983
Place of birth	Godicherla, India
Since September 2009	Ph.D. Max Planck Institute of Solid State Research Stuttgart, Germany Thesis advisor: Prof. Dr. Joachim Maier Title: <i>Influence of extended defects on the electrical-properties of TiO₂ (Rutile)</i>
June 2008 - July 2009	Project associate in the laboratory of interdiffusion- <i>and electronic packaging</i> Indian Institute of Science, Bangalore, India
July 2006 - May 2008	M.E. in Materials Engineering Indian Institute of Science, Bangalore, India Thesis advisor: Prof. Alope Paul Title: <i>Study on interdiffusion and growth of Nb₃Sn- superconductor with A15 structure</i>
July 2002 - May 2006	B.Tech. in Metallurgical Engineering National Institute of Technology, Warangal, India Thesis advisor: Prof. Karuna S. Ghosh Title: <i>Determination of kinetic parameters of precipitation and dissolution reactions in a 7017 Al -Zn-Mg alloy from differential scanning calorimetric (DSC) studies</i>

